# INFORMATION TO USERS

This manuscript has been reproduced from the microfilm master. UMI films the text directly from the original or copy submitted. Thus, some thesis and dissertation copies are in typewriter face, while others may be from any type of computer printer.

**The quality of this reproduction is dependent upon the quality of the copy submitted.** Broken or indistinct print, colored or poor quality illustrations and photographs, print bleedthrough, substandard margins, and improper alignment can adversely affect reproduction.

In the unlikely event that the author did not send UMI a complete manuscript and there are missing pages, these will be noted. Also, if unauthorized copyright material had to be removed, a note will indicate the deletion.

Oversize materials (e.g., maps, drawings, charts) are reproduced by sectioning the original, beginning at the upper left-hand corner and continuing from left to right in equal sections with small overlaps. Each original is also photographed in one exposure and is included in reduced form at the back of the book.

Photographs included in the original manuscript have been reproduced xerographically in this copy. Higher quality 6" x 9" black and white photographic prints are available for any photographs or illustrations appearing in this copy for an additional charge. Contact UMI directly to order.

**UMI**

A Bell & Howell Information Company
300 North Zeeb Road, Ann Arbor MI 48106-1346 USA
313/761-4700 800/521-0600

# MODELLING LUNG TISSUE RHEOLOGY

Geoffrey Nicholas Maksym

A thesis submitted to the

Faculty of Graduate studies and Research

in partial fulfillment of the requirements for the degree of

Doctor of Philosophy

Department of Biomedical Engineering

McGill University

January 1997

# ABSTRACT

A model was developed to account for the static elastic behaviour of the lung tissue strip in terms of distributions of collagen and elastin fibers. Distributions of collagen fiber lengths and elastin fiber stiffnesses were determined by fitting the model to data from dog lung tissue strips. These distributions followed $1/f$ power-laws for more than 95% of the data. Computer simulations of two dimensional tissue strip models with $1/f$ distributions of collagen fiber lengths also predicted realistic stress-strain curves. The simulations illustrated the gradual development of geometric and stress heterogeneity throughout the tissue as the collagen fibers were recruited during stretch. This model suggests a mechanistic basis for the shape of the pressure-volume curve of whole lung. It also indicates how this curve may be affected by changes in tissue collagen and elastin similar to the changes occurring in the diseases of pulmonary emphysema and fibrosis. Nonparametric block-structured nonlinear models for describing both the static and dynamic stress-strain behaviour of the lung were applied to dog lung tissue strips and to whole rat lungs *in vivo*. Both the Wiener and Hammerstein models accounted for more than 99% of the tissue strip data, although the Hammerstein model was more consistently accurate across a range of perturbation amplitudes and operating stresses. Plastic dissipation of energy within the lung tissue strip was estimated at less than 20% of the total dissipation during slow sinusoidal cycling. The Hammerstein model was also the best of those investigated for describing the rat lung data *in vivo*, although there were dependencies of the model parameters on perturbation amplitude and operating point that indicate that a more complicated model is required for the whole lung. Finally, construction of a fiber recruitment model for the dynamic mechanical behaviour of lung tissue strips was attempted. However accurate reproduction of measured behaviour was not achieved, indicating that lung tissue dynamics arise from processes independent of fiber recruitment and may originate from the ensemble behaviour of its many constituents interacting as a complex dynamic system.

# ABRÉGÉ

Un modèle a été développé pour expliquer le comportement statique-élastique d'une bande de tissu pulmonaire en fonction de la distribution des fibres collagènes et élastines. Les distributions de longueurs de fibres collagènes et de rigidités de fibres élastines ont été déterminées en comparant le modèle aux données provenant des bandes de tissu pulmonaire canin. Ces distributions se conforment à une distribution 1/f pour plus de 95% des données. Des simulations de modèles bi-dimentionnels faites à partir de distributions 1/f de longueurs de fibres collagènes prédisent des diagrammes allongement-contrainte vraissemblables. Ces simulations démontrent le développement de l'hétérogénéité de la géométrie et de la contrainte au cours du recrutement des fibres collagènes en fonction de la traction. Ceci suggère un mécanisme qui détermine la forme du diagramme pression-volume du poumon. De plus, ce mécanisme explique comment les changements de ce diagramme peuvent provenir de changements de tissus collagènes et élastines tels qu'occasionnés par l'emphysème et la fibrose pulmonaire. Les modèles non-paramétriques à base de modules ont été appliqués à des bandes de tissu pulmonaire canin et à des poumon de rat in vivo pour décrire le comportement statique et dynamique du diagramme allongement-contrainte. Les modèles de Wiener et de Hammerstein expliquent, chacun, plus de 99% des données de bandes de tissu. Cependant, celui de Hammerstein indique une précision plus uniforme pour différentes amplitudes et contraintes d'opération. L'émission énergétique due à la déformation plastique de la bande de tissu représente moins de 20% de l'émission totale effectuée durant des mouvements sinusoïdaux cycliques lents. Le modèle de Hammerstein est aussi le plus approprié pour décrire le poumon du rat in vivo. Cependant, les paramètres du modèle dépendent de l'amplitude et de la contrainte moyenne; donc un modèle plus sophistiqué du poumon entier est nécessaire. Finalement, un modèle du comportement dynamique d'une bande de tissu pulmonaire basé sur le recrutement de fibres a été essayé, mais ne permet pas la prédiction des propriétés mesurées. Ceci indique que les propriétés dynamiques proviennent de processus indépendants du recrutement de fibres, et peut être d'un comportement de l'interaction du système dynamique de l'ensemble de ses éléments.

*To Jen*

# PREFACE

This thesis is divided into 9 chapters. Chapter 1, is an introduction to the thesis, while Chapter 2 gives a review of the literature relevant to this thesis. Chapters 3 and 5 contain content that is in press at the *Journal of Applied Physiology*[1]. Chapter 4 is to be submitted to *Computer Methods in Biomechanics and Biomedical Engineering*. A portion of the work shown in the Introduction to Chapter 6 has been published in the *Journal of Applied Physiology*[3]. Chapter 7 has been submitted to the *Annals of Biomedical Engineering*[2]. A portion of the work of Chapter 8 has been published in the *Annals of Biomedical Engineering*[4]. Chapter 9 provides conclusions to the thesis, statements of original contributions, and suggestions for future research. Conference papers and abstracts that have resulted from the work contained in this thesis are listed below.

### *Journal Articles*


[1]**Maksym, G. N.** and J. H. T. Bates. A distributed nonlinear model of lung tissue elasticity. *J. Appl. Physiol.* (in press).

[2]**Maksym, G. N.** and J. H. T. Bates. Nonparametric block structured modeling of rat lung mechanics. *Ann. Biomed. Eng.* (submitted).

[3]Navajas, D., **G. N. Maksym**, and J. H. T. Bates. Dynamic viscoelastic nonlinearity of lung parenchymal tissue. *J. Appl. Physiol.* 79: 348-356, 1995.

[4]Bates, J. H. T., **G. N. Maksym**, D. Navajas, and B. Suki. Lung tissue rheology and 1/f noise. *Ann. Biomed. Eng.* 22: 674-681, 1994.

*Conference papers (2-page minimum)*

**Maksym, G. N.** and J. H. T. Bates. Distributed modeling of nonlinear tissue elasticity. *Proc. 20th Conf. Canadian Med. Biol. Eng. Soc. Vancouver.* 138-139, 1994.

**Maksym, G. N.** and J. H. T. Bates. A theory for the basis of lung tissue elasticity. *Proc. 17th Ann. Int. Conf. IEEE Eng. Med. Biol. Soc. Montreal.* 1527-1528, 1995.

*Abstracts*

Bates, J. H. T. and **G. N. Maksym.** A nonlinear distributed model of lung tissue elasticity. *Ann. Biomed. Eng.* 23: s-11, 1995.

**Maksym, G. N.** and J. H. T. Bates. An analytical model for lung distensibility. *American Journal of Respiratory & Critical Care Medicine* 151: A116, 1995.

**Maksym, G. N.** and J. H. T. Bates. A nonlinear model of lung parenchyma disease. *Ann. Biomed. Eng.* 1996.

**Maksym, G. N.**, T. F. Schuessler, and J. H. T. Bates. Nonlinear pulmonary rat mechanics identification. *American Journal of Respiratory & Critical Care Medicine* 151: A116, 1995.

The apparatus for the tissue strip experiments is described in my Master's Thesis, *Computer controlled oscillator for dynamic testing of biological soft tissue strips*, M.Eng. McGill University, 1993. The stress-strain curves of Chapter 3 were obtained in collaboration with Dr. Daniel Navajas. Ms. Carrie Dolman performed most of the animal preparation for Chapter 7. Mr. Thomas Schuessler constructed the small animal ventilator used in Chapter 7.

# ACKNOWLEDGMENTS

I would like to acknowledge the Natural Sciences and Engineering Research Council of Canada and Fonds pour la Formation de Chercheurs a l'Aide à la Recherche de Québec who supported me for nearly my entire course of study.

I am greatly indebted to my thesis supervisor, Dr. Jason Bates, who gave me support, and who always found just the right balance of guidance and freedom, tempered with more than a little good humour. I am also grateful to Thomas Schuessler and William Thorpe who were there as friends and colleagues in and outside the lab (especially far outside). I greatly appreciated their helpful comments and assistance along with that from my colleagues in the lab, Gail Dechman, Anne-Marie, Bengt Kayser, Andrew Adler, Tadashi Nemoto, Rute Gomez, Mohsen Ahmadi, and finally Norihiro Shinozuka, who always could listen and make us all smile. Some of this work was greatly aided by technical assistance from Whitney deVries, Serge Filiatrault and especially Carrie Dolman from whom I learned surgical preparation, and Dr. Daniel Navajas whose expertise I will constantly aspire to. Also not to be under-emphasized are the high times I shared with the members of the Students and Post-docs in Respiration (inSPIRe) of the Meakins-Christie labs; thanks go to my co-director of social activities, for being Flo. Thanks also to Gail and Cheryl for the fun times.

My parents bear a great responsibility for having set me forth with such wide eyes. They and my brother Ted made my childhood as happy as I can imagine. And finally, my very dear thanks go to my wife, Jennifer, whose encouragement, patience and love were an integral part of this work.

# TABLE OF CONTENTS

# LIST OF FIGURES

# LIST OF TABLES

# LIST OF SYMBOLS

| Symbol | Definition | page |
|---|---|---|
| $P$ | pressure | 1 |
| $V$ | volume | 1 |
| $A,B,K$ | parameters of the Salazar and Knowles equation | 10 |
| TLC | total lung capacity | 10 |
| COPD | chronic obstructive pulmonary disease | 10 |
| $L_m$ | mean linear alveolar intercept | 11 |
| $E$ | elastance | 18 |
| $R$ | resistance | 18 |
| $K_p$ | baseline pressure | 18 |
| $\dot{V}$ | flow | 18 |
| $A_h,B_h$ | parameters of the Hildebrandt equation | 20 |
| $\Delta V$ | step change in volume | 20 |
| $\eta$ | hysteresivity | 20 |
| $Z$ | mechanical impedance | 21 |
| $G_t,H_t,\alpha_t$ | parameters of the constant phase model | 21 |
| $c,d$ | parameters of the stress-relaxation function | 21 |
| $K_1,K_2$ | constants to Rohrer model | 22 |
| $x(t)$ | system inputs | 25 |
| $y(t)$ | system outputs | 25 |

| Symbol | Definition | page |
|---|---|---|
| $h_0,h_1...,h_\infty$ | Volterra series kernels | 25 |
| $\phi_{xy}$ | first-order cross-correlation function between $x$ and $y$ | 26 |
| $m_w$ | Wiener model nonlinearity | 27 |
| $h_w$ | Wiener model impulse response function | 27 |
| $u_w$ | Wiener model intermediate signal | 27 |
| $\hat{y}(t)$ | estimated output | 27 |
| VAF% | variance accounted for in percent | 27 |
| $m_h$ | Hammerstein model nonlinearity | 28 |
| $h_h$ | Hammerstein model impulse response function | 28 |
| $u_h$ | Hammerstein model intermediate signal | 28 |
| $\sigma$, $\sigma_r$ | stress, reference stress | 28 |
| $\lambda$, $\lambda_r$ | length ratio with respect to resting length, reference length ratio | 28 |
| $\sigma_o$ | stress prior to step change in strain of tissue strip | 28 |
| $\alpha_n,\gamma_n$ | parameters of Navajas model | 28 |
| $k$ | stiffness of a spring | 31 |
| $l$ | stop-length of a string | 31 |
| $L$ | length | 31 |
| $F$ | force | 31 |
| $L_r$ | resting length of models or tissue strips | 32 |
| $L_s$ | length of stopped units | 32 |
| $L_u$ | length of unstopped units | 32 |
| $N(l)$ | stop-length density distribution function | 32 |

| Symbol | Definition | page |
|---|---|---|
| $l_o$ | stop-length of just stopped unit at $F$ | 32 |
| $X$ | area under stop-length distribution | 33 |
| $M(k)$ | stiffness density distribution | 33 |
| $k_o$ | stiffness of just stopped units at $F$ | 34 |
| $Y$ | area under stiffness distribution | 34 |
| $A_r$ | tissue cross-sectional area | 35 |
| $\rho$ | tissue density | 35 |
| $G,H$ | parameters of tissue stress-strain curves | 36 |
| RMS | root mean squared | 38 |
| $\varepsilon_f$ | maximum strain of a model | 40 |
| $l_f$ | maximum stop length of a model | 41 |
| $F_f$ | maximum force of a model | 41 |
| $k_f$ | maximum stiffness of a model | 42 |
| $b$ | exponent in power-law function | 47 |
| $l_g$ | length to which spring-string unit is extended | 51 |
| $l_k$ | knee length of spring-string unit | 51 |
| $k_1, k_2$ | stiffnesses below and above $l_k$, respectively | 51 |
| $Q, \Delta Q$ | node position, change in node position | 53 |
| $\mu$ | adaptive parameter | 53 |
| $F_{max}$ | maximum force in a spring-string unit | 56 |
| $\nu$ | stop volume of a spring-string unit | 66 |
| $N(v)$ | stop volume density distribution | 67 |

| Symbol | Definition | page |
|---|---|---|
| $\varphi$ | stop volume distribution shape factor | 67 |
| $M(E)$ | elastance density distribution | 67 |
| $\gamma$ | shape factor for elastance distribution | 67 |
| PDF | probability density distribution | 82 |
| $H(f)$ | Fourier transform of linear impulse response function | 82 |
| $\dot{\varepsilon}(f)$ | time derivative of strain in Fourier domain | 83 |
| RMSE | root mean squared error | 85 |
| IRF | impulse response function | 98 |
| $a_0, a_i$ | polynomial coefficients | 99 |
| $\delta$ | Dirac delta function | 99 |
| $h_p$ | impulse response function of parallel model | 100 |
| $m_p$ | nonlinearity of parallel model | 100 |
| PEEP | positive end-expiratory pressure | 107 |
| SAV | small animal ventilator | 107 |
| $p_{cyl}, P_{cyl}$ | pressure within cylinder, time and frequency domain | 109 |
| $v_{cyl}, V_{cyl}$ | volume within cylinder, time and frequency domain | 109 |
| $Z_{tb}$ | impedance of tracheal tube | 109 |
| $Z_{sh}$ | shunt impedance of SAV | 109 |
| $Z_o$ | impedance during open calibration of the SAV | 109 |
| $R_L$ | lung resistance | 111 |
| $E_L$ | lung elastance | 111 |
| $Z_L$ | lung impedance | 111 |

| Symbol | Definition | page |
|---|---|---|
| $\beta$ | exponent of power law stress-relaxation | 126 |
| $C$ | coefficient of power law stress-relaxation | 126 |
| $\alpha$ | exponent in power law impedance dependence on $f$ | 128 |
| $r$ | resistance of dashpot | 130 |
| $D_{eq}$ | equivalent resistance of collection of dashpots | 131 |
| $K_{eq}$ | equivalent stiffness of model | 131 |
| $\tau_{eq}$ | equivalent time constant of collection of springs and dashpots | 131 |
| $F_o$ | instantaneous response of spring-string-dashpot models | 131 |
| A1,A2,B1,B2 | models consisting of springs, strings and dashpots | 131 |
| $\tau_{A1}, \tau_{A2}$ | time constant of model A1, A2 | 131 |
| $\tau_{B1}$ | time constant of model B1 | 134 |
| $\tau_{B2}$ | time constant of model B2 | 135 |

# 1. Introduction

The mechanical impedance to breathing arises from the mechanical properties of the chest wall and the lung. A large portion of the lung impedance comes from the rheological properties of the lung tissue, where the tissue rheology embodies all of its mechanical behaviour. Historically, lung mechanics have almost always been modelled by separating the 'static' properties from the 'dynamic'. This is primarily due to the two most common methods of measuring the lung behaviour. With a slow inflation or deflation one obtains the 'static' pressure-volume (*PV*) curve (21,45), while with the forced oscillation technique (30,52) the dynamic mechanical impedance can be obtained. Furthermore, modelling the static *PV* curve has been largely empirical while the impedance is commonly modelled using linear parametric approaches (12,30,65,89). Many researchers have recognised the importance of understanding the origins of tissue rheology and have put forward a variety of models to describe the observed behaviour. These models have been largely parametric and focused on explaining the dynamic behaviour (37,58,107,114,144,145,152,155,160). Recently, some of these have included static nonlinearities using block structured models of the Hammerstein form to study the mechanics of lung tissue strips (114), or of either the Wiener and Hammerstein forms in the study of the mechanics of whole lungs *in vivo* (160). These last two models have shown promise in describing the observed mechanical behaviour. However, both were parametric in form, and neither modelled the observed data perfectly. Thus I felt it was important to apply these block structured models in nonparametric form, to determine the appropriateness of these model structures without bias. Furthermore, I wished to examine the nature of the nonlinearity obtained from these modelling approaches in order to assess whether either model could extract the static nonlinear behaviour from dynamic measurements, and whether the extracted nonlinearity would correspond to the well known static nonlinearity in lung mechanics.

My interest in the static nonlinear behaviour extended beyond the empirical description of the nonlinear curve. In particular, I wished to improve our understanding of how collagen and elastin fibres interact to produce the stress-strain curve. Setnikar (137) first introduced the now well-recognised qualitative idea that elastin determines the stress-strain behaviour of lung parenchyma at low strains while collagen takes over as strain increases. More recently there have been a few studies that explore this idea in a quantitative fashion. For example, Fung (41) developed a recruitment model based on observed distributions of fibre types to develop a strain energy function for the calculation of linear incremental material constants. A model based on reorientation of fibres was introduced by Suwa et al. (161), while models based on the gradual recruitment of kinked or 'wavy' fibres were proposed by Soong and Huang for human alveolar wall (143) and by Decraemer et al. (27) for various biological soft tissues. However, these models consisted of only one fibre type, elastic collagen, and assumed a specific functional form for the distribution of fibre lengths rather than estimating the distribution from the available data. I have thus developed a quantitative model which provides a mechanistic basis for the shape of the stress-strain curve based on the fundamental properties of the stress-bearing constituents, the collagen and elastin fibres. I have explored this model further in a 1D computer simulation to investigate the effects of variability among the constituents. I have also developed a 2D model in order to introduce greater physiologic reality. Finally, I have extended the model conceptually in an attempt to understand how changes in tissue constituents due to diseases such as emphysema and fibrosis can explain the abnormal shapes of $PV$ curves seen in patients with these diseases.

The key aim of this work was therefore to improve our understanding of lung tissue rheology under normal conditions and in disease. There are two main thrusts of the thesis. In the first, I derive models which give a mechanistic explanation of the nonlinear stress-strain behaviour of lung tissue in terms of the fundamental properties of the stress-bearing constituents. In the second, I apply Wiener and Hammerstein models to the mechanics of rat lungs *in vivo* and lung tissue strips *in vitro*.

## 1.1 Overview

Chapter 2 presents a brief introduction to modelling lung mechanics. A review of the literature is provided which examines the lung structure and mechanics relevant to this thesis. This is followed by a detailed discussion on the different modelling approaches that have been applied to the lung mechanics, with particular attention paid to nonlinear approaches.

Chapter 3 presents a one-dimensional model of the lung tissue static elastic behaviour. Important structure to function relationships for the lung tissue are described. The model is based on distributing the fundamental properties of the stress-bearing constituents of the lung tissue, the collagen and elastin fibres. Measurement of stress-strain curves of lung tissue are reported. These data are used to derive the distributions of the model.

Chapter 4 extends the models of Chapter 3 by introducing geometric effects via a two-dimensional finite element simulation. Different distributions of constituent element properties are generated and length-tension curves produced from the model are compared with measured tissue strip data.

In Chapter 5, the ideas developed in the first chapter are applied to the $PV$ curves of the whole lung *in vivo*. Important relationships are made between the structural changes in the lung tissue and the changes observed in the shapes of $PV$ curves in the lung diseases of emphysema and fibrosis.

Chapters 6 and 7 introduce non-parametric modelling to the field of respiratory mechanics. In Chapter 6, Wiener and Hammerstein models are applied to lung tissue strips perturbed with pseudo-random strain input signals. A new parallel arrangement of the functional blocks of these models is developed and fit to the same data. In Chapter 7, large amplitude pseudo-random volume input signals are used to identify Wiener and Hammerstein models of rat lung mechanics *in vivo*.

In Chapter 8, an exploratory look is taken into extending the modelling concepts introduced in Chapter 3 to account for the dynamic behaviour of lung tissue.

Finally, Chapter 9 summarises the contributions made in this thesis, and provides suggestions for further research.

# 2. Literature review

## 2.1 Physiology of the lung

The lung is one part of the total respiratory system, which includes the upper airways, the chest wall and the respiratory musculature. The primary function of the respiratory system is to provide adequate gas exchange – the supply of oxygen to the blood and removal of carbon dioxide – according to the body's metabolic requirements. The lung inflates due to the negative pressure (with respect to atmosphere) applied at its surface by the respiratory muscles. Deflation normally occurs passively as a result of the static recoil of the lung and chest wall, but effort by the internal intercostals and abdominal muscles can supply an active contribution during exercise. Most of the mechanical energy expended during inflation is elastic and is thus recovered during deflation. The remaining energy is dissipated through viscous effects in both the airways and the tissues. These processes comprise the mechanics of the respiratory system.

### 2.1.1 Lung structure

Surrounding the lung is the visceral pleura which smoothly slides against the parietal pleura lining the ribcage, diaphragm and mediastinum. Upon inspiration, air is conducted from the mouth and nose through the airways to the sites of gas exchange, the alveoli. The airways form an asymmetric tree-like structure branching through a series of bifurcations to successively smaller bronchi, lobar, segmental and subsegmental bronchi, small bronchi, bronchioles, respiratory bronchioles, and finally to the alveolar ducts and alveoli. The mean number of generations of branching airways from the trachea to alveoli is 23, but a given path can have many more or less branches. Some alveoli are located along the respiratory bronchioles, but most alveoli line the alveolar ducts. The walls of the airways larger than generations 12-16 (counting from the trachea) contain cartilage

which contributes to maintaining airway calibre. In the smaller airways, calibre is maintained through connection with the surrounding parenchyma. The alveoli are the sites of gas exchange and comprise a total surface area of from 43 to 102 $m^2$ depending on body size (170).

Gas is exchanged by passive diffusion through the alveolar walls to an extensive network of pulmonary capillaries that form part of the pulmonary circulation. Separating the blood within the capillaries from the air in the lung are the endothelial layer of the capillaries, the pulmonary interstitium filled with the interstitial fluid, and the alveolar epithelium. The alveoli and septa comprise the large part of the lung parenchyma which tethers both airways and vasculature. The septa are thicker bands of fibrous tissue which branch through the parenchyma subdividing different lung structures from the acini (the collection of alveoli fed by a single terminal bronchiole) to the largest segments dividing the lung lobes. Within the alveolar walls, free edges and septa run a complex interconnected network of collagen and elastin fibres. The fibres are embedded in the ground substance which is an amorphous material primarily composed of proteoglycans, serum constituents, cell products, enzymes, other glycoproteins and products from the degradation of collagen and elastin (50).

### 2.1.2 Stress bearing constituents of lung tissue

It is commonly agreed that the stress-bearing constituents of lung tissue are the collagen and elastin fibres. These fibres differ considerably in their elastic properties. The incremental Young's modulus of collagen at typical strains is $6.8 \times 10^8$ dyn/$cm^2$ to $1.2 \times 10^{11}$ (40,56), while the Young's modulus of elastin is $1 \times 10^6$ to $8 \times 10^6$ dyn/$cm^2$ (41). In other words, collagen is 100 to 10 000 times stiffer than elastin. Elastin is extensible by as much as 230% of its unstressed length (17), while collagen once taut is only extensible by 1-3 % (56). Other components of the lung tissue which may contribute to its mechanics are the ground substance, smooth muscles and other cells. Brown et al. (14) proposed that the deformation of the ground substance may be a significant influence on the mechanical properties of tissue, although this remains to be tested. However, all these

components have much lower elastic constants than both collagen and elastin (41), and are thus likely to play only minor roles in maintaining tissue tension. The ground substance has been proposed to be responsible for much of the viscous dissipation within the lung tissue (70).

Both collagen and elastin occur only within the interstitium, external to the interstitial cells (117). The distributions of collagen and elastin fibre diameter distributions were measured in human pulmonary alveolar walls by Sobin et al. (142) and in alveolar mouths and ducts by Matsuda et al. (97). They found that collagen and elastin fibre diameter distributions were skewed towards a larger density of smaller diameters. Fibre curvatures were similarly distributed, but with a greater skewness. They found that the square root of fibre width and the cube root of fibre curvature were both distributed in an approximately Gaussian fashion. The mean thicknesses of elastin and collagen fibre bundles were about five times greater in the alveolar mouths and ducts than in alveolar walls (97).

The differences in quantities of elastin and collagen in different structures within canine lung parenchyma were examined by Oldmixon and Hoppin (117). They found that elastin was primarily located along free edges of septa and along septal intersections. Also, the elastin in septa was much larger in diameter (~10x) than that in the alveolar walls. Similar to elastin, collagen was found in large bundles in the septal borders and edges, but was more diffusely scattered in the alveolar walls. The ratio of collagen to elastin was near unity in the edges and borders, but near 2:1 in the walls. Mercer et al. (103) found similar results in humans, but found the collagen to elastin ratio was higher in the alveolar walls in rats (~5:1). Using serial sections, they also observed that collagen fibres near the septal edges meandered about in a wavelike fashion with no apparent order or uniform pattern. The elastin and collagen fibres were interwoven, especially in the alveolar entrance ring region, implying some mechanical coupling. The studies of Oldmixon and Hoppin (117), Sobin et al. (142) and Matsuda et al. (97) each found a wide distribution of fibre widths and a complex connected network of both collagen and elastin fibres.

### 2.1.3 Measurements of lung tissue mechanics

Knowledge of the contribution of the lung tissues to the mechanics of breathing can be obtained in 3 ways: via direct measurements *in vitro*, by partitioning tissue and airway behaviour *in vivo* using the alveolar capsule technique, or via modelling approaches. Direct measurements of the tissue are done on excised samples of lung parenchyma, usually maintained in a tissue bath, by uniaxial, biaxial or triaxial stretching. The alveolar capsule technique was originally proposed by J. Mead but developed by Sasaki et al. (133) and improved by Fredberg (36). By measurement of alveolar pressure together with pressure and flow at the airway opening, this technique permits the separate determination of airway and tissue impedances. Modelling approaches will be covered in Section 2.2. Each method has advantages and limitations, and can be viewed as complementary to the others.

***Measurements of lung tissue mechanics in vitro***

The first measurements of lung tissue *in vitro* were made by Radford in 1957 (129), who found that tissue strips from dog lungs exhibited very nonlinear elastic properties. Suwa et al. (161) measured the length-tension relationships for a single extension of human lung parenchymal strips, and found the force to be an exponential function of the strain. The length-tension relationship of human alveolar wall segments was found to be similar by Fukaya et al. (38), who showed that the length-tension curves exhibited tissue hysteresis. They also found that lung tissue exhibited stress-relaxation after a step change in force. Sugihara et al. (149,150) measured human alveolar wall segments and showed very similar results, and found that neither age, sex nor diseases such as emphysema altered the amounts of hysteresis or stress-relaxation.

Measurements of larger samples (1 cm cubes) of parenchyma subjected to triaxial loading were obtained by Hoppin et al. (59), who searched for tissue anisotropy by looking for differences in the stress-strain curves and hysteresis along different axes. They concluded that either the degree of anisotropy was small and not systematically distributed throughout the lung, or that the observed anisotropy was due to differences in the experimental handling of each sample. Tai and Lee (162) also examined isotropy and

homogeneity in triaxial tests of dog parenchyma. They found less than 10% anisotropy in young dogs and less in older dogs. Also, no regional variation was discovered in lung samples taken from different parts of the lung. They therefore concluded that lung parenchyma can be reasonably assumed to be isotropic and homogeneous with respect to its bulk mechanical behaviour. Other mechanical tests on lung tissue have been performed to assess the effects of transverse loading (165,180) and changes in temperature (25,69).

### 2.1.4 Quasi-static *PV* behaviour of the normal and diseased lung

Some of the recoil pressure of the inflated lung is due to deformation of the tissues, while the remainder is due to development of surface tension at the air-liquid interface. The classic approach to determining the respective contributions of the tissues and surface tension to the *PV* curve is by comparing the behaviour of air-filled and saline-filled lungs, in which the effects of surface tension are presumably abolished (46,140,148). The saline-filled *PV* curve moves to lower pressures for the same volume, and the size of the hysteresis loop is decreased compared to the air-filled *PV* curve. In the saline-filled case, hysteresis is due solely to energy dissipation within the tissues, and is similar to that found in *in vitro* studies of lung tissue strips (38,149). In the air-filled case the additional hysteresis is due to the surface lining layer and to recruitment and derecruitment of airways through the collapse and reopening of airways, particularly at low lung volumes (19,26,100,113). In addition, differences between saline-filled and air-filled lungs are always much greater for the inflation limbs than the deflation limbs of *PV* curves, implying that surface tension plays a more important role during inflation. This may be due to the high pressures needed to open collapsed airspaces upon inflation (in the air-filled case) and hysteresis of the surface lining layer. There are problems with the assumption that saline-filling reproduces the same tissue forces that are generated upon air-filling at the same lung volume. The surface tension forces and tissue forces are not entirely independent. That is, surface tension provides a contribution to recoil, directly and indirectly, by distorting the parenchymal geometry (60,144). Evidence for such

distortions was provided by Gil et al. (46) in fixed lungs at different volumes, who showed that the total alveolar surface area was larger in saline-filled lungs than in air-filled lungs at the same volume. Thus, estimates of the surface tension contribution to recoil obtained by saline inflation are in general too large. Considering this, Bachofen et al. (3) found that alveolar geometry is dependent on both surface and tissue forces at low lung volumes, while tissue forces are the predominant determining factor at high lung volumes. An analysis by Oldmixon and Hoppin (117) also concluded that tissue tensions exceed those of surface tension at all lung volumes, and indeed even dominate at low lung volumes. Although estimates for the amount of recoil due to surface tension vary, it would appear that both the tissue and surface tension components are significant at all lung volumes (46,146,148).

The equation most commonly used for the static pressure volume curve is that first introduced by Salazar and Knowles (132),

$$V = A - B\exp(-KP), \tag{2-1}$$

where $A$, $B$ and $K$ are constants. This curve has been found to accurately describe the shape of the PV curve above 50% of total lung capacity (TLC), but parameters are significantly altered if the curve is fit below this volume (21).

The parameter $K$ (Eq. 2-1) has been found to be increased in patients with emphysema (45,48,120) and to be decreased in fibrosing alveolitis (163). Emphysema is characterised as a loss of tissue resulting in an enlargement of alveolar airspaces, an increase in TLC and a decrease in elastic recoil (44). There are two forms of emphysema – panlobular emphysema, in which the disease is present in an essentially homogeneous manner throughout the lung, and centrilobular emphysema, which has a more heterogeneous development usually concentrated near larger airways. Emphysema is one of the conditions classified as a chronic obstructive pulmonary disease (COPD). COPD is characterised by very long passive expiratory time constants due to chronic or recurrent increases in resistance (obstruction) to airflow. Emphysema is most commonly linked with a history of smoking, although persons with alpha$_1$ antiprotease deficiency (a genetic condition) have a 70 to 80% risk of developing the disease as well (141). In emphysema

the increased resistance is irreversible and is mostly concentrated in the peripheral airways (127). By contrast, fibrosis is an example of a restrictive disease. These are diseases in which vital capacity is reduced. Fibrosis is associated with widespread inflammation, an increase in the concentration of interstitial fibre constituents, and airspaces which are reduced or even filled in with inflammatory products (33). Both emphysema and fibrosis characteristically occur inhomogeneously; some areas of the lung can be greatly affected, while other regions appear normal (44).

The parameter $K$ in Eq. 2-1 has also been shown to be independent of lung size and sex (22,45) and to be related to age. Morphologically, $K$ has been shown to be directly related to the mean linear alveolar intercept, $L_m$, between alveolar walls of peripheral airspaces (48,49). Haber et al. (49) found that $L_m$ measured in lungs from dogs, cats and rats, was linearly related to $K$ obtained from air-filled lungs, but that there was no relation between $L_m$ and $K$ obtained from saline-filled lungs. This implies that alterations in $K$ due to disease are linked to changes in surface tension - insofar as saline-filling assesses the tissue contribution to elastic recoil. $K$ was also found to be linearly related to $L_m$ in emphysematous human lungs obtained post-mortem (48). However, as pointed out above, due to the mechanical coupling between surface tension and tissue stress under air-filling conditions, a portion of the component of elastic recoil due to surface tension may originate from changes in tissue distensibility. It has also been shown that in patients with emphysema, specific lung elastance calculated as a function of inflation pressure is consistently greater than that of normals (91). A tissue based change in mechanics was found by Sugihara et al. (150) who reported that alveolar walls taken from lungs with emphysema showed a decrease in maximum extension compared to those taken from normal lungs. They assumed this to be due to a increase in the resting length of alveolar walls in the emphysematous lungs.

The amounts of collagen and elastin and their spatial arrangements in the lung are altered in both emphysema and fibrosis. Pathologic studies in humans have confirmed the elastic fibre network as the site of major lesion in human emphysema and the disease is often associated with the degradation of elastin components by proteolytic enzymes

released from inflammatory cells (141). In smoke-induced emphysema in guinea pigs, elastin volume concentration has been shown to be increased, while collagen volume concentrations were initially reduced and then increased due to resynthesis (178). Elastase-induced lung injury is often used as a model of emphysema, as it reproduces the characteristic increases in $L_m$ and decreases in total alveolar surface area (128,179). Elastase-induced lung injury has also been shown to cause long term changes in elastin and collagen concentrations in hamsters (68). Mercer et al. (104) have shown that elastase injury in hamsters introduces gaps in the normally continuous band of elastin that encircles alveolar entrance rings. In human lungs with fibrosis, airspaces are replaced with fibrotic tissue, and the remaining alveoli show an increased wall thickness (167). Similar results have been observed in bleomycin-induced and radiation-induced fibrosis in baboons, where elastin concentrations were increased above normal (33).

As well as fibre concentration after exposure to digestive enzymes, the mechanical properties of lungs or lung tissue exposed to either elastase or collagenase have been measured. Koo et al. (75) measured the mechanical properties of *in vivo* hamster lungs exposed to pancreatic elastase or collagenase. After 21 days of treatment with elastase the lungs showed a marked increase in TLC and a shift in the $PV$ curve to the right, indicative of reduced elastic recoil. However, with collagenase, only slight increases in TLC were observed. However, the same group found that, soon after instillation of collagenase in hamster lungs *in vitro,* TLC increased markedly, while elastase had little effect on TLC (70). The difference in response was therefore attributed to remodelling before the *in vivo* measurements. Sata et al. (134) measured the length-tension characteristics of elastase and collagenase strips over a wide range of strain. They modelled the elastic behaviour using a bi-exponential function, the first exponential accounting for the low strain and the second accounting for the high strain portions of the stress-strain curve. They showed that the exponent of the first exponential was altered only by the elastase treatment while the exponent of the second exponential was altered only by the collagenase treatment.

## 2.2 Modelling lung mechanics

### 2.2.1 Overview

Two approaches in general have been applied to modelling lung behaviour: models which attempt to reproduce static elastic behaviour, and models to describe the dynamic mechanical impedance. Very few models attempt to incorporate both aspects simultaneously. The principal goal of modelling lung mechanics is to gain insight into underlying causes for observed behaviour. There are two main paradigms of modelling which can fulfil this task: forward modelling and inverse modelling. Forward modelling is essentially the construction of a model whose constituent elements are given defined properties, and the model behaviour is compared with observations of the system under study. Inverse modelling consists of first devising a model structure, and then the parameters of the model are chosen so that the model matches observed behaviour as closely as possible. Both modelling approaches usually make use of *a priori* information of the physiologic system in order to construct an appropriate structure. However, another approach to modelling which makes very few assumptions about model structure is the so-called 'black box' approach. The black box model embodies the relationship between input and output empirically, but in general incorporates limited structural or functional information about the system.

The structure of any model depends on the data it is meant to mimic. Since there are many possible methods of measuring the mechanics of the lung, there are many different models. The following sections will give a brief summary of different modelling approaches applied to the study of the respiratory system, with particular attention paid to the lung and especially to models of the lung tissue. Models of the static mechanics have principally been of the forward type, while models of lung dynamics have been mostly inverse. As will be discussed, 'black box' models have only recently been introduced to the study of lung mechanics, and offer certain advantages when the system under study exhibits significantly nonlinear behaviour.

### 2.2.2 Modelling the static mechanics

The static mechanics of the lung are determined by its elastic properties. The elastic behaviour is the deformation in response to an applied stress, or alternatively, the stress in response to an applied deformation. Many models attempt to generate bulk and shear moduli which match observation. The bulk modulus of the lung is nearly an exponential function of the pressure, and the shear modulus is nearly a linear function of the pressure, with the bulk modulus much greater than the shear modulus (78).

***The lung tissue as an elastic continuum***

In 1970, Mead et al. (101) introduced the basic concepts of modelling the parenchyma as an elastic continuum consisting of a mesh of interconnected membranes idealised as a 2-dimensional network of springs. This concept was soon extended mathematically by Wilson and Lambert (79,174) and later followed by a large number of models with idealised geometries composed of substructural elements with specified elastic properties. In most cases, the elements were assigned strain energy functions based on measurements of tissue samples *in vitro*. By relating the bulk strain field to the strain experienced by individual elements within the model, the resulting bulk deformation behaviour was calculated. Many different geometries have been employed in this manner such as cubes, (166), spheres (39,43), dodecahedrons (34,67,83) and circular line elements (147). The strain energy functions employed in these models have all been based on empirical fits to the stress-strain measurements of lung tissue. Wilson and Bachofen (175) developed a model for the alveolar duct in which recoil pressure arose from the combined effects of three terms: the extension of the tissue forming the alveolar duct entrance rings, the direct effects of surface tension, and a term arising from the distortion of the parenchymal geometry due to the action of surface tension on the tissue. The model was capable of accounting for the PV curve between 40% and 80% of TLC, but failed to agree at higher volumes, presumably due to the neglected role of the alveolar septal tissue. This model, like others (34,39,43,80,83,84,175), successfully described the uniform expansion of the lung, but overestimated the resistance to shear deformations. Stamenovic and Wilson (147) extended the model of Wilson and Bachofen to describe

nonuniform distortions and were able to reproduce appropriate estimates of the shear modulus between 20% and 80% of TLC.

Other models similarly based on idealised geometric structures, but which do not make use of strain energy functions, are those of Budiansky and Kimmel and colleagues (15,72). These models assumed linear incremental stress-strain behaviour for the rod elements of a pin-jointed dodecahedron, and treated the lung as an elastic continuum in which the macroscopic strain field is identical to the strain experienced by the sub-structure. Most of these models assumed that surface tension was incorporated into the loading of the sub-elements. These models were made of statically indeterminate structures, that is, they required a prestress to resist collapse. This corresponds to the normal condition of the lung which is always under tension. These models represent a significant advance since their resistance to shear deformation depends primarily on the inflation pressure as has been observed experimentally, rather than on the constitutive properties of the elements (144). However, each model (15,72) represents the mechanical behaviour of the lung in terms of a single alveolus, and thus does not incorporate effects due to parenchymal interdependence (101).

***Finite element models***

West and Matthews (172) were the first to formally apply the finite element method to the analysis of the lung. They examined the three dimensional deformations and stresses induced within a vertical wedge of lung by its own weight. The elements of the model were assigned nonlinear elastic properties similar to those obtained from tissue strips (129). Liu and Lee (85) extended the model and obtained results more closely matching the measured data. Other models employed finite element methods and demonstrated the necessity of explicitly including surface tension (67,164). Some models of this type have attempted to incorporate physiologic variability by the use of stochastically distributed substructures. Frankus and Lee (34) constructed a dodecahedron-based model with faces upon which were distributed straight, randomly oriented fibres which could be simplified to that of an 'equivalent fibre', with stress-strain properties like that of alveolar wall. Other models which make use of the finite element

method are discussed below (28,77,80).

***Fibre recruitment models***

The idea that elastin determines the stress-strain behaviour of lung parenchyma at low strains while collagen takes over as strain increases is well known, first having been introduced by Setnikar (137) and extended later by Mead (98). More recently there have been a few studies that explore this idea in a quantitative fashion. For example, Fung (41,42) used a linear expression for the constitutive equation for elastin together with an exponential function for collagen. The two fibre types were assumed to be distributed probabilistically according to observed distributions of fibre diameter and curvature. This gave a tissue strain energy function from which the incremental material constants were calculated according to the theory of continuum mechanics. Suwa et al. (161) ascribed the origin of the curvilinear stress-strain relationship of lung parenchymal strips to the reorientation of the constituent fibres, where a fibre does not support load until oriented in the direction of the applied strain. Models based on the gradual recruitment of kinked or 'wavy' fibres were proposed by Soong and Huang for human alveolar wall (143), and by Decraemer et al. (27) for various biological soft tissues. Lanir (81) developed an analytical expression based on fibre recruitment which was shown to be compatible with the quasilinear theory of viscoelasticity (described below) – but only with extension, not during decreasing stretch. These models consisted of only one fibre type, elastic collagen, and assumed a specific functional form for the distribution of fibre lengths rather than estimating the distribution from the available data. For general soft biological tissues of more than one fibre type, Lanir (81) derived relations which describe the force extension behaviour of fibrous tissues from summation functions over the orientation distribution and waviness distribution functions. However only a simplified version in which the fibres were lumped into an equivalent fibre and isotropically and uniformly distributed was considered for lung tissue (80). Brown et al. (14) studied ligamentum propatagiale from birds and discussed a model in which the collagen fibres had distributed initial waviness, in parallel with elastin fibres. Although they did not develop the model mathematically, they concluded that it may represent an important factor in distensible

tissues, but it was probably not the predominant mechanism in ligamentum propatagiale. Based on the model of Kowe et al. (77), Denny and Schroter (28) recently constructed a model for the alveolar duct - including collagen and elastin fibres of 3 different diameters for different alveolar locations - based on the densities of collagen and elastin fibres found in dog lungs (117). They used a particular stress-strain relationship for the collagen fibre bundles which they assumed arose from gradual recruitment of tensed collagen fibres within a bundle. They simulated the effects of elastase and collagenase which disrupt the elastin and collagen networks respectively and found qualitative agreement with the measured behaviour of Karlinsky et al. (70) (see end of Section 2.1.4).

### 2.2.3 Modelling lung dynamics

Measurement of the mechanical behaviour of the lung is most often obtained by the measurement of pressures and flows at the airway opening. If the experiment is done with the chest closed, the total respiratory system mechanics are determined including the properties of the chest wall as well as the lung. If intrathoracic pressure is recorded via direct recording of the pleural pressure (1) or less invasively via the esophageal balloon technique (13,108), transpulmonary pressure can be obtained. The alternative is to conduct the experiment with the chest open (in animals, or in humans during open chest surgery), so that the surface of the lung is at atmospheric pressure, or to use excised lungs. Flow or pressure perturbations are applied most often at the airway opening (9,31,52,66,121,122), and sometimes at the body surface (30,47,123,159), or even at the alveoli (6,8,24,109), and the resulting pressure or flow is recorded.

Like the excised lung tissue described above, the intact lung exhibits complex mechanical dynamic behaviour that depends on frequency, perturbation amplitude, and lung volume (or operating pressure). The type of model used to characterise the observed behaviour depends in large part on the type of perturbation applied. Perturbations that have been used range from quasi-sinusoidal ventilation (82), sinusoidal perturbations of single or multiple frequencies (10,30,66,159), step changes in flow (9,73,139), broad

spectrum random noise (23,31,105), and pseudo-random noise with specifically chosen frequency components (52,53,89,121,157,160).

***Linear models***

The simplest and still the most popular model used to represent the passive dynamic mechanics of the respiratory system is the single compartment model with governing equation

$$P = R\dot{V} + EV + K_p, \tag{2-2}$$

where $P$ is pressure usually at the airway opening or transpulmonary pressure, $R$ represents resistance, $E$ represents elastance, $V$ and $\dot{V}$ represent volume and flow respectively, while $K_p$ is baseline pressure. This model is depicted in Figure 2-1 and features $R$ as an idealised linear resistance gas flow (pipe), and $E$ as an idealised linear elastance (balloon). This model is only appropriate for a single frequency and a single operating pressure and oscillation amplitude.

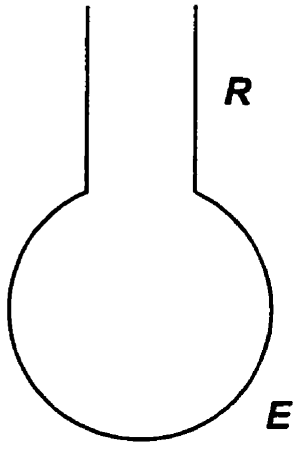


Figure 2-1. Single compartment linear model of the respiratory system, where R represents resistance and E represents elastance.

The frequency dependence of $R$ and $E$ stimulated Mount in 1955 (111) to introduce additional parameters in a rheologic model. His model contained an additional resistance and elastance connected in series to account for viscoelastic properties which he attributed to the tissues (Fig. 2-2A). In Figure 2-2A the lumped element resistances

and elastances are represented respectively by dashpots and springs. The spring and dashpot in series is commonly known as a Maxwell element, while the parallel combination is known as a Voigt element. Other models for lung mechanics based on ventilation inhomogeneity have been proposed, such as two balloons and pipes connected in parallel (119) or in series (99) (Fig. 2-2B and 2-2C). However, as Similowski and Bates (138) point out, the models of Figure 2-2 are mathematically equivalent. By using alveolar capsules in dogs, Bates et al. (11) showed that the tissue rheology model of Mount (111) was the most appropriate for the low frequency behaviour of the normal respiratory system. At higher frequencies it becomes necessary to add inertive elements to the models. In 1956, Dubois et al. (30) proposed a six element model which included inertances representing the inertia of the gas and tissues in a model for the respiratory transfer impedance. As the frequency range of perturbation studies increased to between 4 and 64 Hz, more complex linear models consisting of nine elements were postulated such as those of Peslin et al. (121). However, parametric models of this type pose great difficulties as there can be several canonical realisations, each of which can reproduce the data, but would invoke different physiological interpretations. Also, the requirements imposed on an experiment to obtain statistically reliable parameter estimates are quite stringent (88).

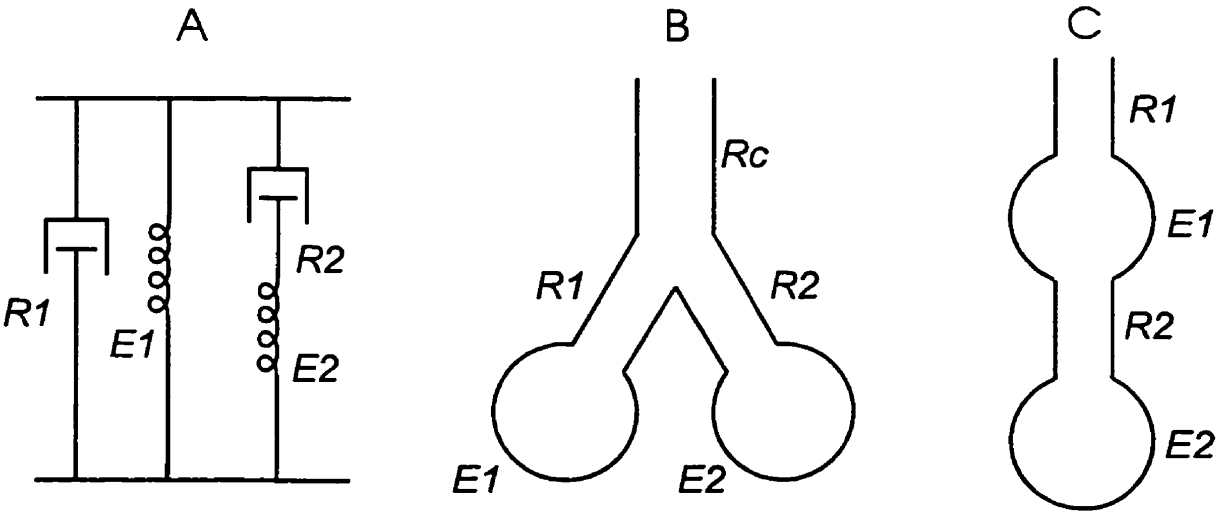


Figure 2-2. Two compartment linear models: A) rheologic model. B) parallel gas redistribution model C) serial gas redistribution model.

Modelling of the respiratory system in the low frequency range near the breathing frequency has been of considerable interest because of its obvious physiological relevance. In this range, much of the impedance to breathing is due to the tissues. Indeed, through the use of the alveolar capsule technique, Ludwig et al. (86) showed that tissue resistance can account for most of the lung resistance in dogs at low frequencies. This was particularly true at high lung volumes, where the tissue resistance accounted for 69-86% of the total lung resistance at 1 Hz oscillations. At a lower frequency, 0.5 Hz, the percentage of total lung resistance due to the tissues was even greater, and at a higher frequency, 2 Hz, the percentage was less.

Similar to the behaviour of excised lung tissue specimens, the lung displays stress adaptation in response to step changes in volume (57,58). In 1970, Hildebrandt (58) measured the stress adaptation of cat lungs filled with both air and saline, and found that the stress-relaxation following a step change in volume decayed with the logarithm of time as

$$P(t)/\Delta V = A_h - B_h \ln(t), \tag{2-3}$$

where $\Delta V$ is the size of the step change in volume, and $A_h$ and $B_h$ are constants. The frequency domain version of this equation was found to accurately predict the oscillatory behaviour between 0.125 and 5 Hz in dogs (52), and between 0.01 and 1 Hz in humans (151). Hildebrandt (58) modelled this behaviour with lumped elements using an infinite series of spring-dashpot pairs (see Fig. 2-3 below), for which a hyperbolic distribution of time constants has been shown to be able to predict Eq. 2-3 (40).

Fredberg and Stamenovic (37) noted that the ratio between the dissipative and elastic parts of lung tissue impedance were well conserved across species, and was nearly independent of frequency and oscillation amplitude. Accordingly, they introduced the structural damping hypothesis, which relates the dissipation and elastic storage of energy through a single constant which they called tissue hysteresivity, $\eta$, where

$$\eta = \omega R/E \ . \tag{2-4}$$

This hypothesis implies that energy dissipation and storage in lung tissue are intimately coupled. They also showed that Eq. 2-3 leads to a weak negative frequency dependence of $\eta$, and stated that this was not incompatible with observations from Hildebrandt (37,58).

As an alternative to Eq. 2-3 to describe the dynamic behaviour of the tissue strip, Hantos et al. (55) introduced the constant phase model

$$Z(\omega) = \frac{G_t - iH_t}{\omega^{\alpha_t}}, \tag{2-5}$$

where $Z(\omega)$ is the mechanical impedance of the lung tissues, $G_t$ and $H_t$ are coefficients of damping and elastance, $i$ is the positive square root of -1, and

$$\alpha_t = (2/\pi)\arctan(H_t / G_t). \tag{2-6}$$

Both elastic and dissipative parts of $Z(\omega)$ follow the same frequency dependence, and the phase is independent of frequency. Note that this is a two-parameter model like equation 2-3. This model was used in other studies as a tissue compartment for the lungs and chest walls of cats (51) and for dog lungs (54,90,125). In the time domain, the step response of the constant phase tissue model is

$$P(t)/\Delta V = ct^{-d}, \tag{2-7}$$

which is essentially identical to the description of stress-relaxation in elastic balloons given by Hildebrandt (57). Equation 2-7 is almost equivalent to Eq. 2-3, provided that the constant $d$ is small (8,154).

Eq. 2-7 is perhaps more compatible with the structural damping hypothesis (Eq. 2-4) than is Eq. 2-3, since in the frequency domain version of Eq. 2-7 (Eq. 2-5), $\eta$ is simply the ratio of $G_t$ to $H_t$, which is completely frequency independent. Suki et al (154) developed a mathematical framework for the basis of the constant phase model. They showed that one could develop this model by replacing ordinary time derivatives with fractional derivatives, and introduced a new constitutive element called the springpot based on the fractional calculus as defined by Koeller (74). The stress response of the springpot is determined by the fractional derivative of the strain which incorporates

dependence on the past strain with a fading memory, rather than the instantaneous derivative of integer calculus. A physical basis for this model was provided from models of polymer viscoelasticity, which take into account the complexity and statistical nature of the motion of long polymer chains (154). In particular, models of branched polymers are able to predict stress relaxation of the form of Eq. 2-3.

***Nonlinear models***

Ever since the first quantitative experiments on respiratory mechanics were performed by Fritz Rohrer in the period from 1915 to 1925 (118), nonlinear phenomena have been recognised as an important aspect of lung behaviour. Rohrer proposed the nonlinear flow model for a pressure drop across the lungs

$$P = K_1\dot{V} + K_2\dot{V}|\dot{V}|, \tag{2-8}$$

where $K_1$ and $K_2$ are constants. $K_1$ represents laminar resistance in a rigid tube to flow, while $K_2$ is a second constant related to the density of the gas, and represents the degree of nonlaminar flow in the airways (98). However, interest in modelling the nonlinear aspects of the tissues did not arise until much later, due likely to improvements in ease of analysis with the onset of computer techniques. Hildebrandt (58) noted that by employing the Fourier transform of Eq. 2-3, the stress relaxation data was not able to predict the total amount of hysteresis observed when the same lungs were oscillated at different frequencies. He concluded that additional energy was being dissipated plastically, and introduced a parallel viscoelastic plastoelastic model (Fig. 2-3) in order to account for the discrepancy. The viscoelastic compartment consisted of an infinite series of Voigt elements (with additional series springs), while the plastoelastic compartment was a series of Prandtl bodies (with additional series springs), each consisting of the parallel arrangement of a spring and coulomb 'dry friction' element. The dry friction elements behave nonlinearly as they only move when a certain yield force is reached, upon which they dissipate energy at a rate independent of motion. This differs from the dashpot which is a linear element and dissipates energy proportional to the rate of motion. The Hildebrandt model (58) was tested by Stamenovic et al. (144), who concluded that both

plasticity and viscoelasticity were important determinants of the mechanical behaviour of the respiratory tissues at low frequencies.

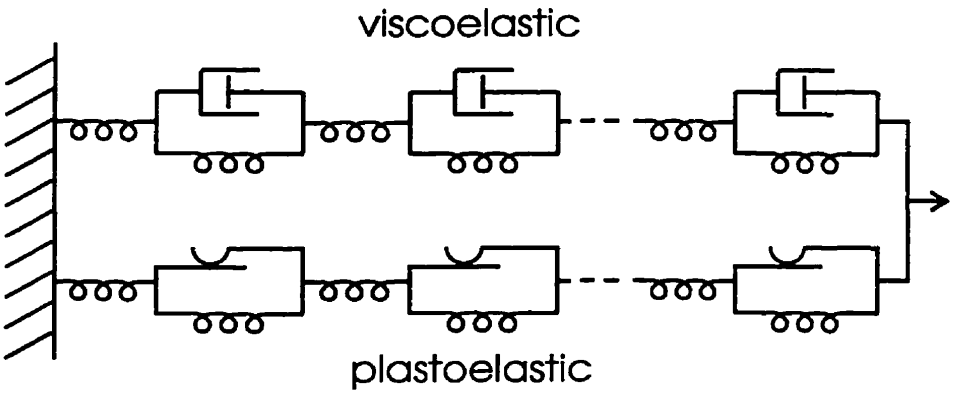


Figure 2-3. Hildebrandt nonlinear model for lung mechanics, consisting of an infinite series of Voigt bodies with a distribution of time constants, in parallel with an infinite series of Prandtl bodies with a distribution of yield points.

More recently Stamenovic et al. (145) developed an improved model which reduced the number of fitted parameters from 8 to 4. They found that the model fitted stress relaxation and oscillation data from human chest wall fairly well, but did not account for all the amplitude dependence observed in excised cat lungs. An important difference from the earlier study was that the plastoelastic and linear viscoelastic compartments (similar to those in Fig. 2-3) were mechanically coupled in a serial arrangement, rather than mechanically decoupled (parallel). A feature of this model is that amplitude and frequency effects are not separable, whereas they are in the Hildebrandt model. However, Suki and Bates (155) realised that the combination of plastoelastic and linear viscoelastic components was not necessary to explain the rheologic behaviour of lung tissues. Nonlinear viscoelasticity could, in principle, provide additional sources of dissipation not possible with linear viscoelasticity. Therefore, they developed a nonlinear viscoelastic model which could account for the amplitude-dependent behaviour observed in dog lungs subjected to sinusoidal perturbations (155). This model was based on the Volterra series, which is discussed in the following section.

Mijailovich et al. (107) developed a viscoplastic model that provided a mechanistic basis for the empirical model proposed by Hildebrandt (58). The viscoplastic model was based on a single fibre interacting with its neighbours. A fibre was modelled as a linear elastic element, which may slip once a certain yield force is achieved. Once in motion, the fibre dissipates energy both plastically (independent of strain rate) and viscously (proportional to strain rate). The model predictions were in qualitative agreement with some of the observed rate and amplitude dependencies of E and $\eta$. However, not all the amplitude and frequency dependencies of $\eta$ were accounted for, and the predicted relaxation response approached Eq. 2-3 only over a limited range.

## 2.3 Wiener and Hammerstein block structured modelling

The Wiener or Hammerstein models (Figure 2-4) consist of static nonlinearities in series with dynamic linear systems. In the Wiener model the linear dynamic block is followed by a static nonlinearity, while in the Hammerstein model the blocks are reversed. In their most general form these models are nonparametric, i.e. a 'black box' which does not represent anatomical features of the system it describes. However, Wiener and Hammerstein models can also be represented in parametric form, if appropriate *a priori* information about the system is available. Only parametric forms of Wiener or Hammerstein models been applied to respiratory mechanics.

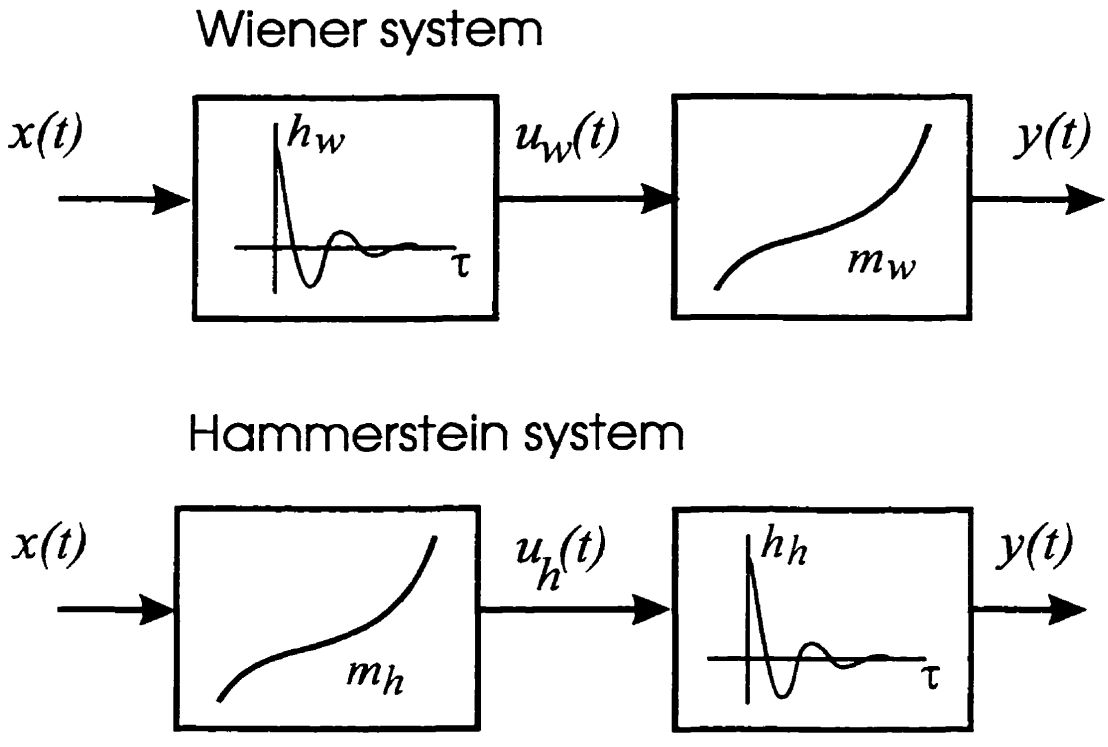


Figure 2-4. Wiener and Hammerstein block structured models. The Wiener system features a linear dynamic system followed by a static nonlinearity, while the Hammerstein system has the order reversed. See text in Section 2.3.2 for explanation of symbols.

### 2.3.1 Block structured modelling

The Wiener and Hammerstein models are but a small subset of a class of nonlinear models that can have Volterra series representations. The Volterra series relates the output $y(t)$ of a system to its input $x(t)$, via cross-correlations of system functionals with the input of increasingly higher order as

$$y(t) = h_o + \int_0^\infty h_1(\tau)x(t-\tau)d\tau + \int_0^\infty\int_0^\infty h_2(\tau_1,\tau_2)x(t-\tau_1)x(t-\tau_2)d\tau_1 d\tau_2 + \int_0^\infty\cdots\int_0^\infty h_\infty(\tau_1,\cdots\tau_\infty)\left[x(t-\tau_1)x(t-\tau_2)\cdots x(t-\tau_\infty)\right]d\tau_1\cdots d\tau_\infty \quad , \qquad (2\text{-}9)$$

where $h_o$, $h_1$, ... $h_\infty$ represent the Volterra series kernels of increasing order, and it is assumed that $x(t)$ is zero for $t < 0$. Note the integrals need only be evaluated to some time

greater than the memory length of the system kernels. The Volterra series can describe any physically realisable nonlinear system with fading memory which is single input - single output and time invariant. It cannot however describe systems that exhibit infinite memory behaviour such as plastic hysteresis (76). As special cases of the Volterra series, the Wiener or Hammerstein models also share this limitation and can only represent systems which contain static nonlinearities in series with dynamic linear behaviour, but they cannot model systems with complex dynamics in the higher order kernels. In a Hammerstein model, the higher order kernels may be non-zero only along the main diagonals (76), while in the Wiener model, the kernels may have off-diagonal components. If the system under study is more complex, sophisticated approaches may be used to identify the higher order dynamics. An excellent review of current methods to identify more general systems with Volterra series representations can be found in the Ph.D. thesis of Westwick (173).

### 2.3.2 System identification techniques

***Linear systems***

The output of a physically realisable linear system to an arbitrary input can be completely represented by the convolution of the input with the system impulse response as

$$y(t) = \int_0^{\infty} h(\tau)x(t-\tau)d\tau, \tag{2-10}$$

where $h(\tau)$ is the impulse response, the lower limit of zero in the integral indicates the system is causal, and the upper limit need only be as great as the length of the impulse response function. The input-output cross-correlation $\phi_{xy}$ can be shown to be related to the input auto-correlation $\phi_{xx}$ and $h(\tau)$, expressed here in discrete time as

$$\phi_{xy}(\tau_k) = \Delta t \sum_{j=0}^{T-1} h(\tau_j)\phi_{xx}(t_k - \tau_j), \tag{2-11}$$

where $\Delta t$ is the sampling interval, and $\phi_{xx}$ is calculated for the same memory length $T$. If the input is white, then the $\phi_{xy}$ is proportional to the $h(\tau)$. If the input is non-white, $h(\tau)$ can be solved for directly using Toeplitz matrix inversion (62), written compactly as

$$h(\tau) = \phi_{xy} / \phi_{xx} \quad . \tag{2-12}$$

Other methods exist for identifying linear systems in parametric form; however I am primarily interested in the non-parametric identification of the linear blocks within the Wiener or Hammerstein models.

***Wiener model***

Hunter and Korenberg (63) developed an iterative identification technique for the Wiener model, which is shown in the upper panel of Figure 2-4. In their technique, the linear impulse response function $h_w(\tau)$ is identified between the input $x(t)$ and output $y(t)$ in discrete time using Toeplitz matrix inversion. Next, the output of the linear block $u_w(t)$ is generated using Eq. 2-11, and a nonlinear polynomial $m_w$ is fitted in the least-squares sense between $u_w(t)$ and $y(t)$. The signal $u_w(t)$ is then re-estimated from $y(t)$ through the inverse of $m_w$, and a re-estimate of $h_w(\tau)$ is fit between $x(t)$ and $u_w(t)$. The intermediate signal $u_w(t)$ is then re-estimated in the forward direction from $x(t)$ and $h_w(\tau)$, and the procedure is repeated until the improvement in the percent variance accounted for (VAF%) between $y(t)$ and the predicted model output in successive subsequent iterations falls below some desired level. The VAF% is calculated as

$$\text{VAF\%} = 100\left(1 - \frac{\text{var}(y(t) - \hat{y}(t))}{\text{var}(y(t))}\right), \tag{2-13}$$

where var() is the variance of the bracketed quantity and $\hat{y}(t)$ is the model predicted output. The above scheme identifies $h_w(t)$ and $m_w$ to within a scale factor. That is, if $h_w(t)$ and $m_w$ are the solution to the system then so are $h_w(t)/a$ and $am_w$ for arbitrary $a$.

***Hammerstein model***

The block diagram for the Hammerstein model is shown in the lower panel of Figure 2-4. The Hammerstein model fitting process is very similar to that of the Wiener model. It is only summarised here and can be found in greater detail in Hunter and

Korenberg (63). Essentially it begins with estimation of an inverse of the impulse response function $h^{-1}_h(t)$ as if the system under study generated $x(t)$ from $y(t)$. By convolution of $y(t)$ with $h^{-1}_h(t)$ via Eq. 2-11, an estimate of the intermediate signal $u_h(t)$ is obtained and a polynomial $m_h$ is fitted between $x(t)$ and $u_h(t)$. Estimates of $h_h(t)$ are generated via Eq. 2-12 applied to $u_h(t)$ and $y(t)$. The process iteratively estimates $h^{-1}_h(t)$, $u_h(t)$ and $m_h$ using the same convergence criteria as for the Wiener model. Again, similar to the Wiener model, the estimates of $h_h(t)$ and $m_h$ are known to within a scale factor.

### 2.3.3 Wiener and Hammerstein models applied to lung mechanics

Only recently has attention been paid to block structured models of the Wiener or Hammerstein type for describing biomechanical systems. The Hammerstein model has been successfully used in parametric form to describe the length-extension behaviour of several biological tissues by Fung (40), and to describe oscillation dynamics and step responses of diaphragm strips (115) and parenchymal strips (64). The model of Fung is known as the quasilinear viscoelastic model, since for a step change in the input, the amplitude dependence of the response is nonlinear and elastic while the time-dependent relaxation is linear. The implementation of quasilinear viscoelasticity by Navajas et al. (115) consisted of an exponential function of strain for the elastic response and time-dependent behaviour modelled according to the Hildebrandt linear step response, Eq. 2-3. Thus the elastic response is

$$\sigma = \sigma_r e^{\alpha_n(\lambda-\lambda_r)}, \qquad (2\text{-}14)$$

where $\sigma$ is the stress, $\alpha_n$ is a parameter of the model, $\sigma_r$ is the stress at an arbitrary reference stretch $\lambda=\lambda_r$, and $\lambda$ is defined as the ratio of the tissue length to the unloaded length. The stress response to a step change of $\Delta\lambda$ amplitude is from the Hildebrandt model (Eq. 2-3) leading to

$$\sigma(t)-\sigma_o = \sigma_o(e^{\alpha_n\Delta\lambda}-1)(1-\gamma_n \ln(t)) \quad , \qquad (2\text{-}15)$$

where $\sigma_o$ is the stress prior to the step and $\gamma_n = B_h/A_h$ from Eq. 2-3. Based on the Fourier transform of Eq. 2-15, the response to sinusoidal inputs was predicted and compared to

the measured oscillatory response in terms of $R$ and $E$, determined as per Fredberg and Stamenovic (37). This model fitted the data fairly well, but a slight decrease in $\alpha$ was observed with increasing step or oscillation amplitude, at odds with Eq. 2-15. This weak dependence on $\Delta\lambda$ may have arisen due to plasticity in the material (115). Suki et al. (160) used the Wiener and Hammerstein models as part of a block structured forward model used to simulate the effects of nonlinearities in respiratory mechanics. The model consisted of two parallel paths, a nonlinear airway compartment in parallel with a tissue compartment. The tissue was modelled as either a Wiener or Hammerstein system, consisting of a fourth order polynomial in series with a Kelvin body (mechanically parallel spring and dashpot in series with an additional spring). To my knowledge, Wiener and Hammerstein models were first used in identification of lung mechanics *in vivo* by Suki et al. (160). They measured lung mechanics in open-chested dogs before and after histamine infusion using sparse pseudo-random inputs. Several different model structures were tested in which the mechanical response was partitioned into separate blocks for the airways and tissues, connected in series or in parallel. Each block was given a parametric functional form and the parameters were fitted in a weighted least-squares sense. For the frequency and amplitude ranges they studied, a model consisting of a linear airway compartment in parallel with a Wiener model for the tissues provided the best fit to the data. The linear block of the Wiener model was the constant phase model (Eq. 2-5), while the polynomial nonlinearity was 3rd order. In addition, they found that modelling the airway compartment as a Rohrer nonlinearity (Eq. 2-8) did not improve the model performance compared to using a simple linear model for the airways.

# 3. One-dimensional elastic properties of the lung tissue strip

## 3.1 Introduction

The nonlinear stress-strain characteristic of the tissue plays a very significant role in the elastic recoil of the lung at normal breathing frequencies (148). It is commonly agreed that the main stress-bearing constituents of lung tissue are collagen and elastin fibres (135,144). As discussed in Section 2.1.2, these fibres differ significantly in their mechanical properties with collagen being 3 to 4 orders of magnitude stiffer than elastin. Furthermore, elastin is stretchable to greater than 250% of its original length before rupturing, while collagen can stretch merely 1-3%. The origin of the curvilinear stress-strain behaviour is thus generally thought to be one of collagen fibre recruitment. That is, elastin is responsible for load-bearing at low strains when much of the collagen is 'wavy' and therefore not contributing to the tension. As strain increases, the collagen fibres become straight and so progressively take up more load, thereby stiffening the tissue. However, it is currently unclear how to precisely translate alterations in lung tissue constituents into changes in tissue mechanical properties.

In this chapter, we develop a model for uniaxial static elastic stress-strain curve of the lung tissue strip. The model is based on the large differences in the mechanical behaviour of the stress-bearing constituents. We attempt to construct as simple a model as possible, but which still leads to the observed elastic behaviour. Thus, the collagen fibre is considered as a wavy string which does not extend once straight, and the elastin is represented as a linear Hookean spring. The collagen and elastin fibres are assembled in a series of string-spring pairs, which may stiffen upon extension only if we permit the relevant parameters (spring stiffnesses and the straightening length of the strings) of the elements to be distributed. Our interest therefore, is whether the model contains sufficient

features to describe the data, and if so, what are the forms of the element property distributions. To gather data for the model, we also measure the stress-strain properties of dog lung tissue strips submerged in an environmentally controlled tissue bath.

## 3.2 Methods

### 3.2.1 Analytic model development

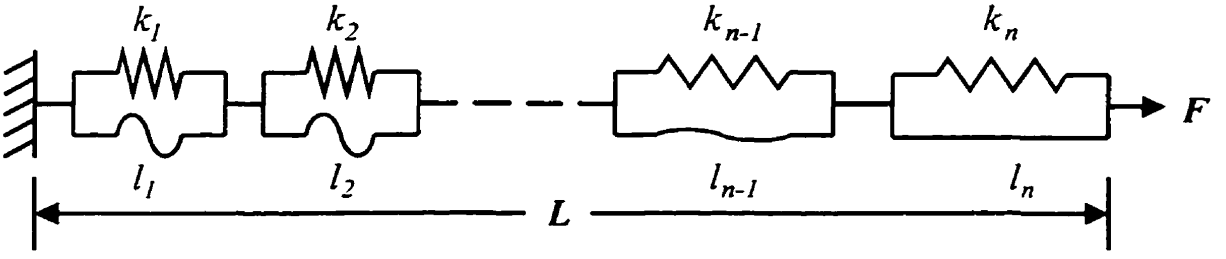


Figure 3-1. The series model of parallel spring-string elements extended to length, $L$ with force, $F$. The springs are identical with stiffness $k$, while the strings each have an associated stop length $l$ at which further extension is not permitted.

Consider the model of Figure 3-1. The model is constructed from a series of spring-string pairs where the springs represent elastin fibres and the strings represent collagen fibres. Each spring-string pair (unit) begins at resting length, with no load and flaccid strings. As the model is extended, each spring resists the applied force in a linear Hookean manner until its associated string becomes taut. The strings are inextensible, so further extension of the unit is impossible. We define the maximum extension of a unit as its 'stop length'. This is thus the difference between the maximum length of the unit and the resting length of the spring. As the model is stretched, the number of units that have reached their stop length increases, thereby progressively increasing the slope of the stress-strain curve. We will assume that the spring-string pairs are small and numerous so that their stop lengths and spring constants can be described in terms of continuous distributions.

***Distributed stop length model***

We consider the model of Figure 3-1 with identical spring constants for each spring-string pair, while the stop lengths are distributed. At rest there is no load on the model and its resting length is $L_r$. When the model is extended to length $L > L_r$, all the units with stop lengths less some value $l_o$ will have become stopped. The length of the model is then the sum of 3 terms,

$$L = L_r + L_s + L_u, \tag{3-1}$$

where $L_s$ is the combined extensions of all the stopped units, and $L_u$ is the length contribution of the remaining units. The stop lengths, $l$, are distributed according to a density distribution $N(l)$. Eq. 3-1 becomes

$$L(l) = L_r + \int_0^{l_o} lN(l)dl + l_o \int_{l_o}^{\infty} N(l)dl. \tag{3-2}$$

In the third term representing all those units which are not stopped, each unit is at length $l_o$ since all $k$ are identical and all the units of the model share the same force, $F$. As the model is lengthened, $l_o$ increases and more units become stopped. Differentiating, we have

$$\frac{dL}{dl_o} = \int_{l_o}^{\infty} N(l)dl, \tag{3-3}$$

which gives the model compliance

$$\left.\frac{dL}{dF}\right|_{l_o} = \frac{dl_o}{dF} \int_{l_o}^{\infty} N(l)dl, \tag{3-4}$$

where $dl_o/dF$ is the compliance of the string-spring unit that has just become stopped. We have defined this compliance to be the same for all units, thus

$$\frac{dl_o}{dF} = \frac{1}{k}. \tag{3-5}$$

Differentiating Eq. 3-4 with respect to $l_o$ gives

$$\frac{d}{dl_o}\left(\left.\frac{dL}{dF}\right|_{l_o}\right) = -\frac{1}{k}N(l_o)$$
$$= \frac{d}{dF}\left(\left.\frac{dF}{dl_o}\frac{dL}{dF}\right|_{l_o}\right) \quad (3\text{-}6)$$

Recognising that this is true for every value of $l_o$, and substituting in for $dl_o/dF$ from Eq. 3-5 we have

$$N(l) = -k^2\frac{d^2L}{dF^2}. \quad (3\text{-}7)$$

Eq. 3-7 allows us to calculate $N(l)$ to within the arbitrary elastic constant $k$ from measurements of tissue force and length.

We note that Eq. 3-5 substituted into Eq. 3-4 and evaluated for $l_o = 0$ gives the initial slope of the length-tension curve. Thus

$$\left.\frac{dL}{dF}\right|_{F=0} = \frac{1}{k}\int_0^{\infty}N(l)dl$$
$$= \frac{X}{k}, \quad (3\text{-}8)$$

where $X$ is the total area under the stop length density distribution. We have no guarantee that $X$ will be finite, so we merely ensure that the upper limit of the integral in Eq. 3-8 is at least as great as the maximum extension of the tissue generating the data to which Eq. 3-7 is applied. In this chapter, we use an upper limit corresponding to a strain of 2 and a value for $X$ of 10 000, thus defining a value for $k$.

***Distributed stiffness model***

An alternate model based on Figure 3-1 can be developed in which the stiffnesses are distributed, but the stop lengths are identical for all spring-string units. Let $M(k)$ represent the stiffness density distribution. Eq. 3-1 now becomes

$$L(F) = L_r + l\int_0^{k_0}M(k)dk + F\int_{k_0}^{\infty}\frac{M(k)}{k}dk, \quad (3\text{-}9)$$

where $k_o$ is the stiffness of that unit which has just become stopped. Differentiating with respect to the force, we get the compliance of the model

$$\left.\frac{dL}{dF}\right|_{k_o} = \int_{k_o}^{\infty} \frac{M(k)}{k} dk \,. \tag{3-10}$$

Differentiating again with respect to $k_o$ gives

$$\begin{aligned} \frac{d}{dk_o}\left(\left.\frac{dL}{dF}\right|_{k_o}\right) &= -\frac{M(k_o)}{k_o} \\ &= \frac{d}{dF}\left(\frac{dF}{dk_o}\left.\frac{dL}{dF}\right|_{k_o}\right) \end{aligned} \,. \tag{3-11}$$

Since all units of the model experience the same force, equal to the force of the unit which has just reached its stop length, we have

$$F = k_o l \,. \tag{3-12}$$

Consequently

$$\frac{dF}{dk_o} = l \,. \tag{3-13}$$

Substituting Eq. 3-13 into Eq. 3-11 and recognising that the result holds for all values of $k_o$ gives

$$M(k) = -kl\frac{d^2 L}{dF^2} \,. \tag{3-14}$$

Eq. 3-14 allows us to calculate $M(k)$ to within the arbitrary stop length constant $l$ from measurements of tissue force and length.

We note that the maximum extension $L_{s,max}$, is given by

$$\begin{aligned} L_{s,\max} &= l\int_0^{\infty} M(k)dk \\ &= lY \end{aligned} \,, \tag{3-15}$$

where $Y$ is the total area under the stiffness distribution. Similarly to the case for the stop length distribution, we have no guarantee that $Y$ will be finite, so we fix the upper limit of the integral in Eq. 3-15 such that the maximum strain is 2 when $Y$ has a value of 10 000 thus determining $l$.

### 3.2.2 Experimental methods

We obtained a tissue strip from each of 5 different degassed dog lungs. The preparation and testing apparatus are also described elsewhere (93). Briefly, sub-pleural strips were taken from the left lobes which had been rinsed several times by injection and withdrawing of Krebs-Ringer solution into the bronchi with a syringe, and the pleura removed. The strips were cut to $L_r = 2.80 \pm 0.18$ cm, with a cross-section, $A_r$ of $0.230 \pm 0.025$ $cm^2$ (means ± std. dev.). Using a large length to width ratio (28 mm to ~ 4 mm) minimised the effects of distortion effects at the tissue ends. Unstressed length was measured with a vernier calliper in the tissue bath prior to attachment, and $A_r$ was determined from the mass and an assumed density of $\rho = 1.06$ $g/cm^3$ as $A_r = \text{weight}/(\rho L_r)$. Tissue samples were placed in a 220 ml tissue bath (Fig. kept at 37°C in continuously circulating Krebs-Ringer solution (in mM: 118 NaCl, 4.5 KCl, 25.5 $NaHCO_3$, 1.2 $MgSO_4$, 1.2 $KH_2PO_4$, 5.6 $C_6H_{12}O_6$, 2.5 $CaCl_2$; pH 7.4) bubbled with 95% $0_2$ and 5% $CO_2$. The gas diffuser and pump were placed in an overflow reservoir to minimise noise. One end of the strip was glued with cyanoacrylate to a semiconductor load cell attached to a wall of the bath. The load cell compliance was 75 μm at the full scale load of 50 g. The other end was glued to the coil of a linear motor which was computer controlled. The glue rigidly held the tissue to the surface of the attachments for forces far in excess of those occurring during measurements. Length was measured with a linear variable differential transformer (LVDT) attached to the motor coil. The frequency response of the motor was flat to 30 Hz for amplitudes less than 0.4 cm peak-to-peak decreasing to 15 Hz for 2 cm peak-to-peak. Force resolution was ~10 mg and length resolution was 13.6 μm. Signals were anti-aliased filtered to 10 Hz (8-pole Bessel), and sampled at 30 Hz on a 486 PC using a 12 bit A/D converter.

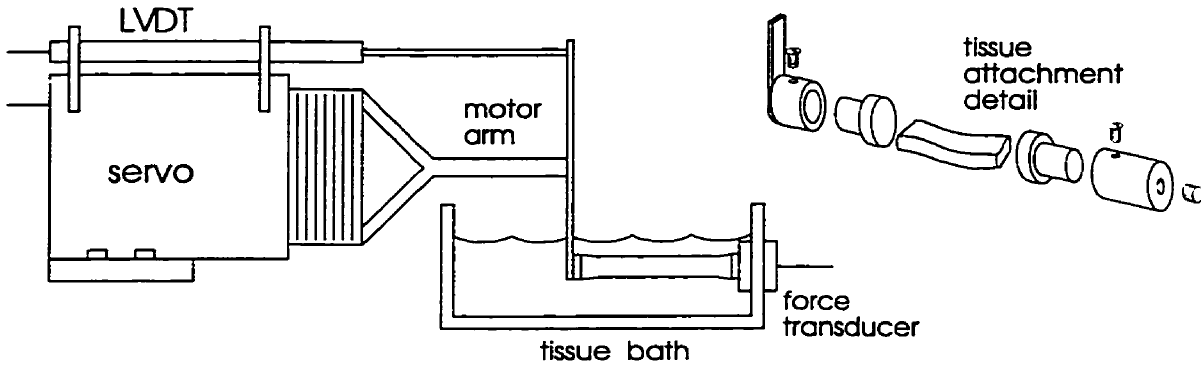


Figure 3-2. Tissue bath setup. The position of the motor arm is measured via the LVDT and servo controlled from the computer. The Plexiglas attachments are glued to the tissue prior to attaching to the transducer and motor arm via the set screws.

The tissue strips were preconditioned several times by slowly cycling at 2% $L_r$/sec between resting length and 5 kPa tension. The length-tension curves were obtained by straining the tissue at 0.5% $L_r$/sec from $L_r$ to greater than 100% strain. The length-tension curves from the five tissue strips were fitted to the function

$$\sigma = G(\exp(\varepsilon / H) - 1), \tag{3-16}$$

where $G$ and $H$ are fitted constants, $\sigma$ is the tissue stress defined by the measured tension $F$ divided by $A_r$, and $\varepsilon$ is the axial tissue strain where $\varepsilon = (L - L_r)/L_r$. Curve fits were obtained using the Marquardt-Levenberg algorithm implemented in SigmaPlot v. 2.0 (Jandel Scientific, Corte Madera, CA).

To calculate the stop length distributions (Eq. 3-7) and stiffness distributions (Eq. 3-14) from stress-strain tissue data, the following relationship was used to convert from stress-strain to length-tension:

$$\frac{d^2\varepsilon}{d\sigma^2} = \frac{A_r^2}{L_r}\frac{d^2L}{dF^2}, \tag{3-17}$$

where $L_r$ and $A_r$ are resting length and cross-sectional area respectively for each tissue strip.

### 3.2.3 Computer model simulations

We simulated the tissue models on computer by assigning spring and string properties to 10 000 units assembled in series. The length tension curves were calculated as follows. Each unit ceases extension at the stop length of the unit, at which point the force is equal to the product of $k$ and $l$, which we define as the 'stop force' of that unit. The units are rank ordered in terms of their stop forces. The model is then extended from rest and the total extension calculated in sequence at each stop force, thus forming a piece-wise linear length-tension curve. At each point in this curve, the length of the model is equal to the resting length plus the sum of the stop lengths of all stopped units plus the extensions of the unstopped units. Note that in choosing 10 000 units, we match the areas chosen for $N(l)$ and $M(k)$, thus permitting direct comparison with the analytic results, as the number of units is the discrete equivalent of the areas under the continuous density distribution functions. The simulated curves were converted from length-tension to stress-strain units using the means of the tissue areas and resting lengths (Table 3-1). These curves were then compared to a mean tissue stress-strain curve generated from the mean values of $G$ and $H$ from the 5 tissue strips via Eq. 3-16. Stress-strain curves were generated for the following different cases: (A) stop lengths varied among the 10 000 units while the stiffnesses were all identical, (B) stiffnesses varied while the stop lengths were all identical, and (C) both stop lengths and stiffnesses varied among the units.

## 3.3 Results

### 3.3.1 Application to lung tissue stress-stain curves

The 5 stress-strain curves from dog tissue strips are shown in Figure 3-3 with their curve fits according to Eq. 3-16. The parameters of the curve fits and the root mean squared (RMS) residuals for each curve are shown in Table 3-1.

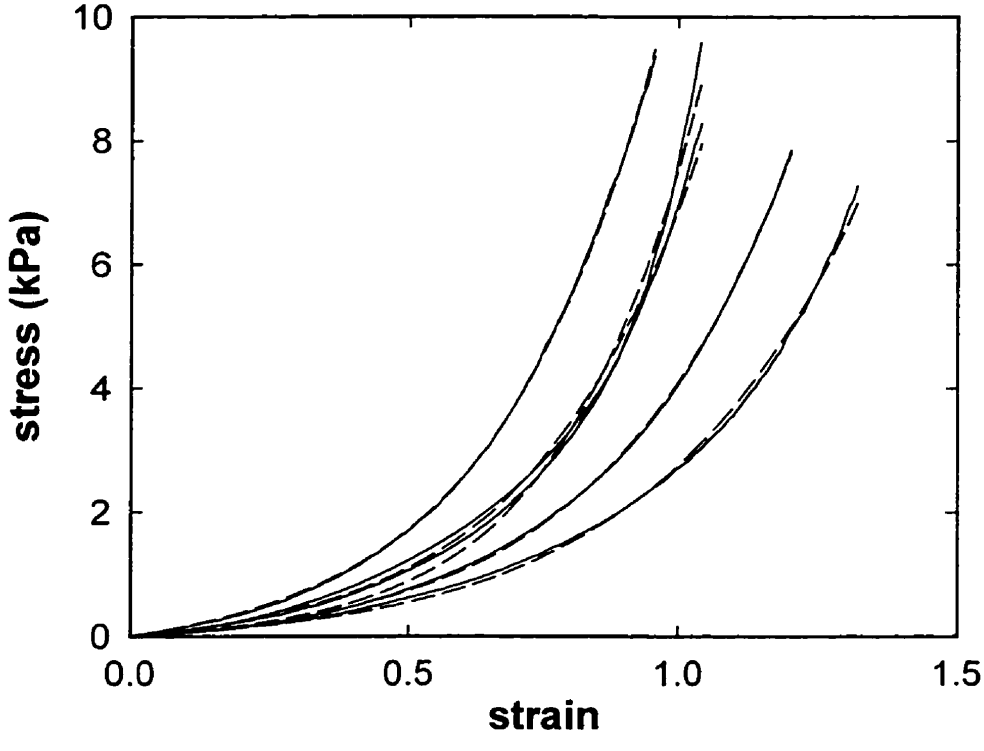


Figure 3-3. The five tissue stress-strain curves recorded at 0.5% of resting length extension per second (solid) with their curve fits according to Eq. 3-16 (dashed).

| tissue strip | $A_r$ ($cm^2$) | $L_r$ (cm) | G (kPa) | H | RMS residual (kPa) |
|---|---|---|---|---|---|
| 1 | 0.229 | 2.8 | 0.254 | 0.300 | 0.108 |
| 2 | 0.204 | 3.0 | 0.199 | 0.326 | 0.028 |
| 3 | 0.240 | 2.6 | 0.137 | 0.249 | 0.163 |
| 4 | 0.207 | 3.1 | 0.164 | 0.348 | 0.086 |
| 5 | 0.272 | 2.6 | 0.390 | 0.297 | 0.036 |
| mean | 0.230 | 2.8 | 0.229 | 0.304 | 0.088 |
| std. dev. | 0.025 | 0.2 | 0.100 | 0.037 | 0.055 |

Table 3-1. The parameters from the tissue strips and the curve fits of the tissue strip stress-strain curves to Eq. 3-16, with mean and standard deviations. The RMS residual is the root mean squared error from the fits.

Applying the distributed stop length model via Eqs. 3-7 and 3-17 to the stress-strain Eq. 3-16, the stop length distribution is

$$N(l) = \frac{L_r H}{\left(l + \frac{GA_r}{k}\right)^2}, \tag{3-18}$$

where $k$ is computed from Eq. 3-8 as

$$k = \frac{A_r GX}{L_r H}. \tag{3-19}$$

The resulting $N(l)$ for each tissue strip are shown in Figure 3-4, where the range of $l$ over which $N(l)$ is plotted corresponds to the measured forces from the relation

$$l = \frac{F}{k}. \tag{3-20}$$

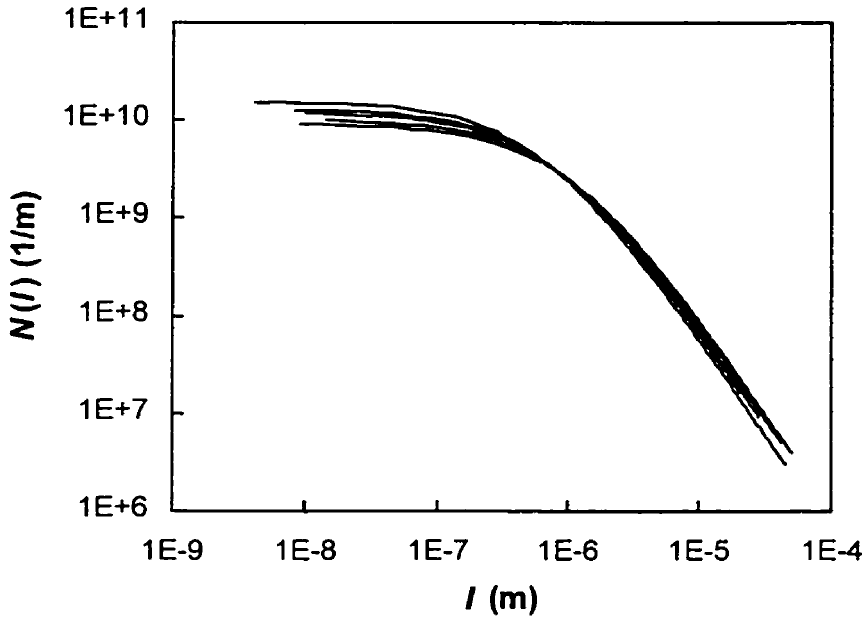


Figure 3-4. The stop length distributions $N(l)$, calculated according to the model from each of the curve fits to the tissue stress-strain curves.

Similarly applying the stiffness distribution model via Eq. 3-12, 3-14 and 3-17 to Eq. 3-16,

$$M(k) = \frac{kHL_r/l}{\left(k + GA_r/l\right)^2}, \tag{3-21}$$

where $l$ is calculated from Eq. 3-15 as

$$l = \frac{\varepsilon_f L_r}{Y}, \tag{3-22}$$

where $\varepsilon_f$ is the maximum strain of the model. In this case $k$ is our dependent variable and is chosen to correspond to the range of available data from the relation

$$k = \frac{F}{l}. \tag{3-23}$$

The resulting stiffness distributions for each of the tissue strips are shown in Figure 3-5.

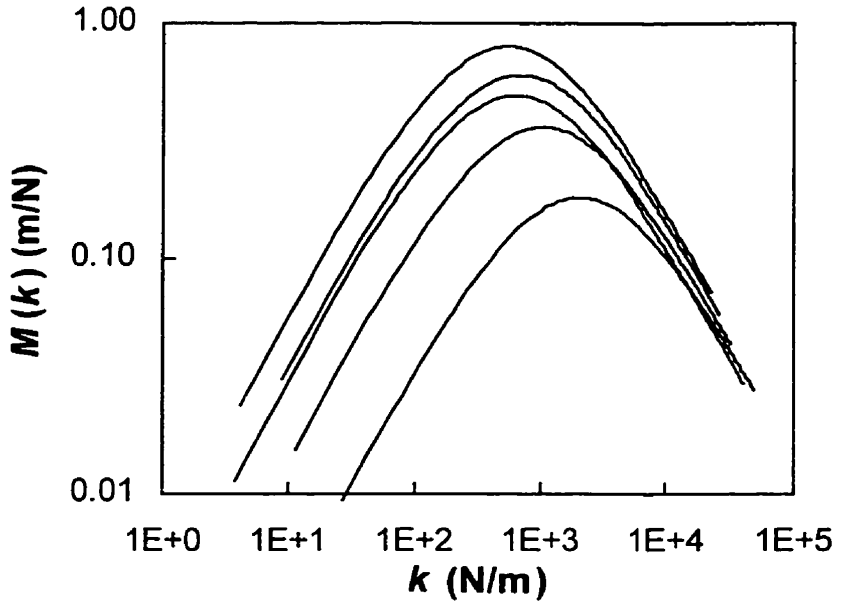


Figure 3-5. The stiffness distributions $M(k)$, calculated according to the model from each of the curve fits to the tissue stress-strain curves.

### 3.3.2 Computer simulations

Figure 3-6 shows the mean experimental stress-strain curve with curves generated using our 10 000 element numerical model. For the distributed stop length model, values for $l$ were randomly assigned according to Eq. 3-18 with $k$ chosen according to Eq. 3-19. The range of $l$ for the distribution function was between 0 and

$$\begin{aligned} l_f &= F_f / k \\ &= \frac{GA_r}{k} \exp(\varepsilon_f / H - 1)' \end{aligned} \tag{3-24}$$

where $F_f$ is the final force defined by $\varepsilon_f = 2$. In the distributed stiffness model stiffnesses were distributed according to Eq. 3-21, with $l$ from Eq. 3-22. The range of $k$ was limited between 0 and

$$k_f = F_f / l$$
$$= \frac{GA_r}{l} \exp(\varepsilon_f / H - 1), \tag{3-25}$$

where again $F_f$ is the final force defined by $\varepsilon_f = 2$. The distributions for the combination model were created according to Eqs. 3-18 and 3-21 respectively, with parameters altered so as to more closely match the mean tissue stress-strain curve. Specifically, the value of $k$ in Eq. 3-18 and in Eq. 3-24 decreased by a factor of 2 over the distributed $l$ model, and the value of $l$ of Eq. 3-18 and Eq. 3-25 was increased by a factor of 2 over the distributed $k$ model.

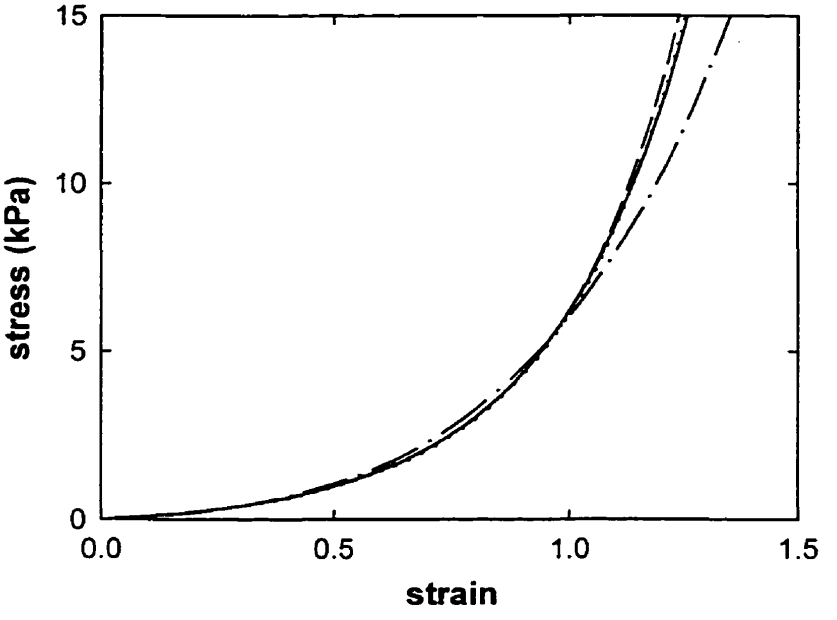


Figure 3-6. The stress-strain curve according to Eq. 3-16 from the mean parameter values for $G$ and $H$ from the five curve fits (solid), with the predicted curve from the simulated stop length distribution model (dotted) and the predicted curve from the simulated stiffness distribution model (dashed), and from the simulation of both stop lengths and stiffness distributed with stiffnesses halved and stop lengths doubled (dash-dot).

## 3.4 Discussion

We have described a model for interpreting static elastic behaviour of the lung tissue strip. Collagen is considered to be infinitely stiff compared to elastin. This is based on the observation that the incremental Young's modulus of collagen at typical strains is $6.8 \times 10^8$ dyn/cm$^2$ to $1.2 \times 10^{11}$ (40,56), while the Young's modulus of elastin is $1 \times 10^6$ to $8 \times 10^6$ dyn/cm$^2$ (41). In other words, collagen is 100 to 10000 times stiffer than elastin. We assumed a linear length-tension relationship for elastin as has been used in previous studies (2,28,41). This is justified because elastin exhibits its nonlinear behaviour outside the range of physiological strains (0.0~0.7) (17,134). Other components of the lung tissue which may contribute to its mechanics are the ground substance, smooth muscles and other cells. Brown et al. (14) proposed that the deformation of the ground substance may be a significant influence on the mechanical properties of tissue, although this remains to be tested. Therefore since this effect is not known, and since these substances have much smaller elastic constants than collagen and elastin (41), we do not explicitly incorporate the effects of ground substance in our model.

The idea that elastin determines the stress-strain behaviour of lung parenchyma at low strains while collagen takes over as strain increases is well known, first having been introduced by Setnikar (137) and extended later by Mead (98). More recently there have been a few studies that explore this idea in a quantitative fashion. For example, Fung (41) used a linear expression for the constitutive equation for elastin with an exponential function for collagen. The two fibre types were assumed to be distributed probabilistically according to observed distributions of fibre diameter and curvature. This gave a tissue strain energy function from which the incremental material constants were calculated according to the theory of continuum mechanics. Suwa et al. (161) ascribed the origin of the curvilinear stress-strain relationship of lung parenchymal strips solely to the reorientation of the constituent fibres where a fibre does not support load until oriented in the direction of the applied strain. As described in Chapter 2.2.2, models based on the gradual recruitment of 'kinked' or 'wavy' fibres were proposed by Soong and Huang for

human alveolar wall (143), and by Decraemer et al. (27) for various biological soft tissues. These models consisted of only one fibre type, elastic collagen, and assumed a specific functional form for the distribution of fibre lengths rather than estimating the distribution from the available data. Brown et al. (14) and Denny and Schroter (28) also considered the development of tension from distributed initial 'waviness' of collagen fibres, but did not develop it mathematically. Our approach however has a significant advantage over all of the above studies in that it allows us to determine functional forms for the distributions of elastin or collagen fibre properties from experimental stress-strain data, rather than having to assume these forms *a priori*.

The distributions of elastin fibre diameters were measured in human pulmonary alveolar walls of human lungs by Sobin et al. (142) and in alveolar mouths and ducts by Matsuda et al. (97). The distribution of elastin diameters would be expected to relate to our distribution of elastin stiffnesses, given that the stiffness of a fibre or fibre bundle is proportional to its cross-sectional area for a fixed Young's modulus. Thus a plot of the stiffness distribution functions versus the square root of stiffness should resemble a fibre diameter distribution function. This is borne out by the mean diameter distribution from our 5 tissue strips shown in Figure 3-6, which demonstrates a striking similarity to the data of Sobin (Fig. 3-8). Distributions of collagen fibre curvatures in the lung (97,142) are also similar in form to our stop length distributions, although it is not entirely clear how these two quantities relate.

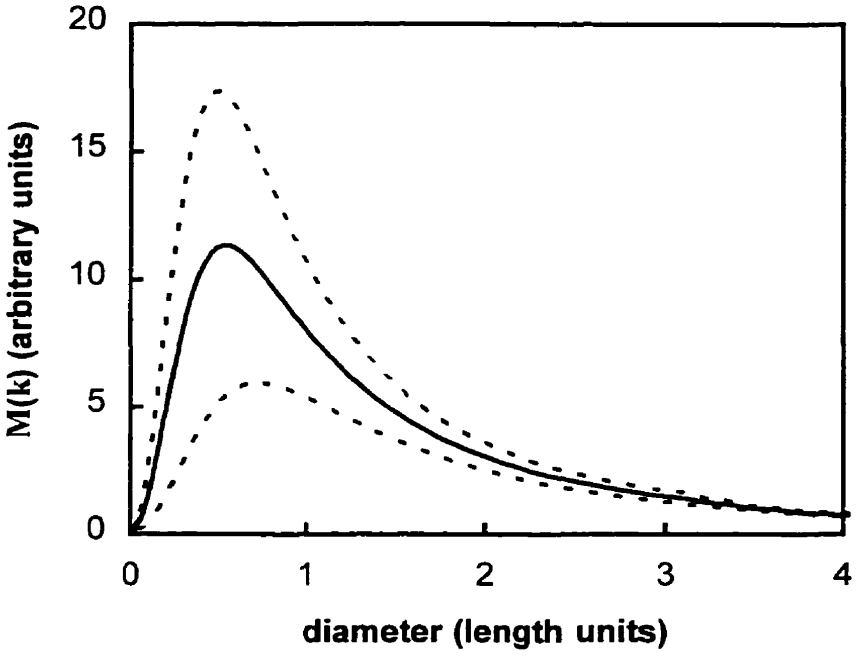


Figure 3-7. The mean stiffness distribution function (solid) with mean ± std. dev. (dotted) of the $M(k)$'s from Figure 4 plotted versus the square root of the stiffness $k$, which is proportional to fibre bundle diameter. The axes are arbitrarily scaled to more closely match the axes of Figure 3-8.

These morphological observations lend support to the model, but this does not imply direct correspondence between the strings and springs of our model and the individual components of actual tissue. The arrangement of the fibres in lung tissue is not only serial, but is also parallel and interwoven, forming complex interconnections (103). In fact, our stop length distribution may span multiple length scales. That is, the shorter collagen fibrils may correspond to the smallest stop lengths, but as many fibres become taut, a stop length may be formed from a cluster of collagen fibres (connected in parallel and in series), all reorienting and straightening against the load. Thus the distribution of stop lengths in our model may represent how the collagen matrix is arranged in a fractal sense.

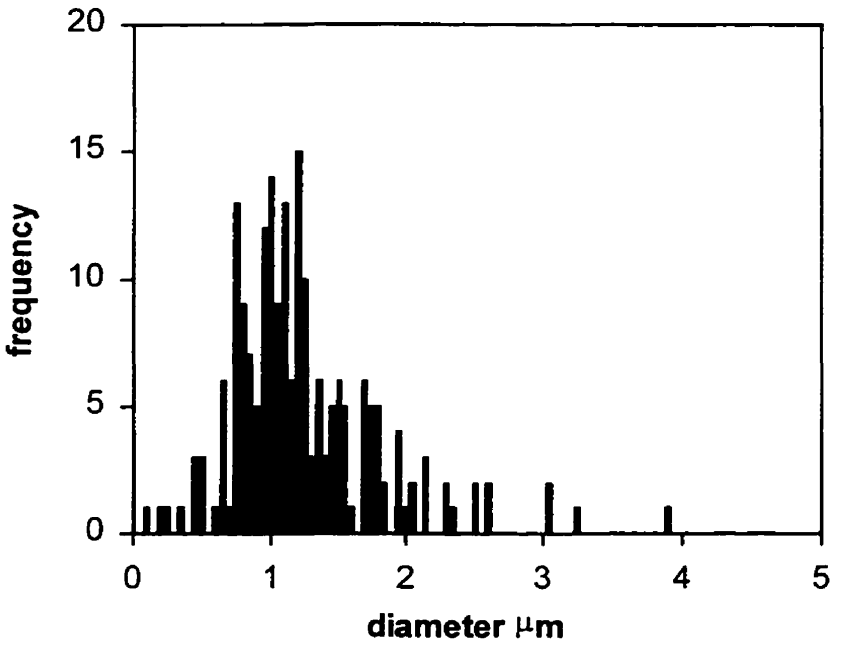


Figure 3-8. An example of a histogram of width of elastin fibre bundles in pulmonary interalveolar septa of a 75-year-old male subject inflated to a transpulmonary pressure of 14 $cmH_20$ reproduced from Sobin et al. (142).

In our model, the properties of collagen and elastin are considered independently, but their interaction is defined by their pair-wise coupling and serial connection. Mercer et al. (103) showed that elastin and collagen fibres are interwoven, especially in the alveolar entrance ring region, implying mechanical coupling of some kind. In fact, Mijailovich et al. (106,107) considered this interaction to be responsible for the observed dynamic viscoelastic properties of lung parenchymal strips in a model based on sliding filaments. It may thus be that interaction along the lengths of the fibres is responsible for dynamic tissue properties, while interconnections between the two fibre matrices with fibre properties distributed in a fractal-like manner are responsible for the static mechanics.

We note that for the large majority of the data (>95%) the distributions of Figures 3-4 and 3-5 are nearly power-law in form, manifest in the nearly linear tails where $N(l)$ is proportional to $1/l^2$ and $M(k)$ is proportional to $1/k$. There are other examples of inverse power laws exhibited by the lung. For example, the stress response of lung tissue strips to

a step change in strain exhibits power law dependence with time. Also, when strips are mechanically cycled over a range of frequencies the impedance amplitude is an inverse power law function of the cycling frequency (12). The lung inflation process has also been found to follow power laws, both as the magnitude of decreases in airway resistance measured from the terminal alveolar space and as the times between airway opening events (153). Complex systems with many varied elements interacting over a wide range of length scales tend to exhibit some measure or multiple measures in a inverse power law sense of the form $1/f^b$ with $0 < b < 2$, and $f$ is usually a distributed frequency, amplitude, or spatial measure. In particular, the inverse power law function often arises as the result of a cascade of smaller events that occur in a chain reaction (5,171). We hypothesise, therefore, that the bulk stress-strain properties of lung tissue are due in large part to some kind of fractal-like structure arising from biological self-organisation. This is responsible for the $1/f$ character found for our collagen and elastin distributions, which is a manifestation of general complexity.

In each of our models, the parameter of the element in parallel with the distributed parameter is identical for the entire model. That is, for the distributed stop length model the stiffnesses are fixed, while in the distributed stiffness model, the stop lengths are fixed. This is clearly not realistic, considering natural physiological variability in real tissue. We thus wondered how robust our models are to variability in the fixed parameters of each model. We therefore generated an $l$ distributed model as before (Eq. 3-18), but with the stiffnesses chosen randomly from uniform distributions having mean $k$ chosen as in Eq. 3-19 and with ranges from 0 to 100% of the mean. We found that the stress-strain curve changed only slightly, showing visible weakening from the mean tissue curve for ranges greater than 50% of the mean (Fig. 3-9, dashed lines). Similarly, we generated a stiffness distributed model as before according to Eq. 3-21 but with uniformly distributed $l$ of the same mean as the fixed $l$ model and with increasing ranges from 0 to 100% of the mean. Again, this caused little change in the stress-strain curve, with some stiffening observed at ranges greater than 50% of the mean (Fig. 3-9, dotted lines).

We therefore see that the model is robust to the introduction of variability in the fixed parameters. Nevertheless, it is obvious that both fibre types will be distributed in real tissue, as indicated by the data of Matsuda et al. (97) and Sobin et al. (142). We presumed that the forms of the collagen and elastin distributions are those given in Eqs. 3-18 and 3-21. However, each of these distributions accounts for the entire stress-strain characteristics independently. Thus in order to invoke both simultaneously, we softened their individual contributions by doubling all stop lengths and halving all stiffnesses. This produced a stress-strain curve that matched the mean experimental curve fairly well, dissociating only at high strains (Fig. 3-6, dot-dashed line).

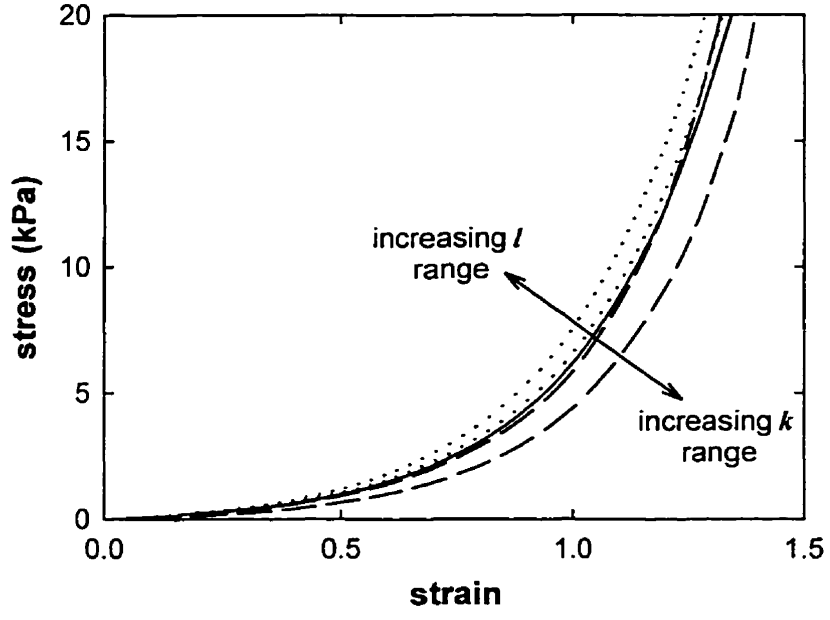


Figure 3-9. Dashed lines: The stress-strain curves calculated from simulation of the distributed stop length model with stiffnesses randomised with ranges of 50 and 100% of the mean. Dotted lines: The stress-strain curves from the distributed stiffness model with stop lengths randomised with ranges of 50 and 100% of the mean. The solid line represents the stress-strain curve according to Eq. 3-16 from the mean values of $G$ and $H$ computed from the 5 tissue strips.

### 3.4.1 Concluding comments

We have introduced a model that accounts for the nonlinear stress-strain curve of lung tissue based on the fundamental differences in behaviour of the structural constituent fibres. A mechanistic description is developed which quantitatively defines the relative roles of collagen and elastin fibres. The model predicts that the distributions for the collagen and elastin fibres are $1/f$-like for the large part of the data. The distribution found for the elastin fibres match the distributions found by Sobin et al. (142). We hypothesise that this reflects a fractal kind of organisation of the tissue constituents.

# 4. Two-dimensional finite element modelling of lung tissue elasticity

## 4.1 Introduction

Ever since the seminal work by Mead (101), it has long been recognised that the static elastic properties of the lung are derived not only from the properties of the underlying tissue constituents, but also from the way these constituents are organised. That is, as tissue is extended, the stiffness is much lower than would be predicted if the material were an isotropic solid. The lung tissue is made up of a complex interconnected network of fibres which are able to re-orient when a stress is applied. Some of the strain is thus taken up by this reorganisation. In the models of the previous chapter, this effect was incorporated by the straightening of formerly wavy or curved strings, taken to represent the straightening of collagen fibres. Once these fibres became taut, no further extension could occur. In lung tissue, both elastin and collagen may also reorient in the direction of the load, as may entire alveolar walls. Furthermore, collagen fibres which are straightened in an off-axis direction may still contribute to the stress through reorientation. This is commonly known as 'nylon stocking elasticity' coined by Bull (16). Thus, geometric effects are an important determinant of the elastic properties of lung tissue. In Chapter 3, we could account for the nonlinear nature of the stress-strain curve based on $1/f$ distributions of the properties of the constituent elements in one-dimensional models. In this chapter we investigate whether similarly distributed properties lead to the stress-strain curve of lung tissue in a two-dimensional finite element model.

## 4.2 Methods

### 4.2.1 The model

We construct the simulated tissue as a 2-dimensional finite element mesh consisting of interconnected spring-string pairs shown in Figure 4-1, where each line segment represents a given element pair. As in the models of Chapter 3, the springs are linear, but we replace the infinite stiffness of the strings by a finite stiffness much greater than that of the spring. Thus instead of a stop length, the fundamental mechanical spring-string unit has a 'knee' length. The length-tension relationship of a fundamental unit is indicated in Figure 4-2, and is given by

$$\begin{aligned} F &= k_1(l_g - l_r), && l_g \le l_k \\ &= k_2(l_g - l_k) + k_1(l_g - l_r), && l_g \ge l_k \end{aligned} \quad , \tag{4-1}$$

where $l_g$ is the length of the unit, $l_r$ is the resting length, $k_1$ and $k_2$ are the stiffnesses below and above the knee length $l_k$.

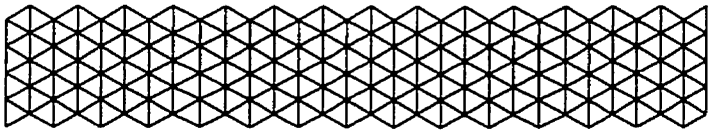

Figure 4-1. Example of 2-dimensional finite element mesh at rest where each line segment represents a spring-string pair (30x5 nodes, 381 elements).

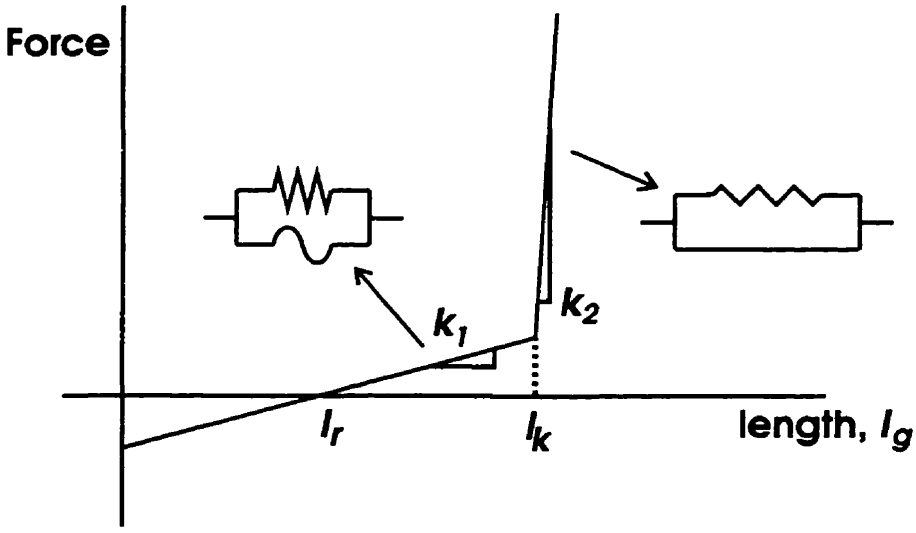


Figure 4-2. The force-length relationship for a single spring-string pair. For lengths below the knee length $l_k$, the spring constant of the unit is $k_1$ ,while for lengths greater than $l_k$, the spring constant is $k_2$. The resting length is $l_r$.

### 4.2.2 Simulation

The tissue simulation software was written in the Oberon language (created by Niklaus Wirth as a successor to Modula 2 and Pascal) (130) and followed an object-oriented programming style. Although the model could be coded in any language, Oberon was chosen as it is more concise than C++, has a very fast compiler, and is available freely from ftp.inf.ethz.ch. Program code was developed on both a PC-486/33MHz and IBM RS6000 model 320 computer, while the numerical simulations were run on an IBM RS6000 model 390 machine.

The solution algorithm initially attempted a simulated annealing approach (177). This method has the advantage of being extremely simple to code, and is known to be very robust in complex problems with nonlinearities (177). Briefly, the simulated annealing method proceeded as follows: First, the simulated tissue was stretched uniformly to the desired length. The energy stored within each of the units was calculated and summed, where the energy in a given unit is

$$Energy = 0.5k_1(l_g - l_r)^2, \qquad l_g \le l_k$$
$$= 0.5k_1(l_k - l_r)^2 + 0.5k_2(l_g - l_k)^2 + k_1(l_k - l_r)(l_g - l_k), \qquad l_g \ge l_k \quad . \quad (4\text{-}2)$$

Each node (intersection of the units) was then moved a random distance in a random direction and the total energy stored within the tissue was re-calculated. If the energy was less than the previous energy, the new node positions were accepted. If the energy was higher, then the node positions were accepted with a probability of less than one. The procedure was repeated with the random distances by which the nodes were translated being gradually decreased. This process mimics the cooling (annealing) of a metal, where the atoms may reach a minimum energy configuration provided that the rate of cooling is sufficiently slow. Unfortunately this method may take a long time to achieve adequate convergence.

A much greater rate of convergence (1-2 orders of magnitude) was found by using a version of the steepest descent algorithm, which makes use of the force gradient at the node positions. The tension within each of the elements at each iteration was computed according to Eq. 4-1, allowing the resultant force on each node to be determined. The nodes were then moved down their respective force gradient according to

$$\Delta Q = Q + \mu F, \quad (4\text{-}3)$$

where $\Delta Q$ is the change in node position from position $Q$, and $\mu$ is an adaptive parameter. If the value used for $\mu$ caused a decrease in the total energy of the entire tissue, then $\mu$ was increased by a factor of 1.01. Conversely, if the energy was increased, the new nodal positions were not accepted, and $\mu$ was decreased by a factor of 0.9 until the energy decreased. Thus, $\mu$ slowly increased when energy was decreasing, and quickly dropped when $\mu$ was too high. Convergence of this process was based on the principle that the same total force must be transmitted through each cross-section of the tissue when it is at its equilibrium configuration. Thus when the difference between the minimum and maximum axial cross-sectional forces along the tissue was less than 1 % of the average force, the tissue strip nodal positions were considered to have converged to the minimum energy positions, and the average force was taken as the tissue strip force at that level of

strain. Using some of the smaller model sizes tested, it was verified that the final node positions computed using the steepest descent method converged to the same positions as using the simulated annealing.

Tissue strips having length-to-width ratios like that of the measured strip of Chapter 3 were simulated. Model sizes of 30x5 nodes (381 elements), 60x10 nodes (1661 elements), and 90x15 nodes (3841 elements) were simulated. The properties of the elements were chosen according to the following four schemes:

A) identical $l_k$ with fixed $k_1$ and $k_2$,

B) identical $l_k$ with Gaussian distributed $k_1$ and $k_2$, keeping the same mean $k_1$ and $k_2$ as in (A),

C) power-law distributed $l_k$ distributed between limits of $10^{-5}$ and $10^{5}$ according to

$$P(l_k) = (l_k - l_r)^{-b} \quad , \tag{4-4}$$

with $b$ ranging from 0.1 to 2.0. Values for $k_1$ ranged between 0.01 to 1 with $k_2 = 100$, and at $k_1 = 0.1$, $k_2$ was either 10, 100 or 1000, and

D) selected examples from (C) with Gaussian distributed $k_1$ and $k_2$, keeping the same mean values of $k_1$ and $k_2$.

For Gaussian distributed spring constants, no spring constant was permitted to be less than zero, and $k_2$ was restricted to be greater than $k_1$ within a single spring-string pair. Since the units of length and force are arbitrary, length was normalised in all simulations to the resting length of the elements, which were all identical. Spring constants were similarly assigned unity stiffness defined by the generation of one unit of force per unit of extension. The Gaussian random deviates were generated according to the transformation method and power-law distributed deviates were chosen according to the rejection method (126). The node positions, element forces, and average axial force were monitored during the iterative process. Force-strain curves were generated by stepping the tissue from a strain of zero in steps of 0.05 to a strain of 1.25 (25 steps), and allowing the tissue to converge at each step.

## 4.3 Results and discussion

Calculation of force-strain curves took from 3 minutes to 16 hours, depending on the number of elements, distribution of $l_k$ and degree of nonlinearity. Generally the greater the ratio between $k_2$ and $k_1$, the longer was the convergence time. Figure 4-3 shows equilibrium node positions for simulated tissue with identical $l_k$ = 1.5, and identical stiffnesses, $k_1$ = 0.1 and $k_2$ = 10. The tissue narrows in the centre as the strain increases. The tissue begins to narrow rapidly at strains greater than about 0.5, which corresponds to the level at which the elements begin to exceed their knee lengths, and elements near the ends of the tissue begin to carry more stress than central elements due to the geometric distortion caused by the fixed end node positions. Figure 4-4 shows the same tissue strip as Figure 4-3 except that the spring constants are now chosen from Gaussian distributions about the same mean stiffnesses with 50 % standard deviations. The forces carried by each element vary considerably (indicated by the varying line thickness in Fig. 4-3), producing a heterogeneous force distribution within the tissue. Figure 4-5 shows the force length curves from the these two simulation examples. Each tissue strip follows nearly identical force strain curves, despite distributing stiffnesses about their respected mean values. The force-strain curves are essentially piece-wise linear, with a 'knee' at about strain 0.7. The curves are very much like that of Fig. 4-2, except that the knee in the curve has been translated to the right of that of a single unit. All of the units have $l_k$ = 1.5, and would each individually give a 'knee' at 0.5 on Fig. 4-5. This rightward motion of the knee is attributable to changes in orientation of the units, which contributes to the total strain.

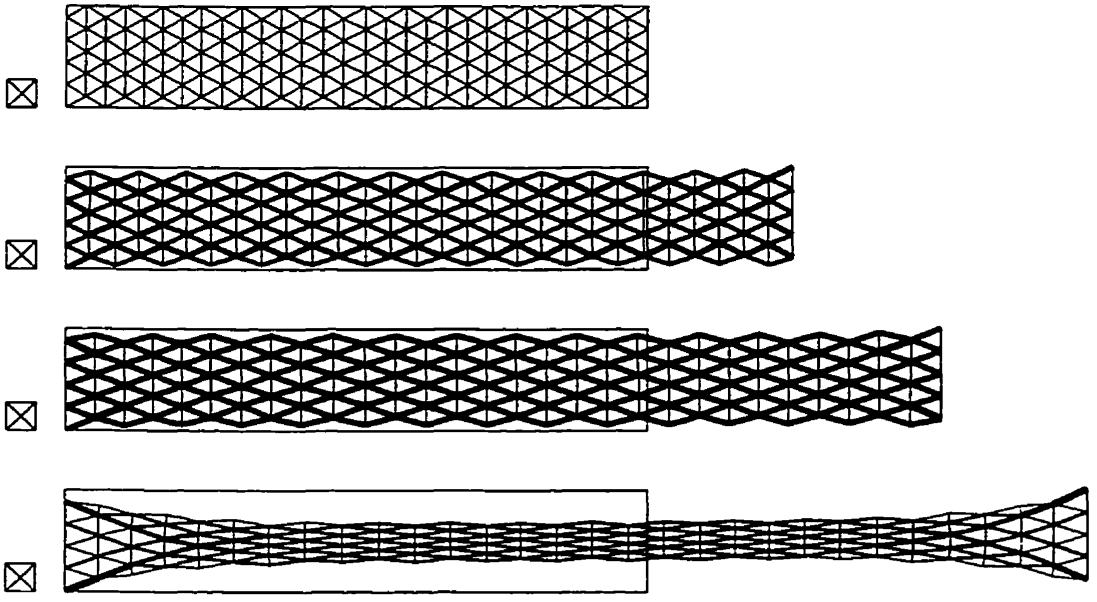

Figure 4-3. Simulated tissue (30x5 nodes) with $l_k$ = 1.5, $k_1$ = 0.1, and $k_2$ = 10, at extensions of 0, 0.25, 0.5 and 0.75 strain from top to bottom. The force in each element is coarsely indicated by the line thickness in the bottom three strips. The maximum force of all elements in each strip from top to bottom are $F_{max}$ = 0, 0.0218, 0.0418 and 0.9465. The small box at the left indicates the aspect ratio (height to width) of the images (unity here). The original bounding box for the tissue at rest is indicated on each image.

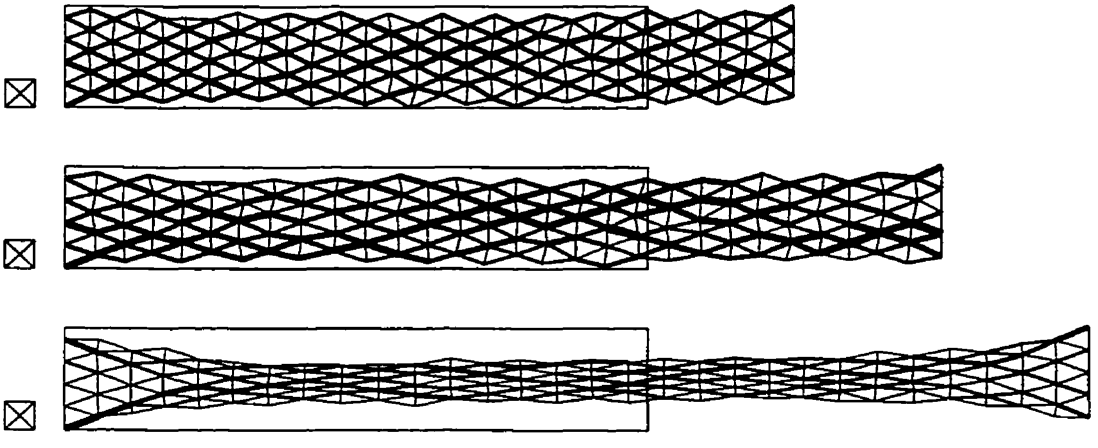

Figure 4-4. Simulated tissue with $l_k$ = 1.5 and Gaussian distributed stiffnesses with 50% standard deviation of the means, $k_1$ = 0.1 and $k_2$ = 10. Strains are 0.25, 0.5 and 0.75 with corresponding $F_{max}$ = 0.03266, 0.0653 and 1.073, top to bottom respectively. Force in each element is coarsely indicated by 4 levels of thickness.

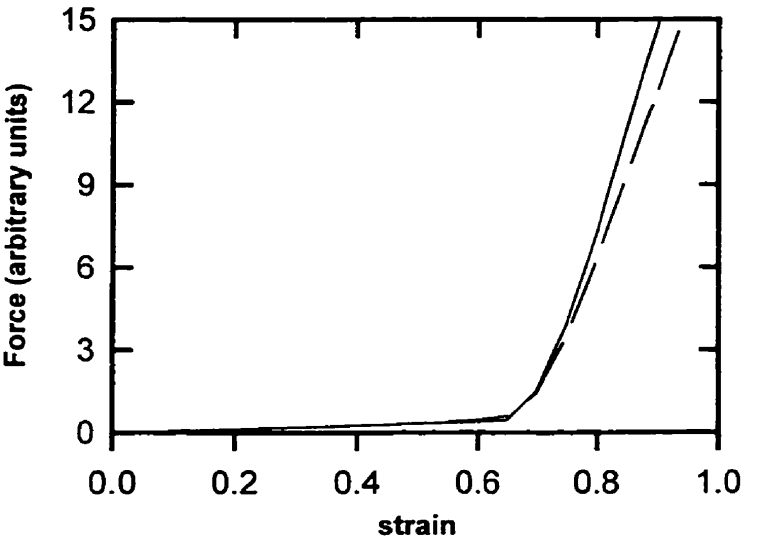


Figure 4-5. Force-strain curves of the tissues described in Figures 4-3 and 4-4. The solid line shows the results for the tissue with nondistributed stiffnesses, while the dashed line is for the tissue with Gaussian distributed stiffnesses.

Tissues in which the $l_k$ were distributed according to power laws posed severe difficulties in numerical simulation. This was primarily due to the fact that the distributions necessarily spanned several decades, and thus sampling the distributions adequately required a very large number of units. The largest simulations we attempted were 90x15 nodes. However, solution of some of these models required several days, particularly for high ratios of $k_2$ to $k_1$. Simulations of models having 60x10 nodes usually required less than a few hours, and this size of model was used most often. An example of six force-length curves for 60x10 node simulations with hyperbolically ($b$=1) distributed $l_k$ is shown in Figure 4-6. There is a large variation amongst the different realisations of the model due to the course sampling of the distribution for $l_k$ in each case. It was observed that this variation was less at other values of $b$ (Eq. 4-4) and was inversely related to the number of elements. In order to choose representative results for a given value of $b$ (Eq. 4-4), 6 different realisations of the distribution were simulated and either the 3rd or 4th curve in rank-order of force at strain 0.6 was chosen. The force-length curves were found to match the experimental data only when the $l_k$ were

distributed with $b$ very close to unity. Figure 4-7 shows force-strain curves from 60x10 node tissue strips with $k_1$ = 0.1, $k_2$ = 100 and $l_k$ distributed according to Eq. 4-4 with values for $b$ ranging from 0.9 to 1.1.

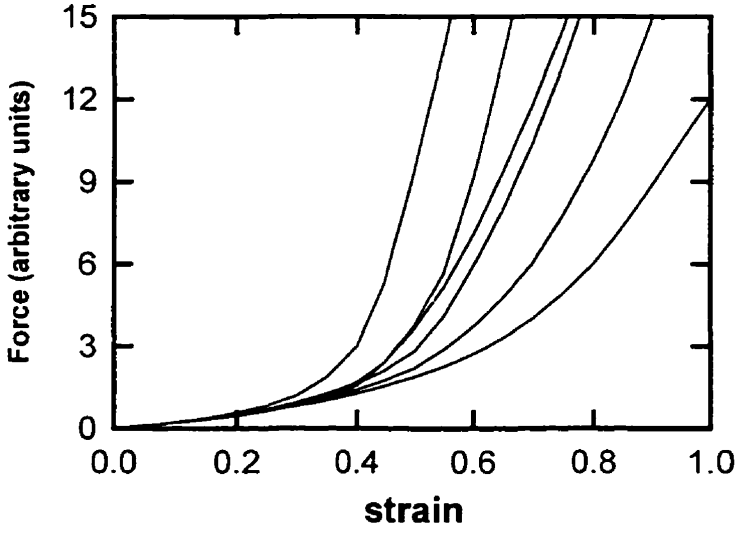


Figure 4-6. Force-strain curves from six realisations of simulated tissue (60x10 nodes) with hyperbolically ($b$=1) distributed $l_k$ with $k_1$ =0.1 and $k_2$ = 100.

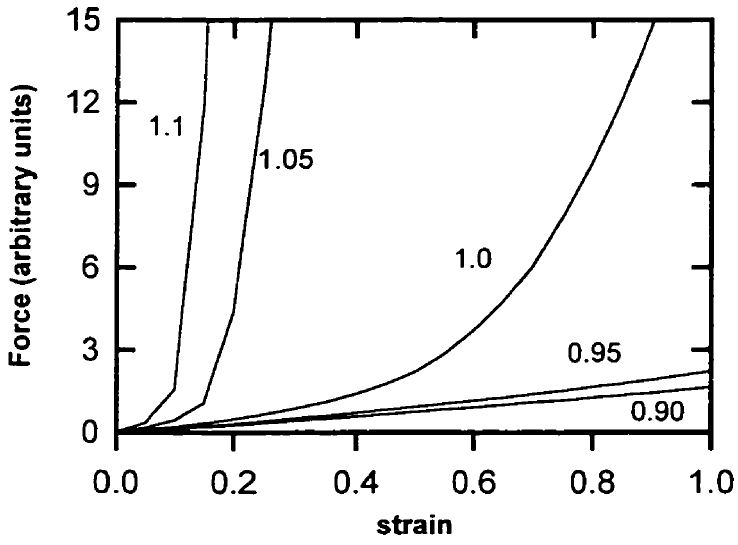


Figure 4-7. Force-strain curves from simulated tissues (60x10 nodes) with power-law distributed $l_k$ with the exponents $b$ indicated (Eq. 4-4).

The behaviour of the model when the $l_k$ are hyperbolically distributed and the spring constants are Gaussian distributed is shown in Figure 4-8. This agrees with the findings shown in Figure 4-4 and is the same result as in Chapter 3, Figure 3-9. In Chapter 3, the 1D model also showed this invariance in force-strain curves when the spring constants were chosen from Gaussian distributions, with stop lengths distributed according to a power law for ~99% of the data. This is despite the additional behaviour from the finite and random $k_2$ in this model. Thus, as in the 1D models of Chapter 2, the 2D distributed $l_k$ model is very robust to variability of the spring stiffnesses. However, the results of this simulation study are somewhat different to the analytic results and simulation of Chapter 3. In the 1D model, the force length curve was produced when the stop-lengths were distributed according to Eq. 4-4 with $b = 2$ for 99% of the data. In contrast, the 2D model gave realistic results for $b = 1$. It is likely that this difference is a geometrical effect. This may mean that in 3 dimensions, the exponent for the distribution may be altered again due to the increased range of motion, although this remains to be tested. One may speculate that if a model were constructed consisting of two 2D layers connected vertically at their nodes, these additional vertical elements would only alter the

equilibrium node positions from the 2D case slightly since the uniaxial loading implies that these members are not likely to be greatly extended. Thus the change in exponent of the $l_k$ distribution may be only slight. However, if the elements connecting the layers were oriented partially in the direction of the applied strain (e.g. by connecting nodes at 45 degree angles), then perhaps these elements would become a contributing factor to the stress-strain curve, and thus result in a greater change in the value for $b$.

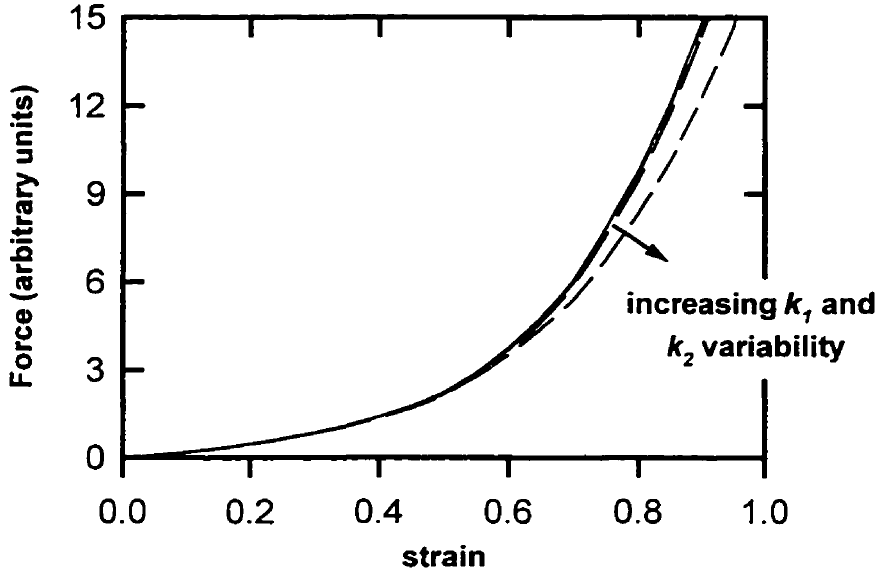


Figure 4-8. Force-strain curves from tissue simulations (60x10 nodes) with hyperbolically distributed $l_k$ (identical realisations) and Gaussian distributed spring constants. The spring constants mean values are $k_1$ = 0.1, $k_2$ = 100, and the standard deviations for both constants together are 0, 12.5, 25, and 50% of the means.

It is perhaps surprising that the force-strain curves should be so sensitive to the exponent of the $l_k$ distribution (Fig. 4-7). The sensitivity is due to the rate at which the elements exceed their respective $l_k$ as the tissue is stretched. This depends on both the $l_k$ distribution and the value of $k_1$. The value of $k_2$ is less important because as an element reaches its knee length, it is more likely to distort the nearby tissue rather than move up the steep portion of its length-tension curve, provided there are nearby elements which

have not yet reached their respective knee lengths. This kind of recruitment of nearest neighbours as the tissue becomes stressed can be observed in Figure 4-9, which shows a sequence of strains of a tissue strip with hyperbolically distributed $l_k$. When elements begin to exceed their $l_k$ (indicated by thick line elements in Fig. 4-9), they cause local tissue distortion which causes the stress to be inhomogeneously distributed throughout the tissue. Regions of increased stiffness appear to connect in small chains at first and then to form progressively longer chains. Finally, at the highest level of stress a continuous link of elements which have been stressed beyond their $l_k$ forms from end to end of the tissue. Thus, for the hyperbolic distribution of $l_k$, the elements become strained to their knee lengths in a gradual manner, which reflects the presumed way in which collagen fibres are recruited with increasing strain to produce a smoothly stiffening stress-strain curve.

It is possible, of course, that a different distribution of the $l_k$ and different $k_1$ and $k_2$ values could produce similar force-strain behaviour to the experimental data. However, no suitable candidates were found. Nevertheless, it is sufficient for our purposes that a parameter set was found that yielded the desired force-strain behaviour. It is for these reasons also that we did not investigate the behaviour of lung tissue models with power-law distributed spring constants. It was shown that distributing $l_k$ while keeping the spring constants fixed was equivalent to distributing the spring constants while keeping the stop-lengths fixed in Chapter 3. Therefore, similar results would be expected in the 2D case. Figure 4-10 shows a single tissue strip curve from Chapter 3 (Fig. 3-2) with the two closest realisations of 6 simulations with hyperbolically distributed $l_k$. The data match fairly well to about strain 0.6 for one of the realisations and to about strain 0.9 in the other.

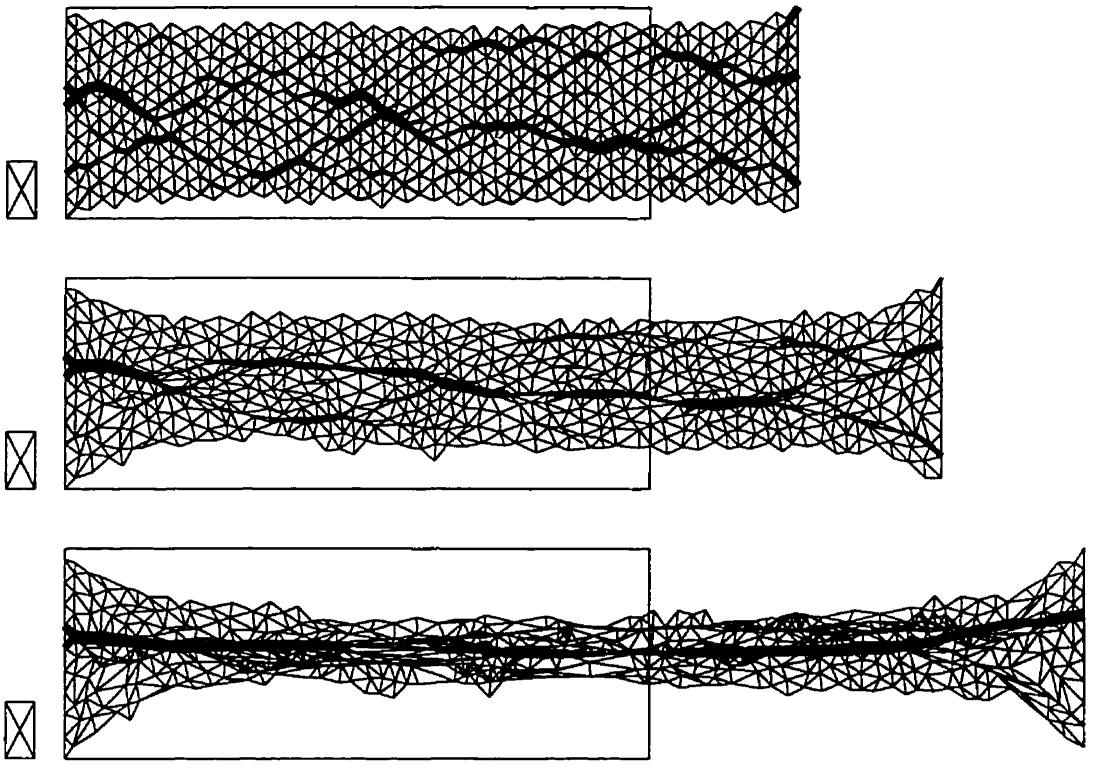

Figure 4-9. Simulated tissue (60x10 nodes, 1661 elements) with power-law distributed $l_k$ according to Eq. 4-4 with $b = 1$. Strains are 0.25, 0.5 and 0.75 with corresponding $F_{max}$ = 0.2006 and 1.141, 5.87 from top to bottom respectively. Force in each element is indicated by 8 levels of thickness. The box at left shows the images have been expanded vertically by a factor of 2.

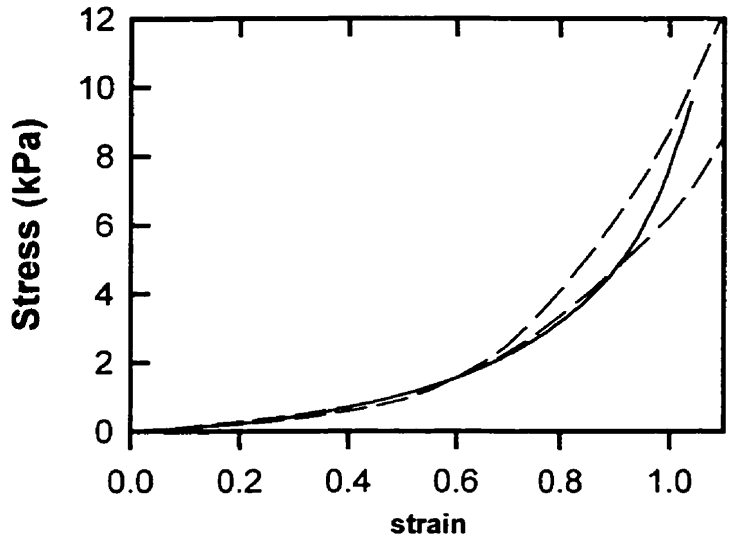


Figure 4-10. Tissue strip stress-strain curve from Figure 3-3 (solid), with the two closest realisations of 6 simulated curves normalised to match the tissue curve at 60% strain (dashed).

The change in shape of the tissue samples (Fig. 4-9) behaves similarly to the *in vitro* tissue strip described in Chapter 3. That is, the tissue narrows with extension, and most of the transition from fixed width at tissue ends to the narrower cross-section in the centre is confined to the tissue end regions. However, we cannot expect to match the geometric behaviour quantitatively, since this model is only 2-dimensional. Also, the model is composed of statically determinate structures (triangular spaces). Although statically determinate models can predict the bulk properties of the air-filled lung (144), it has been shown that the resistance to shear is better reproduced using statically indeterminate structures, such as the dodecahedron shape in 3 dimensions (15,72). This is presumably because indeterminate structures, when not prestressed, have very little resistance to shear deformations, since their members can rotate to a new configuration with little stress of the elements. With prestress, the resistance to shear is increased. For the statically determinant structure, on the other hand, resistance to shear arises from both prestress and element loading. Real tissue likely has substructures of both indeterminate and determinate nature. The criss-crossing network of fibres across alveolar walls may

behave more as a determinate structure while the geometric arrangement of the alveolar walls themselves is indeterminate.

The tissues of Figure 4-9 are quite distorted at the higher levels of strain, and some of the nodes have even crossed over neighbouring units. This is a kind of buckling that could not occur in 3-dimensions, at least at the scale of the alveolar wall, since this would mean that the walls would have to pass through each other. This may explain some of the lack of agreement between the true data and the simulated data at high strains shown in Figure 4-10. The true tissue strip stress-strain curve becomes stiffer than the simulated curves at high strain, perhaps due to these additional physical restrictions. The degree of distortion shown in Figure 4-9 is not normally observed experimentally in fixed samples of lung tissue (116,169). However, most tissue images are from samples fixed at a defined level of transpulmonary pressure, and thus do not show how tissue behaves under nonuniform loading. To my knowledge, no study has imaged the microstructure of the lung tissue subjected to uniaxial strains. Large degrees of distortion have been observed in nearly 2-dimensional flat sections of tissue which have been exposed to smooth muscle agonists (29,112). The contractile agonist caused smooth muscle cells within the alveolar walls and around airways to constrict producing a large degree of heterogeneity within the tissue. However, it is uncertain whether this heterogeneity is attributable to differences in smooth muscle cell response, differences in the smooth muscle distribution or due to passive mechanical inhomogeneity (or a combination of each process). In any case, evidence for inhomogeneity in the passive mechanics of the lung tissue has been observed by Wilson et al. (176), who showed that the regional $PV$ curves measured using parenchymal markers followed markedly disparate paths during passive expiration from total capacity. Indeed, this could conceivably arise from different samplings of the underlying distributions of the constituent properties as observed in Figure 4-6, as Wilson et al. remarked (176).

## 4.4 Conclusions

In this chapter, I have expanded the ideas developed in Chapter 3 in a 2-dimensional model of lung parenchyma with distributed constituent properties. The actions of the elastin and collagen fibres were simplified to a string-spring pair in which the elastin first extended as a weak spring until the collagen fibre became taut (at its knee length), at which point the pair acted like a stiff spring. Curves which were very close to measured stress-strain data were generated for models in which the knee-lengths followed a hyperbolic distribution. This was different than the $1/l^2$ distributions found in Chapter 3. This difference is likely due to geometric effects appearing in the 2D models. The elastic behaviour of the model was very sensitive to the value of $b$ in the $1/l_k^{\,b}$ distribution. Also, a large amount of variability was observed between different realisations of hyperbolic distributions. Finally, the model illustrated the development of geometric heterogeneity in the tissue micro-structure with increasing strain. This is due to the $1/f$ distribution of the fibre properties leading to fractal-like spatial recruitment of collagen fibres under uniaxial loading.

# 5. A model for the quasi-static *PV* curve of the lung

## 5.1 Introduction

The amounts of collagen and elastin and their spatial arrangements in the lung are altered in diseases such as pulmonary emphysema and fibrosis (167,178), and it is thought that these alterations could be responsible for the abnormal *PV* curves associated with these diseases (127). However, it is currently unclear how to precisely translate alterations in lung tissue constituents into changes in tissue mechanical properties. In Chapter 3, I developed a model of lung tissue that exploits the collagen fibre recruitment concept by representing the collagen and elastin fibres as a series of spring-string pairs. In this chapter, I explore how the model might be used to explain the curvilinear quasi-static *PV* curve of whole lung, and how the changes in the *PV* curve due to disease are reflected in the model.

## 5.2 Methods

In analogy to the tissue model developed in chapter 3, I consider the lung as a series of elastic volume elements (elastance $E$), each of which extends to a maximum stop volume ($v$). In doing so I presume that the nature of the tissue expansion in 3-dimensions is like that in tissue strips. That is, elastin fibres stretch elastically under the applied load whether uniaxially or from lung inflation while collagen fibres straighten until taut. Thus, in no way does a stop volume unit correspond to a well-defined physical structure such as an alveolus. It merely represents the action of collagen fibres straightening within the lung tissue in terms of volume units. Indeed, Mercer and Crapo (102) showed via serial reconstruction that the pressure volume characteristics of alveoli are much the same as for

the whole lung. With the model we explore how the mechanism of mechanical stops in parallel with elastic springs can describe the deflation limb of $PV$ curves, and how changes in $PV$ curves in disease are reflected in changes in the model constituents, the elastin and collagen fibre matrices. In particular, I examine how changes in static deflation $PV$ curves may be related to changes in the underlying tissue structure with tissue diseases such as emphysema and fibrosis.

We can generate static elastic $PV$ curves by having both stop volumes and unit elastances distributed according to Eqs. 3-7 and 3-14, with $F$, $L$, $k$ and $l$ substituted for $P$, $V$, $E$ and $v$ respectively, where $V$ is lung volume and $P$ is transpulmonary pressure. The equation most commonly used for the static $PV$ curve is that first introduced by Salazar and Knowles (132), reproduced here from Chapter 2 (Eq. 2-1):

$$V = A - B\exp(-KP), \tag{5-1}$$

where $A$, $B$ and $K$ are constants. If we solve for the model distributions by double differentiation of Eq. 5-1 in the $PV$ equivalent of Eqs. 3-7 and 3-14, we have

$$N(v) = \frac{KEB}{\varphi}\exp(-v/\varphi), \tag{5-2}$$

where

$$\varphi = \frac{1}{KE} \tag{5-3}$$

and

$$M(E) = \frac{KEB}{\gamma}\exp(-E/\gamma), \tag{5-4}$$

where

$$\gamma = \frac{1}{Kv} \tag{5-5}$$

and we have used the fact that

$$P = Ev \tag{5-6}$$

in analogy with Eq. 3-12. It can also be shown, since the areas under the distributions of Eq. 5-2 and 5-4 are fixed and finite, that $B$ is proportional to $v$ in the stop volume distribution model, and is proportional to $\gamma$ in the distributed elastance model. Since the actual values of $E$ or $v$ are arbitrary, I use the convention adopted in Chapter 3, and thus fix the area under each distribution to be 10 000. Thus the model cannot be used to predict the magnitudes of the parameters of the models, but only changes in their value from some reference, which for the purposes of this chapter will be the parameters derived from the normal $PV$ curve.

Equations 5-2 and 5-3 represent the stop volume distribution model while Eqs. 5-4 and 5-5 represent a distribution of elastances. It is likely that the collagen fibre matrix and the elastic constitutive elements of lung tissue have distributed stop volume and stiffness properties, respectively. We therefore recognise that the two models represent the extremes of possibility, and so consider these two extremes in order to quantitatively assess how changes in $PV$ curves may reflect pathologic changes in lung tissue.

## 5.3 Results and discussion

We can apply these two extremes to examine the effects of changes in the model parameters. I first consider the effect of decreasing the elastance by 50%. For the $N(v)$ model, this means a decrease in the value of $E$ by 50%, or using the $M(E)$ model, we shift the distribution leftward by halving each elastance. In either case, the change in the $PV$ curve is a leftward shift, resulting in a doubling in the value of $K$, with no change in $B$ or $A$ (Figure 5-1). This is in agreement with the current hypothesis that changes in $K$ associated with emphysema are due to changes in the elastin network. However, emphysema is also associated with increased lung volume, which in my model can only be caused by changes in the collagen network. I thus conduct the alternate experiment and cause the stop volume distribution to be altered by increasing $v$ by 50 % in either the $N(v)$ model or $M(E)$ model and maintaining the same zero pressure intercept. Again the results are the same for either model and are shown in the left panel of Figure 5-2. The $PV$ curve begins with the same slope at low lung volumes, but as the volume increases the slope

decreases more slowly and the asymptotic volume maximum increases. In this case, $K$ is decreased to 66% of normal, while $B$ is increased to 150% of normal. Note that, while $E$ and $\gamma$ have units of elastance and thus affect the rate of change of pressure within the vital capacity (Fig 5-1), $\varphi$ and $v$ have units of volume (and are in fact proportional to $B$), and thus control the vital capacity of the model (Fig 5-2).

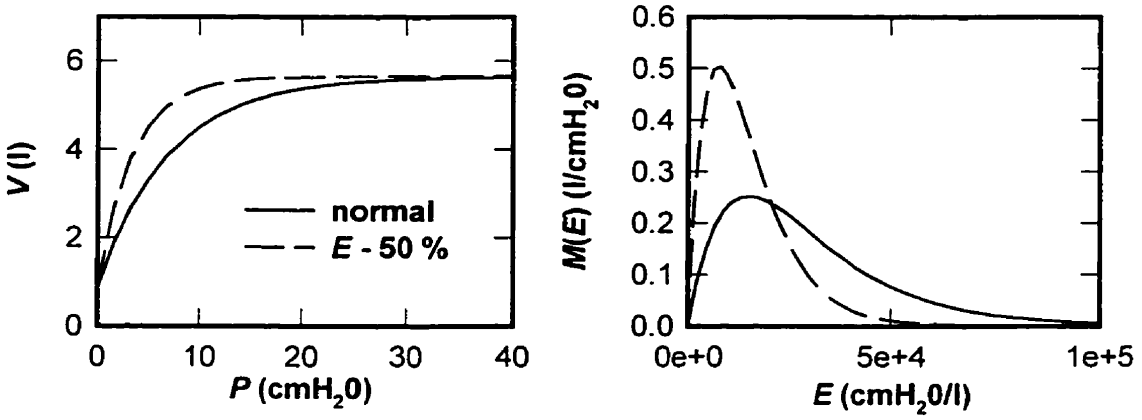


Figure 5-1. Left panel: $PV$ curve of normal lung (solid) with curve from model in which $E$ had been decreased by 50% (dashed). Right panel: elastance distribution of model applied to normal $PV$ curve (solid) and with $E$ decreased by 50% (dashed).

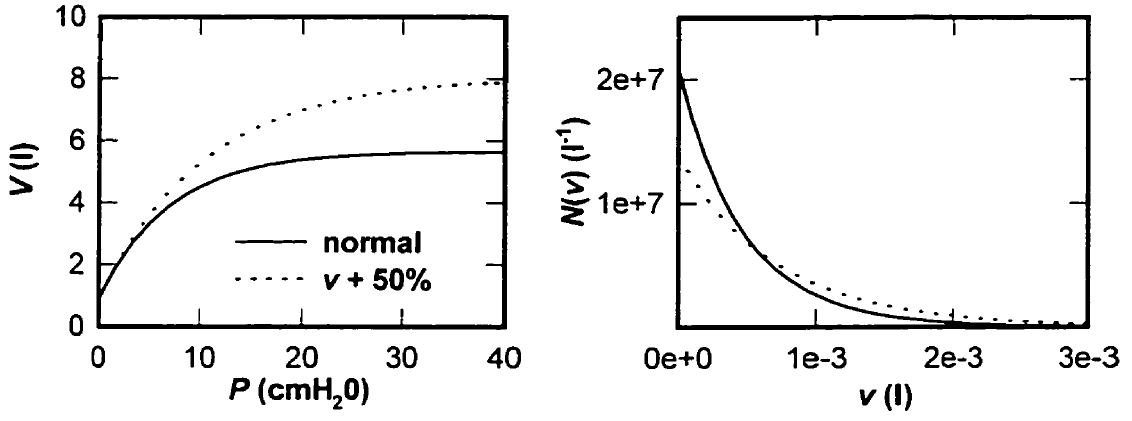


Figure 5-2. Effects of increasing $v$ by 50% from normal values. Left panel: $PV$ curve of normal lung (solid) with curve from model in which $v$ had been increased (dotted). Right panel: $N(v)$ distribution of model applied to normal $PV$ curve (solid) with $N(v)$ distribution where $v$ has been increased (dotted).

| | $A$ (l) | $B$ (l) | $K$ ($cmH_2O^{-1}$) |
|---|---|---|---|
| normal | 5.65 | 4.79 | 0.143 |
| emphysema | 7.66 | 6.98 | 0.325 |
| fibrosis | 2.64 | 0.93 | 0.089 |

Table 5-1. Parameter values from the fit of Eq. 5-1 to the deflation limb of PV curves of a normal, emphysematous and fibrotic lung in vivo from Gibson et al. (45).

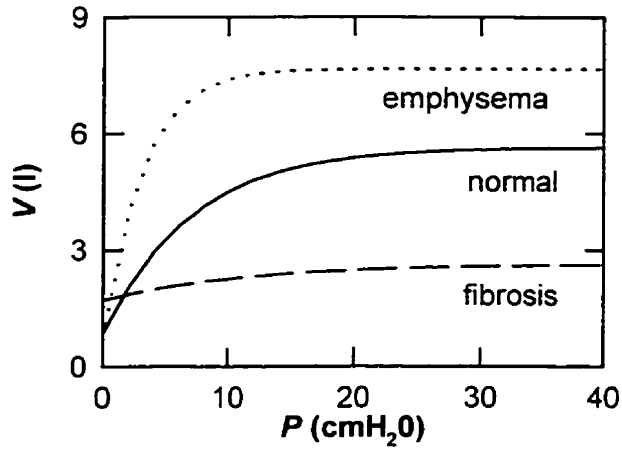


Figure 5-3. *PV* curves of representative emphysematous, normal and fibrotic lungs reproduced according to Eq. 5-1 using the parameters from Table 5-1.

To investigate how the parameters of the model are changed from normal when applied to representative examples of lung tissue disease, I applied the model equations (Eqs. 5-2 to 5-5) to the curves shown in Figure 5-3. The changes of the model parameters expressed as a percentage of normal are shown in Table 5-2. For emphysema, $\varphi$ and $v$ are elevated while $E$ and $\gamma$ are decreased below normal. In terms of the stop volume distribution model, $N(v)$ for an emphysematous lung is thus shifted toward large stop volumes compared to normal (Fig. 5-4), and $E$ is decreased to 30% of normal. This is consistent with the nature of the disease, which causes destruction of tissue with associated remodelling of both elastin and collagen networks as well as an increase in airspace volumes (48,178). If interpreted in terms of the elastance distribution (Fig. 5-4, right panel) the $M(E)$ shifts leftward of normal indicating a loss in tissue stiffness, and $v$ increases to 146% of normal. Both models predict changes in qualitative agreement with observation. Of course, both elastance and stop-volumes are likely to be distributed, so the actual changes in distributions are likely to lie between the limits expressed in Figure 5-4.

By contrast, the changes in the tissue afflicted by fibrosis involve widespread inflammation, an increase in the concentration of interstitial fibre constituents, and airspaces are reduced or even filled in with inflammatory products (33). Correspondingly

for fibrosis, in terms of each model, the parameters φ and $v$ are greatly decreased below normal while $E$ and γ are elevated, which results in a reduction in vital capacity and a stiffening of the tissue (Table 5-2). The changes according to the distributions of each model are indicated in Figure 5-5. $N(v)$ is shifted towards smaller stop volumes corresponding to the reduction in vital capacity, while $M(E)$ is shifted to greater tissue stiffness in agreement with increased amounts of connective tissue associated with the disease.

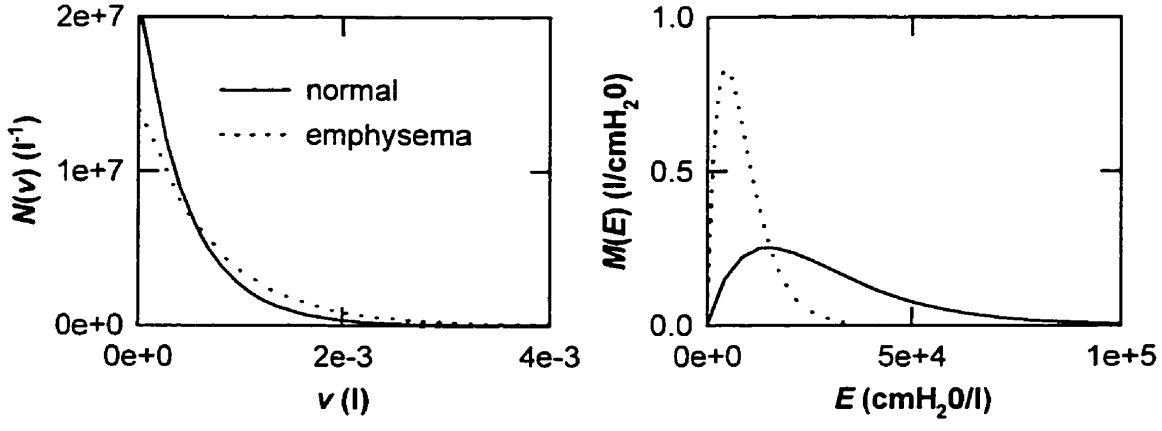


Figure 5-4. Stop volume distributions (left panel) according to application of Eqs. 5-2 and 5-3 and elastance distributions (right panel) according to application of Eqs. 5-4 and 5-5 to representative $PV$ curves of normal and emphysematous lungs (Fig. 5-3).

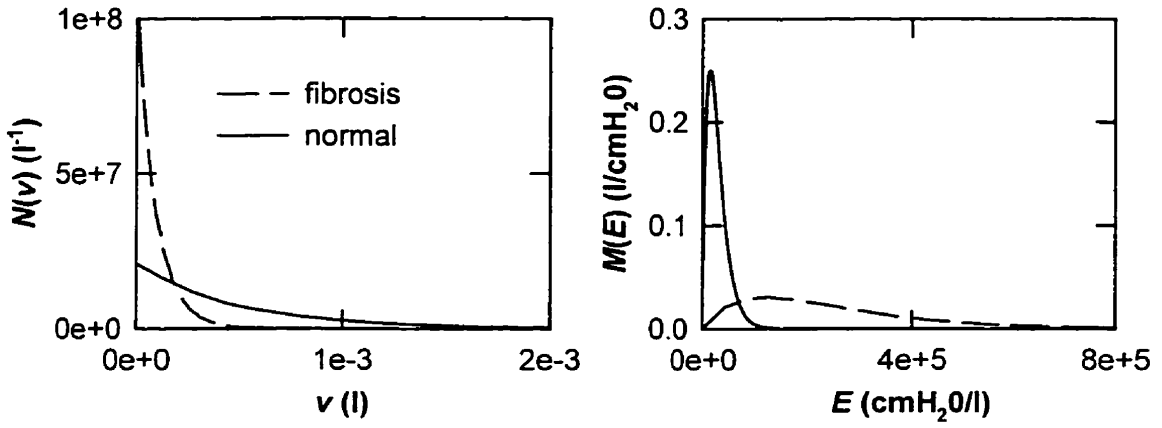


Figure 5-5. Stop volume distributions (left panel) according to application of Eqs. 5-2 and 5-3 and elastance distributions (right panel) according to application of Eqs. 5-4 and 5-5 to representative *PV* curves of normal and fibrotic lungs (Fig. 5-3).

| | distributed stop volumes | | distributed elastances | |
|---|---|---|---|---|
| parameter | E | φ | γ | *v* |
| emphysema | 30 % | 146 % | 30% | 146% |
| fibrosis | 827 % | 19 % | 827% | 19% |

Table 5-2. Percent changes in model parameters from normal values to those for emphysema and fibrosis for the distributed stop volume and distributed elastance models.

In both emphysema and fibrosis, the changes in the model parameters were always greatest for those parameters associated with elastance, $E$ and $\gamma$. A possible mechanism for the dominance of changes in elastance-related properties over changes in volume-related properties via our model is shown in Figure 5-6. Here I consider the collagen and elastin fibres to be composed of the parallel contribution of multiple fibrils.

The stiffness of a single unit is equal to the sum of the stiffnesses of all the individual elastin fibrils in that unit, whereas the stop length of the unit is the minimum collagen fibril length. A decrease in the number of elastin fibrils would manifest itself as a proportional decrease in the stiffness of the unit, while an increase in stop length would occur only if the shortest fibril were removed. The situation is similar for the addition of collagen or elastin fibrils; the elastance increases in proportion to the number of added elastin fibrils, while the stop length shortens only if a collagen fibril shorter than the shortest is added. The elastance-associated parameters are thus more likely to be affected than volume-associated parameters under conditions that randomly affect both collagen and elastin, through tissue destruction (emphysema) or tissue building (fibrosis). Possible support for the model of Figure 5-6 was demonstrated by Mercer and Crapo (103) who observed parallel collagen fibrils meandering in a wavelike fashion in serial reconstructions from slices of human and rat lungs. They measured the maximum possible degree of fibre extension to be as much as 16.1 ± 3.2% (SE, n=6) near the alveolar septal edge in human lungs. This is comparable in magnitude to the changes expected to occur between functional residual capacity and total lung capacity (102).

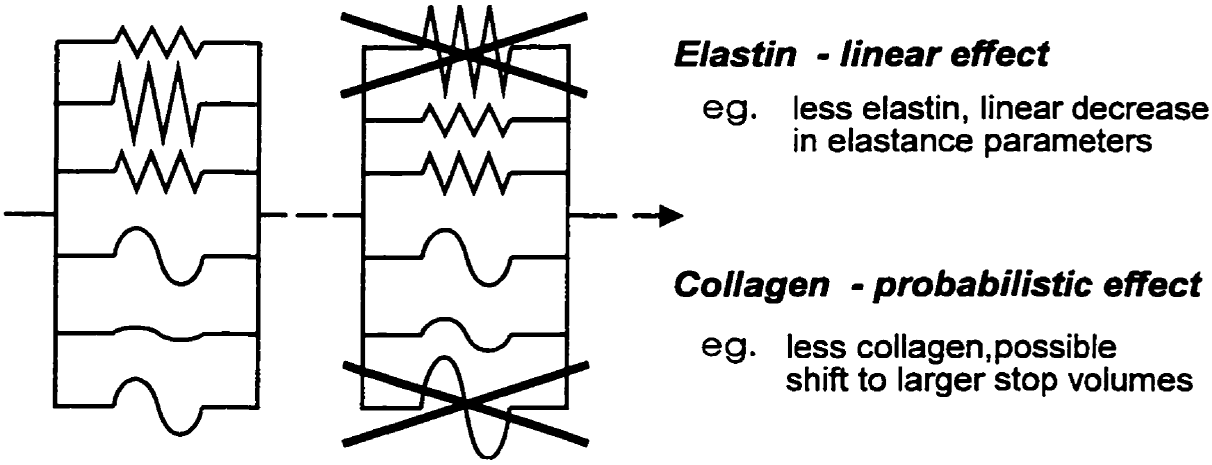


Figure 5-6. Generalisation of spring and string model of Fig. 3-1, showing the different effects of removing collagen or elastin fibres.

The shapes of *PV* or length-tension curves can be altered by digestion of tissue constituents by proteases (70,75,134). Karlinsky et al. (70) found that the chord

compliance was increased in isolated hamster lungs exposed to elastase, but no change in vital capacity occurred. By contrast, collagenase caused an increase in vital capacity and a change in the shape of the *PV* curve. These observations are consistent with our model. However, as mentioned in Chapter 2.1.4, when the measurements were done *in vivo* by the same authors there was an increase in vital capacity observed in the lungs 21 days after elastase treatment (75). This contradicts the theory that the collagen matrix is responsible for limiting the maximum extension. They attributed the difference between the *in vitro* and *in vivo* results to the repair process after elastase injury which may disrupt the collagen matrix. Sata et al. (134) found that the stress-strain curves of microtissue specimens from hamster parenchyma could be described by 2 exponential functions, where the exponent of the first exponential was primarily responsible for the low strain portion of the curve while the upper portion of the curve was due to the exponent of the second exponential. They found that elastase treatment affected only the first exponent, while collagenase affected only the second exponent, which is in agreement with our model. However, from their data one can discern an increase in the asymptotic maximum extension in both elastase and collagenase treated strips. The increase in maximum extension with collagen injury is in agreement with our models (of this chapter and of Chapter 3); however, increases in maximum extension with elastase treatment is not predicted. A possible reason for the increased extension with elastase is that they may have induced irreversible damage to their tissue by stretching the specimens in their study to strains outside that which is physiologically possible (>1.6 control, greater for treated tissue) or it may be that in three dimensions, disruption of the elastin network alters the spatial arrangement of the collagen fibres, thus permitting increased extension.

A significant result of the application of the model to the *PV* curves of diseased lungs is that it may provide a mechanistic description for the origin of the shape parameter $K$ (Eq. 5-1) in terms of the structural constituents of lung tissue and their organisation. The parameter $K$ has been found to be increased in those patients with emphysema (48,120) and to be decreased in fibrosing alveolitis (163) as shown in Table 5-1. Within the context of our model, these changes in $K$ are interpreted in terms of alterations to the collagen and elastin networks (Table 5-2, Figs. 5-4, 5-5). In fact $K$ is

inversely proportional to the stiffness arising from the elastin related parameters $E$ and $\gamma$ and inversely proportional to $v$ and $\tau$ which define the maximum lung vital capacity through the distension of collagen. I have not been able to find any other quantitative model which addresses how changes in tissue constituents affects the shape of the $PV$ curve.

I did not explicitly include the effects of surface tension in the model, and it may be that changes in surface tension in emphysema and fibrosis may contribute to changes in $K$. Surface tension contributes a significant portion to the elastic recoil of the lung as clearly shown by the differences between $PV$ curves for saline- and air-filled lungs (140,148). Furthermore, Haber et al. (49) found that $L_m$ correlated well with $K$ in air-filled lungs but was unrelated to $K$ from saline-filled lungs, suggesting that changes in airspace size were related to surface tension effects rather than tissue properties. However, we note as per the analysis of Hoppin and Hildebrandt (60) that surface tension properties are mechanically coupled. Removal of surface tension forces (e.g. by saline filling) alters alveolar wall geometry, changing tissue distension and thus affecting the recoil attributable to the tissues.

In any case, I do not claim that my model accounts for all aspects of the lung $PV$ curve, but merely that it embodies the important contribution from the tissues themselves whose significance for lung recoil is well accepted. Indeed, as mentioned in the previous chapter, Wilson et al. (176) invoked this mechanism to explain the regional mechanical heterogeneity they observed during expirations from total lung capacity in dogs using parenchymal markers. Such regional variation is predicted by my model as different lung regions would have different samplings of the underlying collagen and elastin fibre distributions and thus would follow different local $PV$ curves.

## 5.4 Summary

In this chapter, the model of Chapter 3 is extended to account for the $PV$ curve of the whole lung *in vivo*. Important structure-to-function links were made which contrast

the roles of collagen and elastin in the tissue diseases of emphysema and fibrosis. The predicted changes in the tissue constituent properties, such as changes in airspace size and tissue elasticity in these diseases, are matched by the changes in the model parameters. Changes in the elastin properties dominated the changes in the collagen properties in these diseases. A mechanism by which this is likely to occur in general tissue disease which affects both fibre networks is proposed. Changes in the tissue distension from alterations in the collagen fibre network fibres might occur probabilistically while changes in the elastic recoil due to elastin may occur in proportion to the change. Although it is likely that $K$ from the Salazar and Knowles equation (Eq. 5-1) may have both surface tension and tissue origins, this model provides a possible mechanistic link between $K$ and both the collagen and elastin tissue properties, and between $B$ and distension of the collagen network.

# 6. Nonlinear block structured modelling of lung tissue mechanics *in vitro*

## 6.1 Introduction

As well as elastic behaviour, lung tissue displays significant time dependent behaviour. This can be demonstrated by the finite area of length-tension loops (38,149) due to the dissipation of energy either viscoelastically and/or plastoelastically (58). Also, the dynamic mechanical impedance of the lung exhibits amplitude and volume dependencies (7,26,156) which have been ascribed to both nonlinear viscoelasticity (114,155) and plastoelasticity or viscoplasticity (58,144,145). With Dr. Daniel Navajas, I measured the mechanics of lung tissue using sinusoidal oscillations and step perturbations at 3 different amplitudes at a single operating stress and 3 stress-operating points at a single amplitude (114). The measurements were made on the apparatus I constructed in partial fulfilment of my M.Eng. degree. We also applied oscillations at 5 different frequencies at a single amplitude and operating stress. We analysed the data in terms of the quasilinear viscoelastic model of Navajas et al. (115) that had been previously applied to rat diaphragm muscle strips (see Introduction, Section 2.3.3).

The model is based on Fung's quasilinear viscoelastic theory (40), and is a Hammerstein model with only 2 parameters. The equations of the model are found in Introduction, Section 2.3.3. The model predicts oscillatory behaviour according to

$$E = \sigma_o[\sinh(\alpha\Delta\lambda)/\Delta\lambda](1 + 0.25\gamma + \gamma\log(2\pi f)) \qquad (6\text{-}1)$$

and

$$R = \sigma_o[\sinh(\alpha\Delta\lambda)/\Delta\lambda]\gamma/(9.2f), \qquad (6\text{-}2)$$

where the parameters of the equations can be found in Chapter 2.3.3. We fitted the model (Eqs. 2-14 and 2-15) to the stress adaptation data and predicted the response to oscillatory input. The predicted frequency and operating point dependencies of $R$ and $E$ matched measured oscillatory data. However, the data indicated no dependence of $E$ on input amplitude and a slight negative dependence of $R$ on amplitude, whereas the model predicted a slight positive $R$ and $E$ amplitude dependence. $R$ was also consistently underestimated by about one third, indicating additional dissipation within the lung tissue not accounted for by the model. Following the approach of Hildebrandt (58), we postulated that this additional dissipation may arise from plasticity which could not be accounted for by the model (114). However, it is also possible that the model did not have enough degrees of freedom to describe the data, since it contained only two parameters, $\alpha$ and $\gamma$. In this chapter, I thus explore the possibility that the lung tissue may be described by nonparametric block structured models of the Wiener or Hammerstein forms. I also propose a new parallel block structured model and test its performance for the description of lung tissue mechanics.

## 6.2 Methods

Five tissue strips were taken each from a different dog from the lower subpleural region of the right lung. The lung tissue strips were prepared exactly as in Chapter 3.2.2 and the characteristics of the strips are shown in Table 6-1. Three different maneuvers were performed on the tissue strips; preconditioning, sinusoidal cycling and pseudo-random perturbations, each described below. All perturbation sequences were conducted with the strips in air by lowering the fluid level of the bath to eliminate the effects of the very significant noise produced due to fluid motion on the transducer for the perturbations used in this chapter. The tissue did not show any signs of drying during the ~ 84 second intervals ( see timing protocol below) that it was held in the air.

| tissue strip | 6 | 7 | 8 | 9 | 10 | mean | std. dev. |
|---|---|---|---|---|---|---|---|
| $A_r$ (cm$^2$) | 0.3357 | 0.3202 | 0.2888 | 0.2982 | 0.3702 | 0.3226 | 0.0323 |
| $L_r$ (cm) | 2.90 | 2.73 | 2.95 | 3.01 | 2.96 | 2.91 | 0.107 |

Table 6-1. The dimensions of the dog lung tissue strips, where $A_r$ is the tissue strip cross-sectional area calculated as in Chapter 3.2.2 at resting length $L_r$.

The tissue was preconditioned at 2% $L_r$/sec between $L_r$ and a maximum stress of 5 kPa for a total of 4 cycles. On the 4th cycle, strain stopped when the desired stress level was reached (either 0.5, 1.0 or 1.5 kPa). After approximately 60 seconds, sinusoids equalling or exceeding the amplitude of the subsequent pseudo-random perturbation were applied, provided the stress level did not exceed 5 kPa. After approximately 60 further seconds, the fluid level of the bath was lowered below the level of the tissue, and after a another 60 seconds, a pseudo-random perturbation sequence was recorded. The output level of the transducer was slightly sensitive to temperature (94); thus the measurements in air had to be corrected for the change in output. This was done in post-processing by adjusting the initial level of the recorded force signal to equal the initial force recorded during the sinusoidal oscillations in the bath. This involved an adjustment of about ~2 g, which was much less than the range of the recorded perturbations. The fluid level of the bath was returned to normal after the perturbation was complete, and after 60 seconds a sinusoidal perturbation of 0.125 Hz of amplitude equalling or exceeding the amplitude of the pseudo-random perturbation was applied. Signals were anti-aliased filtered to 50 Hz (6-pole Bessel), and sampled at 256 Hz on a 486 PC using a 12-bit A/D converter with custom software.

### 6.2.1 Perturbation signals

The input volume perturbation was a pseudo-random noise signal of rectangular amplitude probability distribution and $1/f$ ($f$ is frequency) amplitude distribution between 0.125 and 12.5 Hz and zero elsewhere. It was generated using an algorithm similar to that

of Hunter and Kearney (61). The integers from 1 to 256 were randomised to generate 8 sec of 32 Hz white noise. Pairs of values in the signal were then swapped at random. If the spectrum of the signal after each swap was closer to the desired spectrum (in the least-squared sense) the swap was accepted. This process was continued until no further improvement occurred (approximately $8x10^5$ swaps). This process differs from that of Hunter and Kearney (61) in that signal spectra calculated by Fast Fourier transform are compared rather than signal auto-correlation functions. Use of the biased estimate for the auto-correlation function led to systematic errors in the frequency spectrum due to the long memory of the desired auto-correlation function. This error did not arise by direct use of the signal spectra, and led to signals which were naturally periodic. After convergence, the resulting signal was then interpolated to a sampling rate of 256 Hz by zero-padding the Fourier transform and taking the inverse Fourier transform. The signal was also filtered in the Fourier domain to exactly the desired frequency spectrum. This produced a cyclic signal with an amplitude histogram that was flat to within 1% (in the root mean squared sense) and a frequency spectrum that was exactly $1/f$ (Fig. 6-1). The signal was concatenated with itself 3 times to produce the final 24 second volume perturbation sequence. Three scaled versions of the signal having peak-to-peak strain excursions of 0.25, 0.50 and 0.75 were produced. The strain velocity spectrum was thus approximately flat between 0 and 12.5 Hz, with root mean squared velocity levels of 0.125, 0.25 and 0.375 $sec^{-1}$. Four different versions of the signal were used to reduce any time dependent effects: the original signal, the signal in reverse order, the inverted signal, and the inverted signal in reverse order. A different version was randomly assigned to the different stress levels and strain amplitudes of investigation. Perturbations were started at a point mid-way in the range of the strain excursions, and at stress levels of 0.5, 1.0 and 1.5 kPa. Perturbations were only conducted at stress levels for which the minimum and maximums of the perturbation sequence did not exceed the limits of 0 to 5 kPa. The order of operating stress levels was randomised and at each operating stress level, the order of input strain amplitudes was randomised.

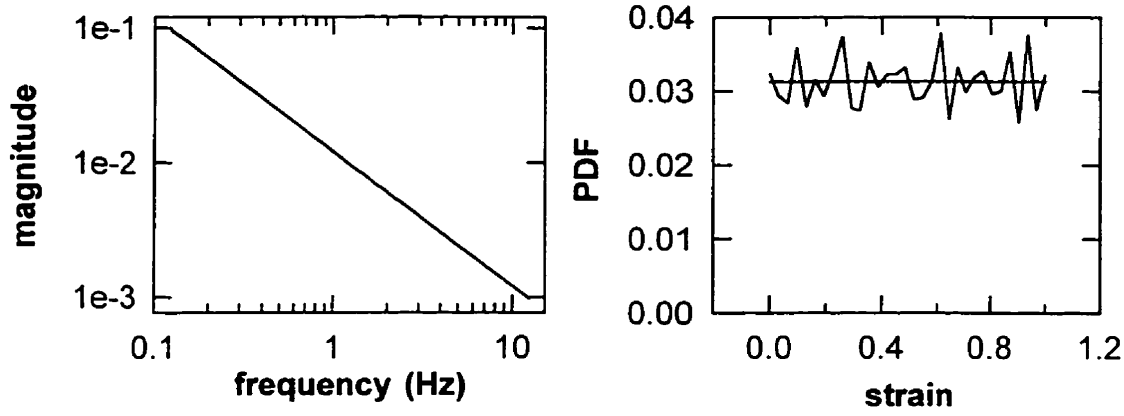


Figure 6-1. Left panel: frequency spectrum of input signal. Right panel: probability density function (PDF) of input signal (jagged line), where the straight line indicates the ideal rectangular PDF. For each tissue strip, the amplitude range was scaled to peak-to-peak excursions of 0.25, 0.5 and 0.75 strain, and mean strain levels were adjusted to produce stress levels of 0.50, 1.0 and 1.5 kPa.

### 6.2.2 System identification - Wiener and Hammerstein models.

The identification method used was that of Hunter and Korenberg (63) described in Chapter 2.3.2. The system input was the strain signal $\varepsilon(t)$ and the system output was the stress $\sigma(t)$. Polynomials of order 2 to 10 were estimated, and impulse response functions were one-sided of 1 second duration. The iterative identification was terminated when improvement in the VAF% between $\sigma(t)$ and the model output was less than $10^{-6}$. Unless otherwise indicated, the linear system block dc gain was fixed to unity, so that all static gain was located in the nonlinearity.

In order to interpret the results in a manner consistent with current methods in the study of respiratory mechanics, we transform the impulse response functions, $h(t)$, of the dynamic linear blocks to the frequency domain as

$$H(f) = \Im(h(t)), \tag{6-3}$$

where the script '$\Im$' indicates the operation of Fourier transformation and $H(f)$ is the transfer function of the system. It is common in the field of respiratory mechanics to define impedances as the complex frequency domain ratio between pressure and flow. The analogous representation in the case of the tissue strip is the frequency domain ratio between stress and the time derivative of strain. We choose the same convention to represent the impedance of the dynamic linear blocks, thus

$$\begin{aligned} Z(f) &= \sigma(f) / \dot{\varepsilon}(f) \\ &= R(f) - i\,E(f)/2\pi f \end{aligned} \quad , \tag{6-4}$$

where $\sigma(f)$ and $\dot{\varepsilon}(f)$ are the Fourier transforms of $\sigma(t)$ and $\dot{\varepsilon}(t)$, respectively, $R(f)$ is called resistance and is that part of the impedance in phase with $\dot{\varepsilon}(f)$, $E(f)$ is that part of the impedance in phase with the strain, $\varepsilon(f)$, and $i$ is positive square root of -1. To calculate $Z(f)$ from $H(f)$ we have

$$Z(f) = \frac{-iH(f)}{2\pi f} \quad . \tag{6-5}$$

## 6.3 Results and discussion

Figure 6-2 shows sample input $\varepsilon(t)$ and output $\sigma(t)$ signals for a single tissue strip at an operating stress of 1.0 kPa and strain peak-to-peak amplitude of 0.5. It can be seen from the increased stress response at high strains that the relation between the input and output is highly nonlinear. Figure 6-3 shows examples of Wiener models identified from a single strip for perturbations at 3 different operating stresses. It can be seen that the impulse response functions have large values at zero lag, and then quickly decrease toward zero in an oscillatory manner.

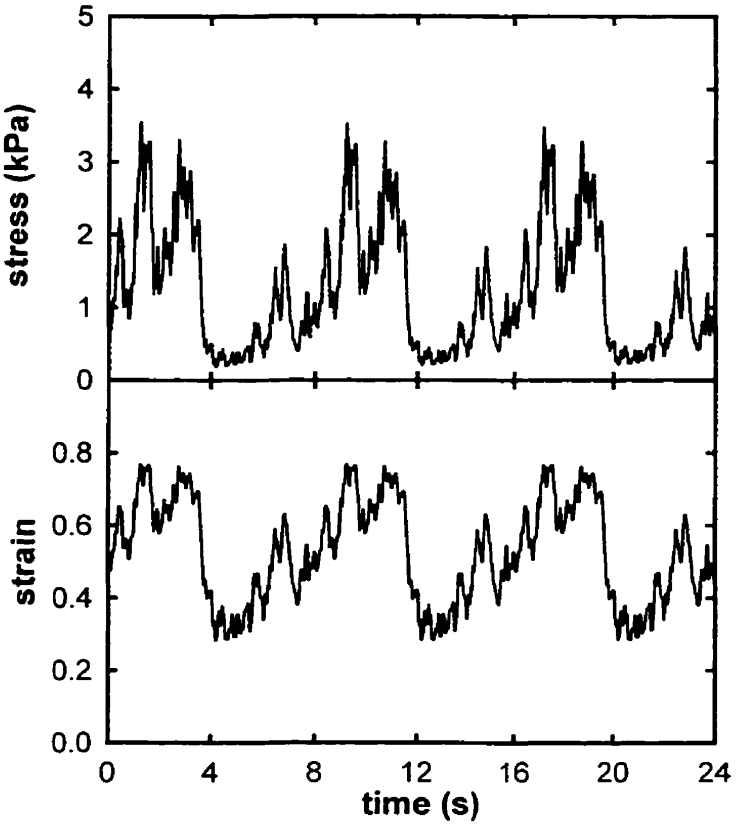


Figure 6-2. Lower panel shows an example of the input signal $\varepsilon(t)$ applied to the lung tissue strip while the upper panel shows the resulting stress signal $\sigma(t)$. The perturbation amplitude range was 0.5 at an operating stress of 1.0 kPa.

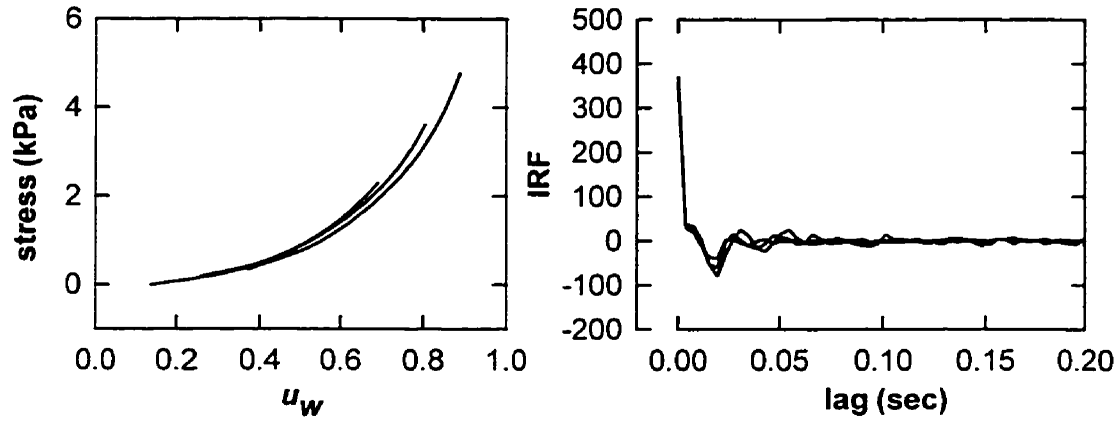


Figure 6-3. Example of Wiener models fitted to data from a single strip for strain amplitude of 0.5 at each operating stress. In the left panel are 5th-order nonlinearities, where the curves from bottom to top correspond to operating stresses of 0.5, 1.0, and 1.5 kPa. In the right panel are the corresponding impulse response functions shown for lags from 0 to 0.2 sec.

### 6.3.1 Estimation of block structured systems.

For all Wiener and Hammerstein models a few iterations were required in the identification process to achieve convergence. The larger the amplitude of the input perturbation, the more iterations were required in general for convergence. The largest number of iterations was 7 for Wiener models and 17 for Hammerstein models, with a mean iteration number of 2.8 (std. dev. 1.3) for Wiener models and 6.5 (std. dev. 4.3) for Hammerstein models. The greatest improvement in the VAF% between the initially identified models and the model of the final iteration was 3.6 % for both Wiener and Hammerstein models. The effect of iterative improvement on the estimate of the linear system block resistance is demonstrated in Figure 6-4. The first estimate for the dynamic linear block is a linear model of the entire system, which is strongly affected by harmonic distortion arising from the nonlinearity (152). However, after 11 iterations the identification process converges on a smoother estimate for $R$ (Fig. 6-4).

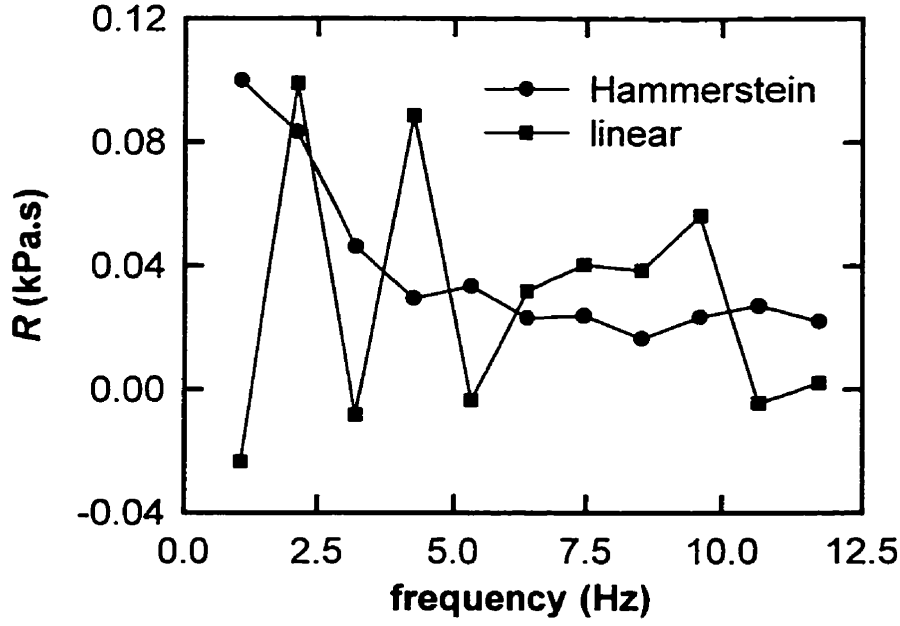


Figure 6-4. Comparison of linear system block $R$ from Hammerstein model with all linear dc gain in the linear system block, to linear model fitted $R$ for a single strip at strain amplitude 0.75 at operating stress of 0.5 kPa.

### 6.3.2 Estimation of polynomial order

Figure 6-5 shows the root mean squared error (RMSE) between $\sigma(t)$ and the predicted output stress for Hammerstein models having increasing polynomial order from 1 to 10 at an operating stress 1.0 kPa. Note that models with polynomials of order one are linear systems. The plot shows that after approximately 5th-order there is essentially no improvement in the RMSE at the highest amplitude. At the lower amplitudes the improvement with increasing order less great, and 3rd-order polynomials suffice. The results at the different operating stresses and for Wiener models were very similar. I thus felt that all significant variation in the data that could be captured by a Wiener or Hammerstein model was achieved with a 5th-order polynomial in the static nonlinearity and therefore used polynomials of this order for all further results and comparisons.

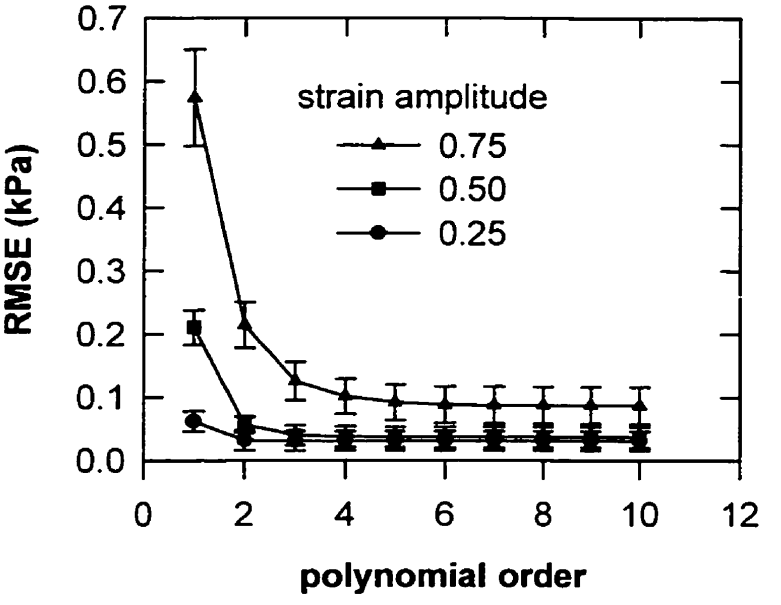


Figure 6-5. The root mean squared error (RMSE) of the Hammerstein models computed with static nonlinear polynomials of order 1 to 10 at a stress level of 1.0 kPa. The symbols are mean values from all strips, and bars indicate standard deviation.

### 6.3.3 Comparison of Hammerstein models to Wiener models

The VAF% calculated between the model predicted output and $\sigma(t)$ are shown in Figure 6-6 for Wiener, Hammerstein, linear, and static nonlinear models. The linear models were fit using Eq. 2-12 and had the same impulse response function length as the linear blocks of the Wiener or Hammerstein models. The static nonlinear models consisted of 5th-order polynomials in every case like the nonlinear blocks of the Wiener and Hammerstein models. All nonlinear models fit the data much better than the linear model. The Wiener and Hammerstein models fit the data nearly identically, and accounted for nearly all the variance in the data, with minimum and maximum values being 98.82 ± 1.39 % and 99.84 ± 0.13 % respectively (mean ± std. dev. across all strips). Both Wiener and Hammerstein models were better than a simple static nonlinear model although the dynamics in either case did not account for much of the variance in the data, with improvements in the VAF% of from 0.4% to 0.8% over the static nonlinear model.

The Kruskal-Wallis test was used to search for any significant difference between the model types at each amplitude and operating stress. If there was any significant difference, the Wilcoxon signed rank test was performed (Winstat: public domain software). In all cases the linear models were different from the nonlinear models ($p<0.05$ for amplitude 0.25, and $p<0.01$ otherwise). Both Hammerstein and Wiener models were different from the static nonlinear model ($p<0.05$) except at amplitude 0.25 where the tests did not indicate any significant difference. The small increases in VAF% from static nonlinear models to the dynamic nonlinear models were due of course to the lung tissue behaviour, but were also due to the amplitude and frequency spectrum of the input used. Since the amplitude of the input perturbations were quite large, this tended to increase the significance of the static nonlinearity relative to the dynamic behaviour. This also tended to emphasise the low frequency behaviour relative to the higher frequency dynamics because most of the signal power was concentrated at low frequencies,.

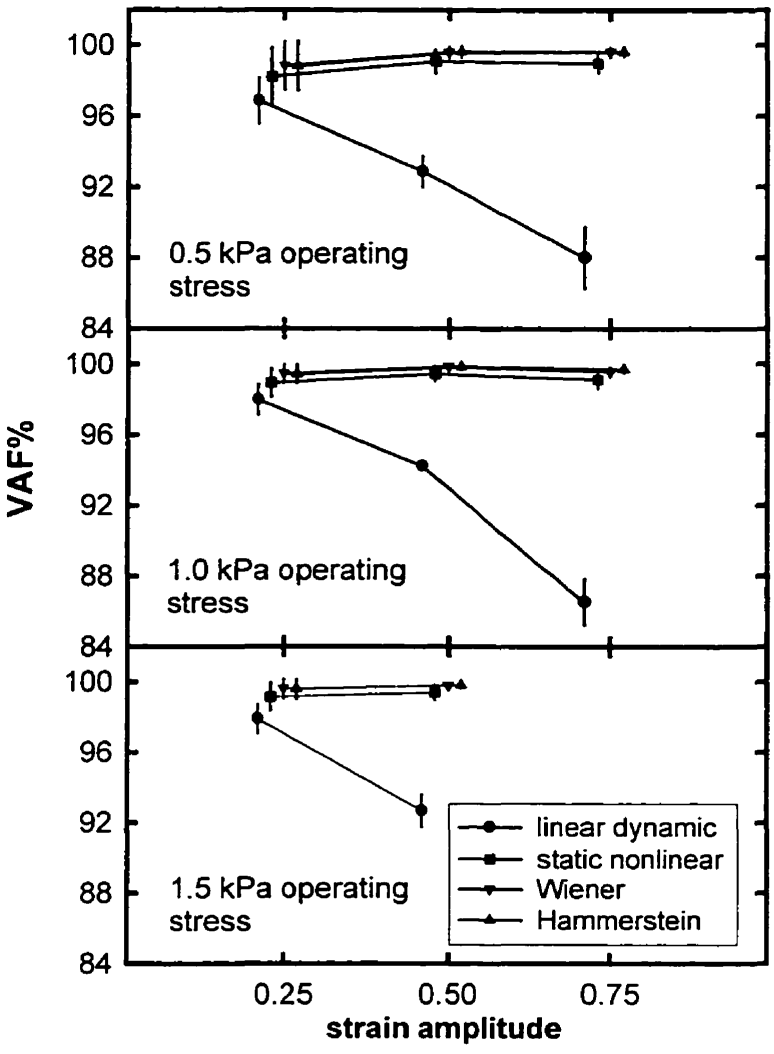


Figure 6-6. Performance of nonlinear models, dynamic linear model and static nonlinear model in terms of VAF% versus strain amplitude, with panels from top to bottom corresponding to operating stresses of 0.5 kPa, 1.0 kPa and 1.5 kPa, respectively. Symbols are mean values across all strips and error bars indicate standard deviation.

### 6.3.4 Nonlinear blocks

Both the Wiener and Hammerstein nonlinear blocks appeared to trace the same underlying curve for all amplitudes and operating stresses, although Wiener nonlinearities

spanned a 5-10% greater range. Figure 6-7 shows the nonlinear blocks from both Wiener and Hammerstein models for all operating stresses and strain amplitudes.

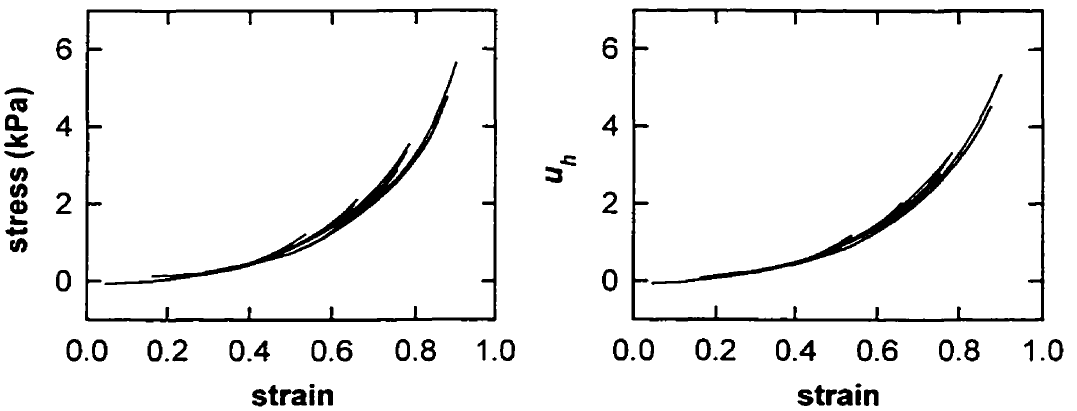


Figure 6-7. Nonlinear polynomials from both Wiener (left panel) and Hammerstein (right panel) models for a single tissue strip, for all strain amplitudes and operating stresses. Strain amplitudes of 0.25, 0.5 and 0.75 are shown for operating stress of 0.5 and 1.0 kPa. Amplitudes of 0.25 and 0.75 are shown for a stress of 1.5 kPa.

### 6.3.5 Linear model blocks

Figure 6-8 shows the frequency dependence of $R$ and $E$ for the dynamic linear blocks of the Hammerstein models for all tissue strips. The left panels show the results for a single strain amplitude (0.5) at each operating stress level. The right panel shows the results for a single operating stress (1.0 kPa) for each strain amplitude. $R$ displays a hyperbolic frequency dependence and $E$ increases with frequency. The fact that $R$ does not decay to zero with increasing frequency is indicative of a Newtonian component to resistance (a component independent of the rate of strain) consistent with the findings of Lutchen et al (90). The important observation from Figure 6-8 is that the linear system blocks are largely independent of both strain amplitude and operating stress. It would thus appear that the Hammerstein model is consistent for changes in amplitude and stress. In contrast, the Wiener models are somewhat less consistent (Fig. 6-9), with $R$ showing a

slight decreasing dependence on operating stress at 0.5 strain amplitude and $E$ showing a slight spreading with frequency. Thus, for the Hammerstein model results, one model may suffice to account for all the data, but there is some slight variation in the data not accounted for by the Wiener structure. However, since there was essentially no difference in model performance at a given amplitude and operating stress (Fig. 6-6), results are shown primarily from Hammerstein models from this point on.

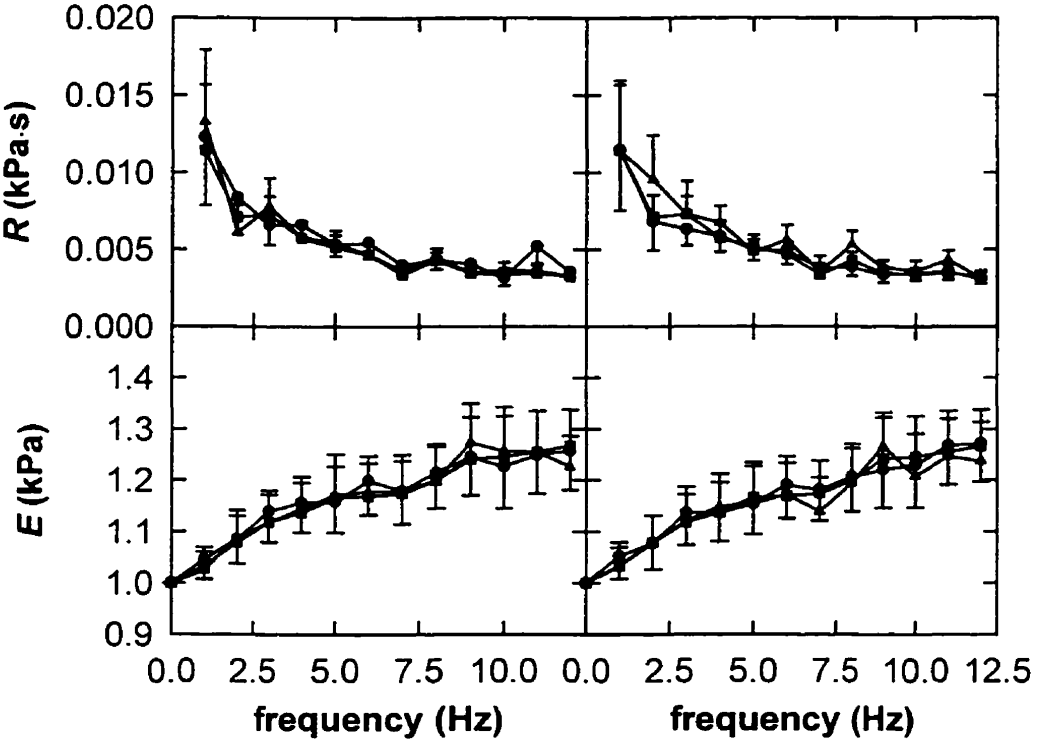


Figure 6-8. Linear blocks from Hammerstein models from all tissue strips. Left panels show $R$ and $E$ at a strain amplitude of 0.5 at each operating stress, while the right panels show $R$ and $E$ pooled from all tissue strips at 1.0 kPa operating stress at each strain amplitude. Error bars indicate standard error.

These results contrast against the findings of Suki et al. (160) (see Chapter 2.3.3) who found that in their parametric block structured models, a Wiener model describing the tissue behaviour provided the best fit to the flow-pressure relationships of canine lungs *in vivo*. However, they used flow rather than volume (analogous to strain) as the

input, and subjected the tissues to much smaller strains about a single operating stress level, corresponding to the functional residual capacity. There is also no guarantee that their tissue compartment represented only stress-strain properties of the tissue. Indeed it likely included effects due to the air-liquid interface, and perhaps even some airway properties. However, the differences that were found between the Wiener and Hammerstein model for the lung tissue strip were minor; thus it is possible that a Wiener model is more appropriate for tissue in the intact lung.

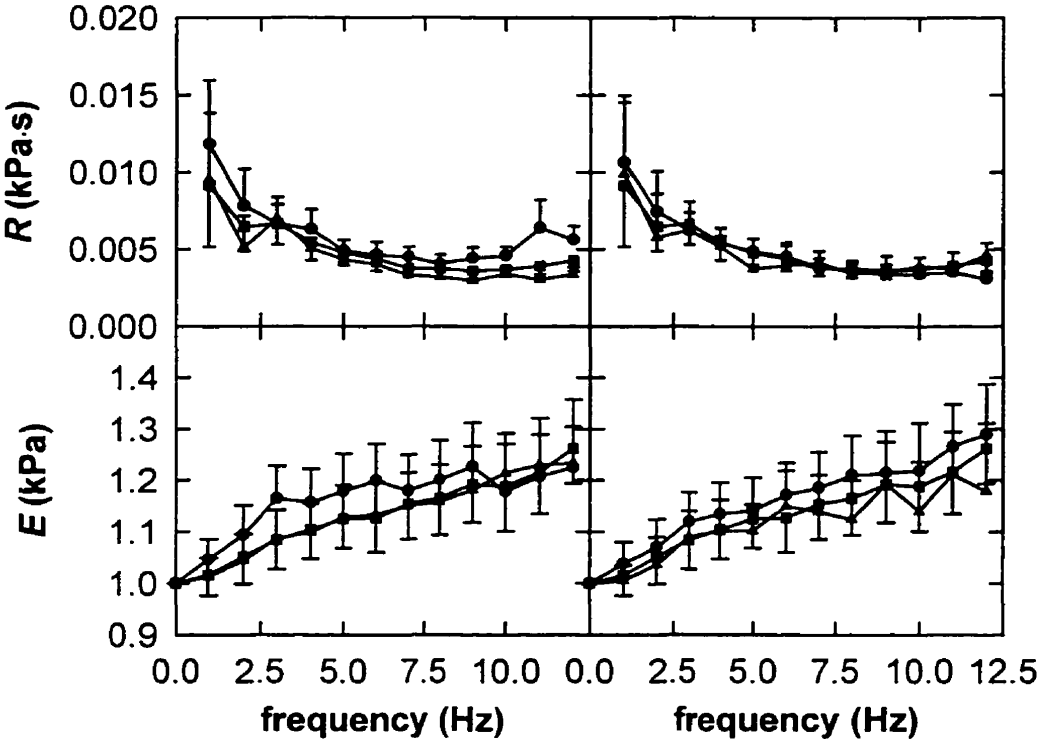


Figure 6-9. Linear blocks from Wiener models from all tissue strips. Left panels show $R$ and $E$ at a strain amplitude of 0.5 at each operating stress while the right panels show $R$ and $E$ pooled from all tissue strips at 1.0 kPa operating stress at each strain amplitude. Error bars indicate standard error.

In both the Wiener and Hammerstein models, it is arbitrary where the dc component of the linear gain is located. This is because the blocks are connected in series, and therefore the static gains of the blocks are multiplicative. Our convention thus

far has been to assign all the static gain to the nonlinear block, which is achieved by fixing the dc gain of the linear system block to unity. The result of this on the linear system blocks can be observed in Figures 6-8 and 6-9, where the 0 Hz term of the elastance is unity (1 kPa). This leads to the important result that for the Hammerstein system and to a large degree for the Wiener system, the linear dynamics are very insensitive to strain amplitude and operating stress. This is unfamiliar to those accustomed to linear models which, when applied to a system with inherent nonlinearities, must exhibit amplitude and operating stress dependence. However, in normalising the linear system in this manner, we cannot compare the values we report for our $R$ and $E$ to that of $R$ and $E$ obtained from linear models, since a large part of the gain of our nonlinear models is located in the static nonlinearity. An alternate choice for the placement of some of the static gain is to normalise the static nonlinearity to the value of its 1st-order coefficient, and correspondingly multiply the dynamic linear block by the same value. Thus all linear characteristics of the model - including the linear term of the static zero memory block - are located in the linear block, and the remaining gain of the static nonlinearity is due only to its higher order coefficients. Under these conditions, nonlinear effects such as harmonic distortion are accounted for, and thus we can still use linear model parameters ($R$ and $E$) to describe the linear system block. These values should then correspond to the usual measurements of $R$ and $E$ obtained using small amplitude perturbations, where the effects of nonlinearities are less significant (35,110). If linear parameters such as $R$ and $E$ are determined from larger amplitude perturbations, then they are sensitive to the method of analysis and type of input, and thus may vary purely as a result of changes in experimental conditions.

The results for the dynamic linear block, under the condition that all linear gain is located in the linear block, are shown in Figure 6-10. Both $R$ and $E$ now scale with operating stress as observed previously in canine lungs (52,156), and also match our observations from sinusoidal oscillation (114). Amplitude dependence is negligible between strain amplitudes of 0.25 and 0.50, but $R$ and $E$ are increased for the largest strain amplitude of 0.75. The increase in $R$ and $E$ with amplitude matches the prediction of the quasilinear theory (Eqs. 6-1, 6-2) that we used in Navajas et al. (114), but does not

match the dependence observed in the sinusoidal oscillation data of that study. The amplitude dependence is also contrary to data obtained in dog lung *in vivo*, which shows an inverse dependence of $E$ and smaller inverse dependence of $R$ on the tidal volume (156).

Another interesting point to be noted when comparing Figures 6-8 and 6-10 is that in Figure 6-8 the standard error in the elastance is apparently increasing, perhaps indicating a reduction in signal-to-noise ratio at high frequencies. However, Figure 6-10 shows no increase in standard error with frequency. Despite the $1/f$ input spectrum there is apparently sufficient signal power at high frequencies to accurately extract the lung tissue behaviour. Thus this effect arises solely from fixing the dc component to unity in Figure 6-8. In any case, locating the linear portion of the static nonlinear zero memory block within the dynamic linear block allows us to compare the amplitude and stress dependence to the results of others. However, this also has the effect that both blocks of the nonlinear models are dependent on strain amplitude and operating stress. That is, there is a different static nonlinear block and linear dynamic block for each measurement condition. This is unreasonable, in view of the fact that a single Hammerstein model can account for all linear dynamics and static nonlinear behaviour at all strain amplitudes and operating stresses.

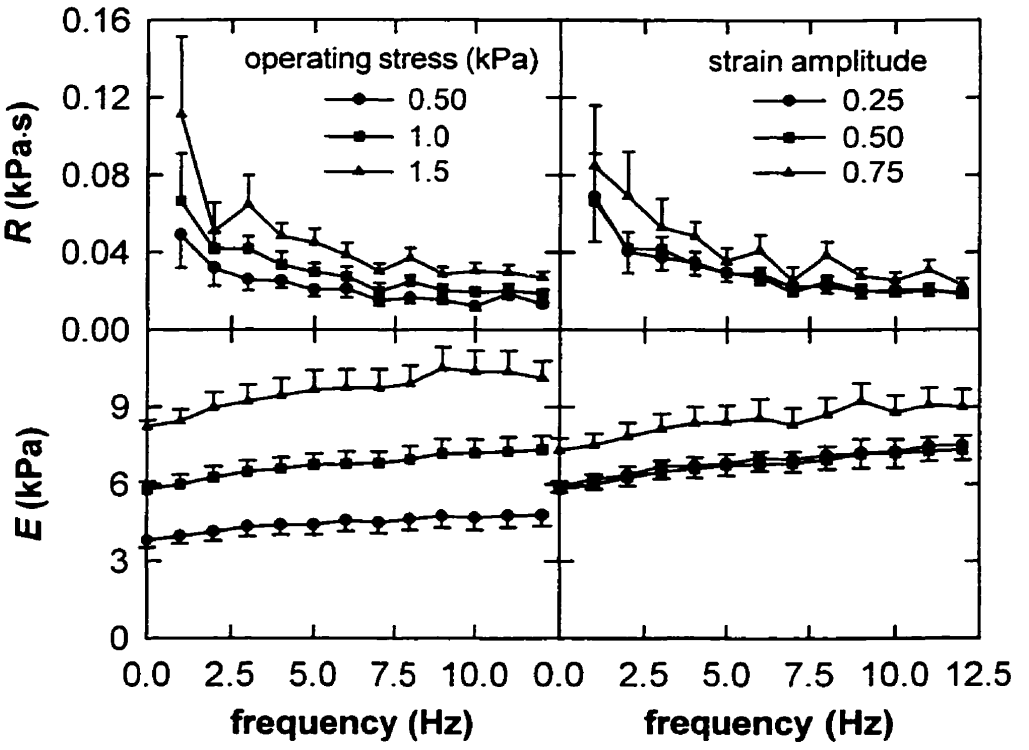


Figure 6-10. *R* and *E* with dc gain located in the linear system block. Left panels: Pooled results from all tissue strips at 0.5 peak-to-peak strain amplitude and different operating stresses. Right panels: Pooled results from all tissue strips at 1.0 kPa operating stress and different strain amplitudes. Error bars indicate standard error.

A principle objective of this study was to investigate the ability of the Wiener or Hammerstein model to describe the data, and thus it is confirmed here that the static mechanical properties of lung tissue are separable from the dynamic properties. This is a necessary requirement for the validity of Chapter 3, where I developed a model which considered only the static elastic behaviour of the lung tissue. I compared the static nonlinearities of both Wiener and Hammerstein models (with all static gain within the static nonlinearity) to the responses obtained during a quasi-static maneuver at the same operating stress and strain amplitude. Figure 6-11 shows the experimentally determined stress-strain loop and the Hammerstein model nonlinearity at an operating stress of 1.0 kPa and strain amplitude of 0.5. The static nonlinearity traces the mid-line of the stress-strain loop, providing convincing evidence that the static nonlinearity reflects the underlying static stress-strain behaviour of the lung tissue. This behaviour was observed irrespective of whether a Wiener or Hammerstein model was used, but only under the condition that all static gain of the models was confined to the static nonlinearity. Figure 6-11 also shows the output of the model driven with the same quasi-static sinusoidal strain input signal that produced the experimental the stress-strain loop (solid line). The loops are quite similar, although the simulated curve underestimates the area enclosed by the data by 26%, which is typical of other loops measured. This is quite similar to the ~30% underestimation of energy dissipation we observed using the quasilinear viscoelastic model (Eqs. 6-1 and 6-2 applied to step perturbation data to predict sinusoidal response).

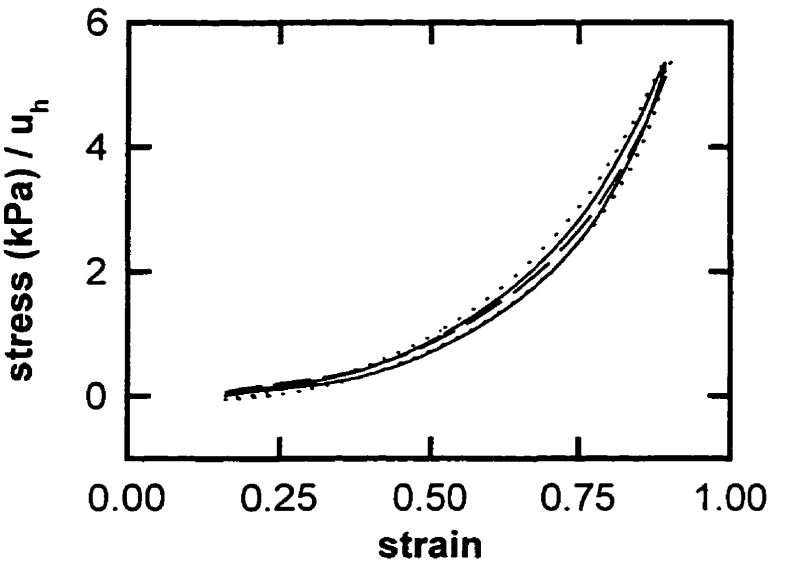


Figure 6-11. Quasi-sinusoidal stress-strain loop obtained at operating stress of 1.0 kPa and strain amplitude of 0.75 (dotted) with corresponding Hammerstein model nonlinearity (dashed) and model output for quasi-static sinusoidal input (solid).

This agreement is somewhat surprising, since the Wiener and Hammerstein models were obtained using stochastic broadband perturbations and contain a large number of parameters, whereas the quasilinear viscoelastic model was obtained from step perturbations and contains only two parameters. This result shows that despite allowing the Hammerstein and Wiener models complete freedom to account for as much of the static nonlinear behaviour and dynamic linear behaviour as possible, neither model can account for all the dissipation of energy during a single low frequency perturbation. This may reinforce the conclusion that some of the dissipative processes within the lung tissue are plastic in origin (see Introduction Section 2.2.3 ***Nonlinear models***), and thus cannot be accurately modelled by the Hammerstein or Wiener structure. This is because the Volterra series, which includes Wiener and Hammerstein models as a subset, cannot model systems with infinite memory such as those exhibiting plasticity.

However, despite the very good performance of the models, and the invariance of the Hammerstein model blocks, the lung tissue may be exhibiting behaviour requiring a

more complex Volterra series representation. The possible presence of plasticity must also be considered with some caution because the length of the impulse response function (IRF) used to predict the sinusoidal loop was only 1 second in length, and thus we can only estimate frequencies as low as 1 Hz, whereas the frequency of the sinusoid was 0.125 Hz. It is conceivable that additional dynamics may exist for longer lags than 1 second, despite the appearance of the IRF's of Figure 6-3 which appear to decay rapidly to zero at much shorter lags. This possibility was tested by re-estimating the models using longer IRF lengths from 2 to 8 seconds, and comparing the predicted loop areas to that of the measured sinusoids at each amplitude and operating stress for a representative tissue strip. Figure 6-12 shows the results of the Hammerstein model in terms of percent of loop area predicted. The estimation of loop area varied among the different amplitudes and operating stresses and underestimated the measured area at all IRF lengths with a minimum of 14 ± 11 % at an IRF length of about 6 seconds. Loop area was better estimated as the IRF length increased to about a lag of 6 seconds; however, for longer lengths the under-estimation increased. It is also observed that the estimation of the model became poor for the longest IRF lengths, and did not predict sinusoidal loops that matched the data. This was expected due to the finite length (24 sec.) of the pseudo-random input used to identify the models, leading to very limited averaging during the estimation of the IRF for long lags. Thus, we cannot rely on the model predictions at long lags and it is likely that the amount of viscoelastic dissipation that could be accounted for by a Wiener or Hammerstein model is greater than we can reliably predict with these data. This implies that the amount of plasticity that may be present in the lung tissues (during sinusoidal cycling) is less than the 30% we previously postulated (114) and is likely less even less than 20%.

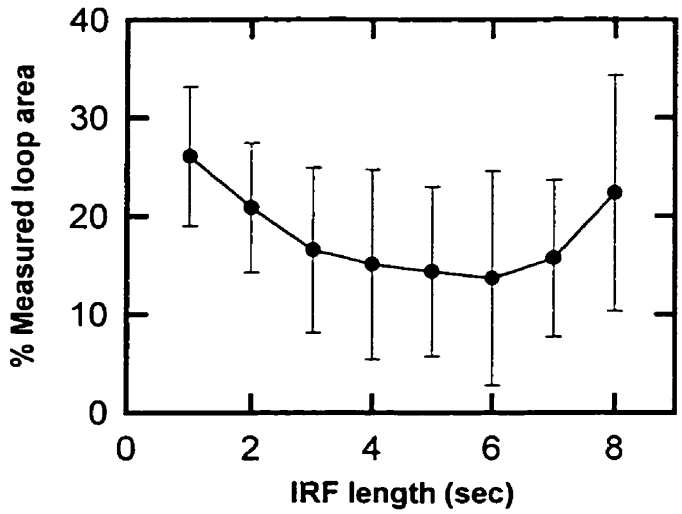


Figure 6-12. Underestimation of stress-strain sinusoidal 0.125 Hz loop area by simulated output of Hammerstein model. Symbols and error bars are means ± standard deviations at all strain amplitudes and stress levels recorded in a representative tissue strip (n=8).

### 6.3.6 Parallel system

The ability of both the Wiener and Hammerstein structures to model the data nearly equally well is intriguing. The Hammerstein system output $y(t)$ to an input $x(t)$ is

$$y(t) = a_0 + \sum_{i=1}^{n} \int_0^{\infty} a_i h_1(\tau_1) x'(t-\tau_1) d\tau_1 , \qquad (6\text{-}6)$$

where $a_i$ are the coefficients of an $n^{th}$-order nonlinear polynomial. The Volterra series kernels are thus simply scaled versions of the first-order kernel, with value only on the principal diagonals

$$h_i(\tau_1,\ldots\tau_i) = a_i h_1(\tau)\delta(\tau_1-\tau_2)\delta(\tau_1-\tau_3)\cdots\delta(\tau_1-\tau_i) \qquad (6\text{-}7)$$

for $i = 1...n$, where $\delta(\tau_1 - \tau_i)$ is the Dirac delta function. Similarly, the output of a Wiener system is

$$y(t) = \sum_{i=o}^{n} a_i \left[ \int_0^{\infty} h_1(\tau_1) x(t-\tau_1) d\tau_1 \right]^i . \qquad (6\text{-}8)$$

so that the kernels of order higher than 1 in the Volterra series are higher order powers of the first-order kernel, thus

$$h_i(\tau_1, \ldots \tau_i) = a_i [h_1(\tau_1) \cdots h_1(\tau_i)] \qquad (6\text{-}9)$$

for $i = 1 \ldots n$, and can have value for any $\tau_i$ depending on the form of $h_1$. Thus, the Volterra kernels for the Hammerstein and Wiener models are necessarily different. Yet our results indicate that both the Wiener and Hammerstein models account nearly equally for the system behaviour (Fig. 6-6), and indeed have very similar forms for their dynamic linear blocks (Fig. 6-8, 6-9). If the lung tissue can be represented by a Volterra series, it is unlikely that two different Volterra series models can represent the same system. This may mean that neither model represents the true underlying system (after all even though the VAF% are very high they are not 100%), and even that the system contains features that the Volterra series cannot model such as plasticity. In any case, considering the similar performances of the Wiener and Hammerstein models, I wondered whether a parallel arrangement of the nonlinear and dynamic blocks could account also for the lung tissue behaviour. This model is shown in Figure 6-13 and consists of a dynamic linear system $h_p(\tau)$ in parallel with a nonlinear polynomial $m_p$.

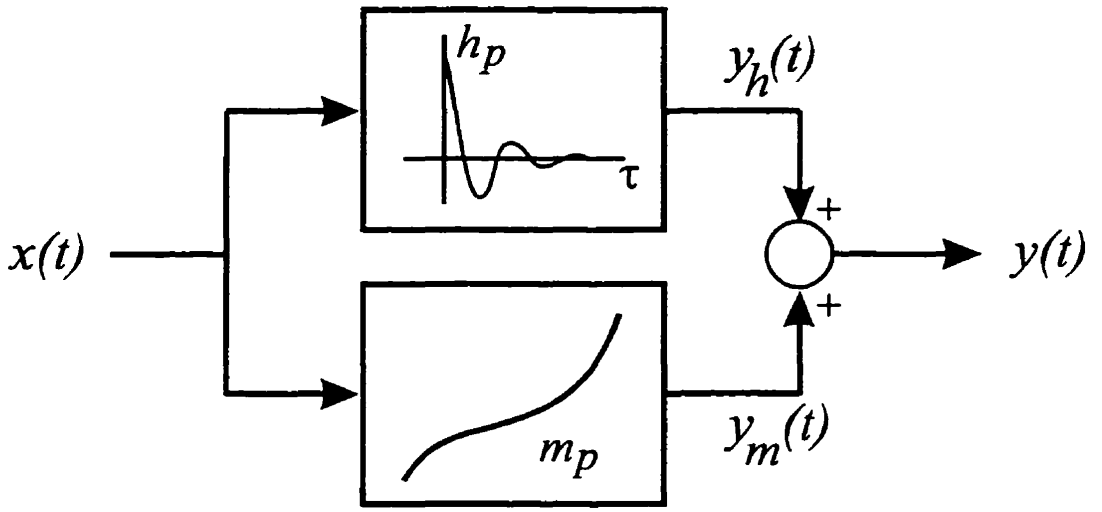


Figure 6-13. The parallel linear-nonlinear model. The input $x(t)$ is fed into both the linear block $h_p(\tau)$ and the nonlinear block containing the polynomial $m_p$, and the outputs of each are summed to give the model output $y(t)$.

The output of this system is

$$y(t) = \int_0^\infty h_1(\tau_1)x(t-\tau_1)d\tau_1 + \sum_{i=0}^{n} a_i x^i(t), \tag{6-10}$$

for which the higher order $i \geq 2$ Volterra kernels are

$$h_i(\tau_2,\ldots\tau_i) = a_i\left[\delta(\tau_2)\cdots\delta(\tau_i)\right], \tag{6-11}$$

and are thus zero except at zero lag. The system dynamics thus arise only from the linear impulse response, and nonlinear effects in the system output arise solely from a nonlinear function of the input. This is an attractive hypothesis for the lung tissue, since with this simple structure one can easily use lumped elements to model the different mechanical behaviours: all nonlinear aspects could be modelled as a nonlinear spring while all linear dynamics could modelled in parallel with appropriately chosen lumped elements to account for the linear viscoelastic behaviour. Thus, dynamic behaviour is completely independent of static elastic behaviour. Suitable candidates for the two blocks could be the distributed nonlinear model proposed in Chapter 3 of this thesis for the nonlinear elastic spring, while for the linear viscoelastic model, the Hildebrandt model (Eq. 2-3) or the constant phase model (Eq. 2-5) could suffice.

I developed an iterative identification scheme very similar to that used to identify the Wiener and Hammerstein models. The first estimate of the nonlinearity $m_p$ is fitted between the $x(t)$ and $y(t)$ in the least squares sense. The output of the nonlinear block $y_m(t)$ is then subtracted from $y(t)$ and $h_p(\tau)$ is estimated between $x(t)$ and $y(t)$ - $y_m(t)$ via Toeplitz matrix inversion (Eq. 2-12). The VAF% is then calculated between $y(t)$ and the predicted model output. Iterative improvement continues by subtracting the output of the linear block, $y_h(t)$, from $y(t)$ and a new estimate of $m_p$ is obtained between $x(t)$ and $y(t)$ - $y_p(t)$. The process proceeds by re-estimating $h_p(\tau)$ and $m_p$ until the improvement between successive VAF% is less than $10^{-6}$. To compare directly with the Wiener and Hammerstein results, the length of the $h_p(t)$ was limited to 1 sec and $m_p$ was 5th-order. The model converged in 5.3 ± 2.4 (mean ± std. dev.) iterations with the maximum number of iterations being 11 among all data records. The maximum improvement in VAF% from the first iteration to the final model was 0.046%. The nonlinearities identified from a single strip are shown in Fig. 6-14, and the linear block results for amplitudes and operating points are shown in Fig. 6-15. Comparison of model performance in terms of the root mean squared error (RMSE) with the Wiener, Hammerstein and static nonlinear models is shown in Figure 6-16.

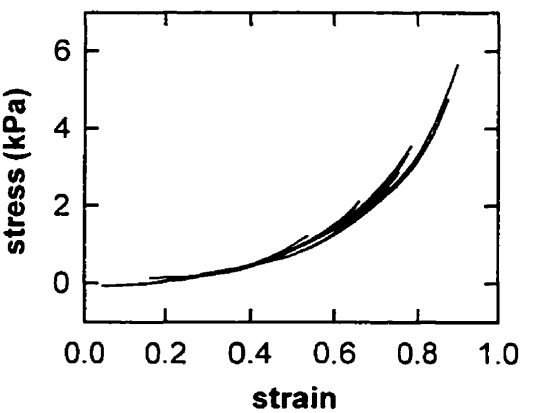


Figure 6-14. Representative nonlinearities from parallel models fitted to a single strip, corresponding to that of Figure 6-7 for the same amplitudes and operating stresses.

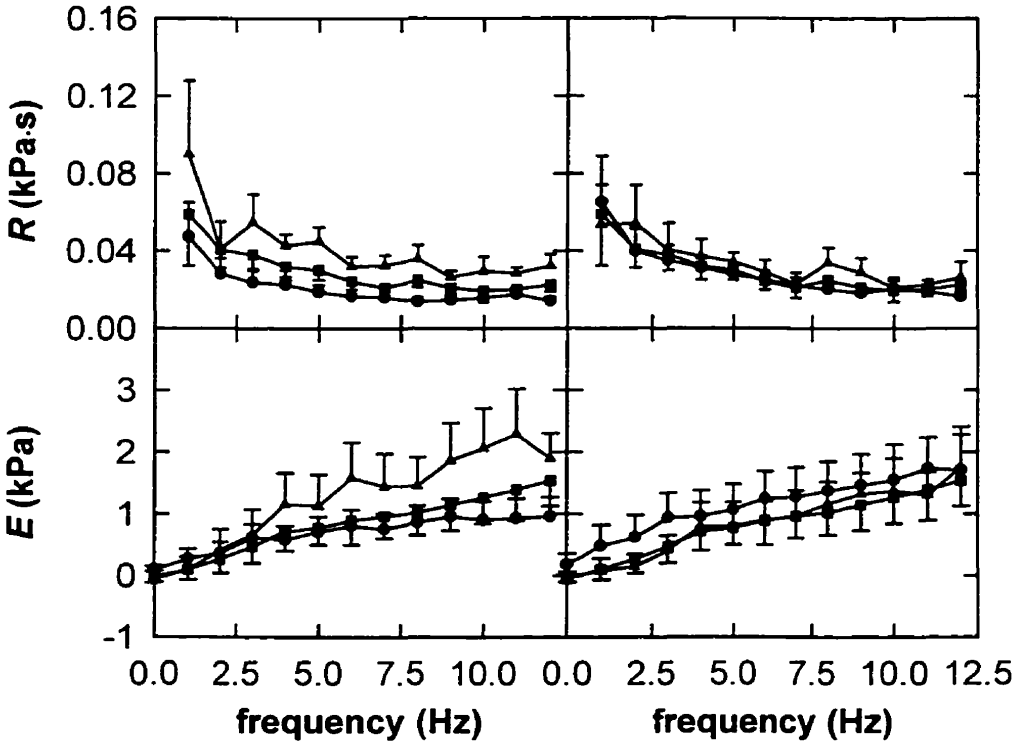


Figure 6-15. $R$ and $E$ of linear block of parallel models. Left panels show $R$ and $E$ at strain amplitude of 0.5 at each operating stress while the right panels show $R$ and $E$ pooled from all tissue strips at 1.0 kPa operating stress at each strain amplitude. Error bars indicate standard error.

The parallel models exhibit greater amplitude and operating stress dependent behaviour (Fig 6-15) than the Wiener models (Fig. 6-9). The nonlinear curves (Fig. 6-15) also do not follow a single function as well as those of the other nonlinear models (Fig. 6-7). Furthermore, as shown in Figure 6-16, the RMSE is less than that of the static nonlinear models, particularly at high amplitudes and operating stresses (and much less than the linear models - not shown). Thus, although the parallel model accounts for much of the system behaviour, both the Hammerstein and Wiener models are superior. This leads to the conclusion that the tissue mechanical properties are more complex than can be accounted for with the parallel model structure, and thus are not easily amenable to modelling approaches using lumped elements.

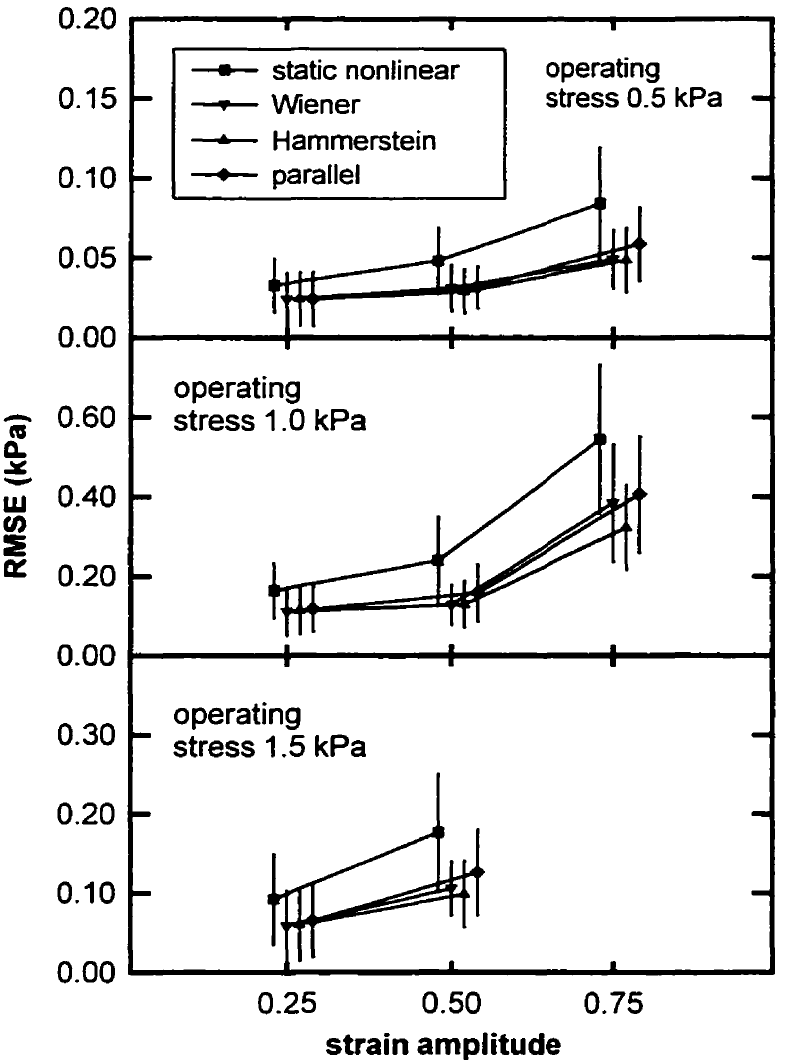


Figure 6-16. Comparison of parallel model to Wiener, Hammerstein and static nonlinear models in terms of the RMSE at each amplitude for operating stress levels from top to bottom of 0.5, 1.0 and 1.5 kPa. Symbols are mean values across all strips and error bars indicate standard deviation.

## 6.4 Summary

In this chapter I have applied nonlinear block structured models in nonparametric form to large amplitude pseudo-random perturbations of uniaxially stretched lung tissue strips. The Hammerstein and Wiener models fitted the data well, accounting for greater than 99% of the output variance. However, the Hammerstein model was more consistently accurate across different amplitudes and operating stresses. The Wiener and Hammerstein models were also better able to account for the dissipation during slow sinusoidal cycling of the tissue strip than the two parameter nonlinear quasi-linear viscoelastic model of our earlier study (114). However, neither model completely accounted for all the dissipation. We cannot conclude from these data whether the additional dissipation observed was due to very long memory viscoelastic dynamics, or whether a small amount of plastic behaviour contributed to the dissipation during sinusoidal cycling. Furthermore, a parallel arrangement of the blocks fitted the data nearly as well as the serial models, indicating that to a large degree, the elastic behaviour is independent of the dynamic behaviour. Even so, the Hammerstein model provided the best fits to the data and was the most consistent model across different amplitudes and operating stresses. Thus, apart from the possible presence of small plastic effects, one can completely separate static elastic behaviour from the dynamic linear behaviour of lung tissue using a block structured approach.

# 7. Nonlinear block structured modelling of lung mechanics *in vivo*

## 7.1 Introduction

The importance of the lung tissue mechanics to the mechanical properties of the whole lung is well established (37,58). Essentially the same behaviour that is demonstrated in the lung tissue is present in the whole lung. For example, the static pressure volume (*PV*) curve of the lung is nonlinear and exhibits hysteresis between inflation and deflation (58,132). The dynamic mechanical impedance of the lung exhibits amplitude and volume dependence (7,26,156), and insofar as the origins of these characteristics arise within the lung tissue, these nonlinear effects have been ascribed to both nonlinear viscoelasticity (114,155) and plastoelasticity or viscoplasticity (58,144,145). Models of these processes have typically involved lumped parameter constructs such as Maxwell, Voigt, or Prandtl bodies that exhibit the desired behaviour (58,144,145). Recently however, the block structured Wiener and Hammerstein models have been applied to the study of lung mechanics (95,152,160). Suki et al. (160) identified both Wiener and Hammerstein models in dogs under both control and bronchoconstricted conditions. They used the models to represent tissue mechanics over the tidal range of breathing, and were able to account for both the frequency and amplitude dependence of lung impedance. However, they assumed specific functional forms for both the dynamic linear and static nonlinear blocks, which may have imposed inappropriate restrictions on their results. They also assumed that the Wiener or Hammerstein models formed only a part of a more complex model which contained additional parameters attributed to airway properties. In this chapter, I thus examine the ability of the more general nonparametric forms of the Wiener and Hammerstein models to describe *in vivo* rat lung mechanics over the entire pressure-volume range of the lung.

## 7.2 Methods

### 7.2.1 Animal preparation and perturbation protocol

Five adult male Brown-Norway rats weighing 300 +/- 40 g (mean +/- standard deviation) were studied. The rats were anaesthetised by i.p. injection of sodium pentobarbitol (8.5 mg) and the trachea cannulated with a 12-gauge metal needle. The rats were then paralysed with an i.p. bolus of succinylcholine (0.1 mg). The chest was opened widely by mid-line sternotomy. Regular mechanical ventilation was performed by a computer controlled piston-type oscillator (small animal ventilator, SAV, (136)). Inspiration was quasi-sinusoidal at 100 breaths/min. with tidal volumes fixed at 2-3 ml for each animal approximately proportional to animal weight. Expiration was passive through a water trap adjusted to maintain the desired level of positive end-expiratory pressure (PEEP). Broad spectrum volume perturbations were applied at PEEP levels of 0.2, 0.4, 0.6 and 0.8 kPa. The perturbation protocol for a given level of PEEP proceeded as follows. The lungs were inflated to total lung capacity (TLC) by clamping the expiratory line for 1 to 3 breaths. After a further 30 seconds of normal ventilation, a 12 second sinusoidal volume perturbation of 0.25 Hz and 4 ml amplitude range was given. Four volume perturbation signals (described below) of identical form but of different amplitude ranges (1, 2, 3 and 4 ml) were then applied with at least 90 seconds of normal ventilation between each perturbation. A final TLC maneuver and sinusoidal oscillation were applied before changing the PEEP level.

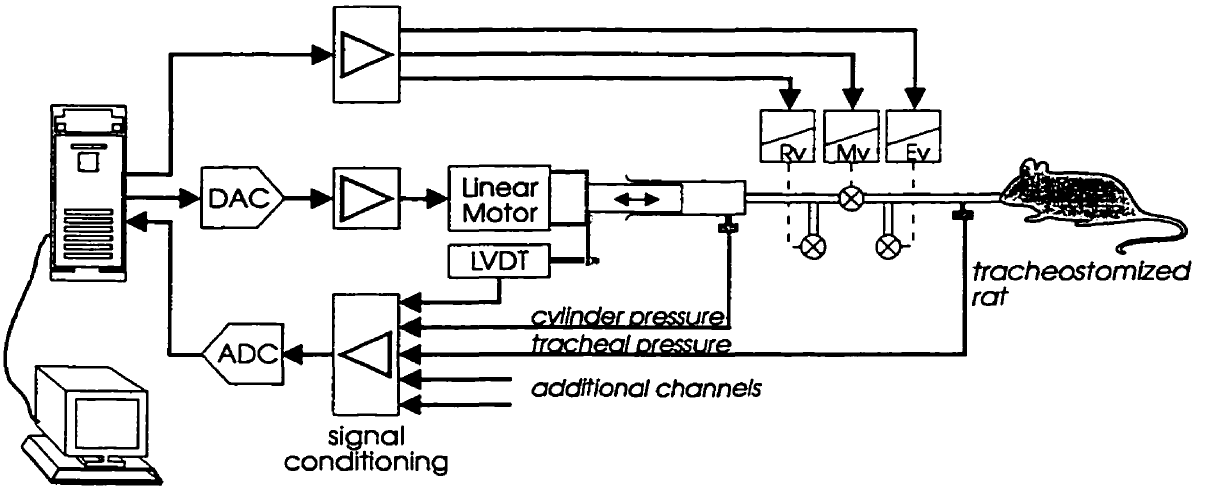


Figure 7-1. Schematic of the small animal ventilator (SAV).

### 7.2.2 Input signals

The input volume perturbation was a pseudo-random noise signal of rectangular amplitude probability distribution and $1/f$ frequency distribution. The signal was exactly the same as used for the input signal in the previous chapter (Section 6.2.1), except that it was 12 seconds long rather than 24 seconds, and contained frequencies from 0.25 to 25 Hz rather than from 0.125 to 12.5 Hz. The signal was scaled so that the peak-to-peak volume excursions were 1, 2, 3 and 4 ml. The flow spectrum was thus approximately flat between 0 and 25 Hz, with root mean squared flow levels of 0.5, 1.0, 1.5 and 2 ml/sec. Perturbations were started at a point mid-way in the range of volume excursions so that the mean lung volume equalled the functional residual capacity (FRC) as determined by the PEEP.

### 7.2.3 Data Collection

During perturbation the SAV piston volume displacement ($v_{cyl}(t)$) and the pressure within the cylinder ($p_{cyl}(t)$) were continuously recorded at 1024 Hz after being filtered at 200 Hz with 6-pole low-pass Bessel filters. The data were then digitally low-pass filtered (6-pole Bessel) to 40 Hz and decimated to 256 Hz sampling rate prior to data storage. However, $v_{cyl}(t)$ and $p_{cyl}(t)$ include effects due to the intrinsic impedance of the SAV,

namely the gas compression within the piston cylinder (from the shunt impedance) and the pressure drop along the flow pathway into the animal (from the impedance of the tubing). To calculate the actual pressure at the trachea and the volume entering the animal by correcting for the impedance of the SAV, we performed two calibration experiments using the input perturbation sequence of 1 ml amplitude range prior to attachment of the rat to the ventilator. These calibration experiments consisted of applying the perturbation sequence once with the outlet of the SAV clamped closed and again with the outlet open to the atmosphere. A schematic of the SAV impedances during the closed and open calibrations and with the animal on the ventilator are shown in Figure 7-2.

The shunt impedance was calculated in the frequency domain from the closed calibration using spectral averaging with Hamming window length of 512 points and 50% overlap as

$$Z_{sh} = P_{cyl} / V_{cyl} \ , \tag{7-1}$$

while the open impedance was calculated from the open calibration as

$$\begin{aligned} Z_o &= P_{cyl} / V_{cyl} \\ &= \frac{Z_{tb} Z_{sh}}{Z_{tb} + Z_{sh}} , \end{aligned} \tag{7-2}$$

from which one can solve for the impedance of the tubing, $Z_{tb}$. Impedances were then interpolated back to the original data length of 3072 points using lowpass filtered interpolation so that $V$ and $P$ could be calculated. With the rat attached to the SAV, the volume of gas entering the trachea was computed as

$$V = V_{cyl} - P_{cyl} / Z_{sh} , \tag{7-3}$$

and the pressure presented to the trachea was

$$P = P_{cyl} - V Z_{tb} . \tag{7-4}$$

The time domain signals for pressure $p(t)$ and volume $v(t)$ were obtained by taking the inverse Fourier transforms of $V$ (Eq. 7-3) and $P$ (Eq. 7-4).

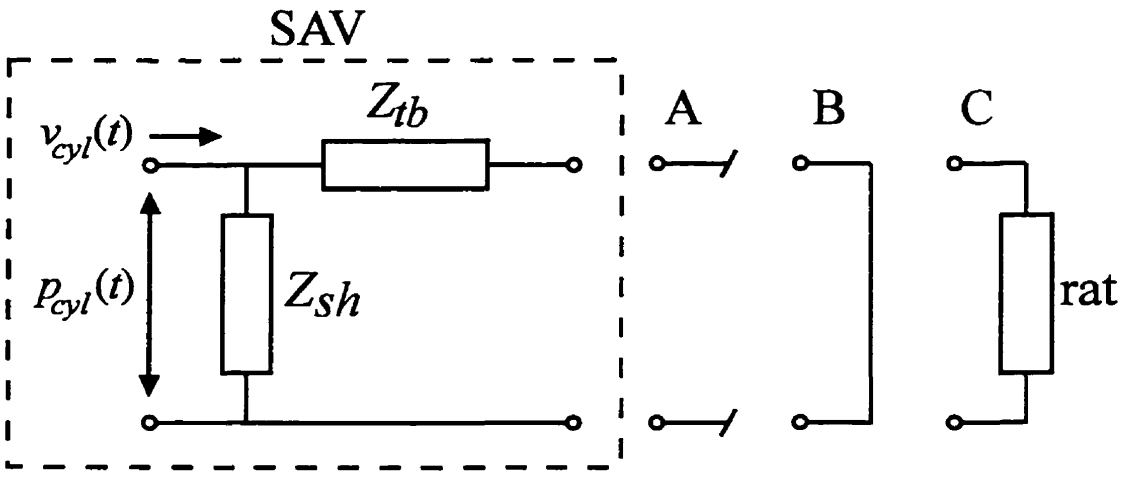


Figure 7-2. Impedance structure of the SAV with three load conditions: A) the tracheal tube is clamped shut so that $P_{cyl}$ is related to $V_{cyl}$ through $Z_{sh}$, B) the tracheal tube is open to atmosphere so that $P_{cyl}$ and $V_{cyl}$ are related through the parallel combination of $Z_{sh}$ and $Z_{tb}$, and C) with the tracheal tube in place connected to the rat lung.

### 7.2.4 System identification - Wiener and Hammerstein models

The identification method used was exactly that applied to the lung tissue strip data of the previous chapter (Section 6.2.2) and that of Hunter and Korenberg (63) described in Chapter 2.3.2. The system input was the volume signal $v(t)$, and the system output was the pressure $p(t)$. Polynomials of order 2 to 10 were estimated, and impulse response functions were one-sided of 1 second duration. The iterative identification was terminated when improvement in the VAF% between $p(t)$ and the model output was less than $10^{-6}$. Unless otherwise indicated, the linear system block dc gain was fixed to unity, so that all static gain was located in the nonlinearity.

To interpret the results in a manner consistent with current methods in the study of respiratory mechanics, methods similar those of Chapter 6 are employed. We transform the impulse response functions, $h(t)$, of the dynamic linear blocks to $H(f)$ in the frequency domain using Eq. 6-3. We represent the dynamics of the linear system as the

complex frequency domain ratio between pressure and flow $\dot{v}(t)$, the time derivative of $v(t)$, thus

$$\begin{aligned} Z_L(f) &= P(f) / \dot{V}(f) \\ &= R_L(f) - i\, E_L(f)/2\pi f \end{aligned}, \tag{7-5}$$

where $P(f)$ and $\dot{V}(f)$ are the Fourier transforms of $p(t)$ and $\dot{v}(t)$, respectively. $R_L(f)$ is called resistance and is that part of the impedance in phase with $\dot{V}(f)$, $E_L(f)$ is that part of the impedance in phase with the volume $V(f)$, and $i$ is positive square root of -1. Thus $R_L$ and $E_L$ in this chapter are used exactly in the same manner as $R$ and $E$ of Chapter 6, where it is understood that $R_L$ and $E_L$ refer to parameters derived from volume-pressure input-output data, rather than strain-stress data as for $R$ and $E$ of the previous chapter. To calculate $Z_L(f)$ from $H(f)$ of volume-pressure data we have

$$Z_L(f) = \frac{-iH(f)}{2\pi f}. \tag{7-6}$$

## 7.3 Results

Figure 7-3 shows a typical input $v(t)$ record of 4 ml amplitude range together with the output $p(t)$ record, both computed from $v_{cyl}(t)$ and $p_{cyl}(t)$ from a single rat subjected to perturbations about a mean PEEP of 0.6 kPa.

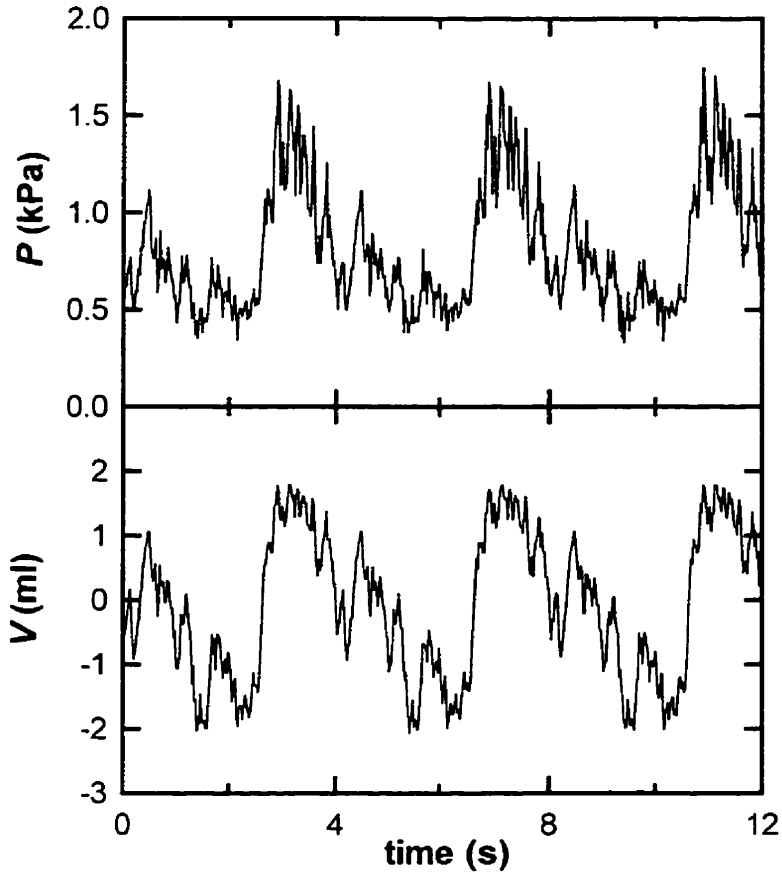


Figure 7-3. Lower panel shows an example of the input volume signal $v(t)$ applied to the lung while the upper panel shows the computed pressure signal $p(t)$ at the trachea. The perturbation amplitude range was 4 ml, and the applied PEEP was 0.6 kPa.

### 7.3.1 Estimation of block structured systems

For much of the data the best Wiener or Hammerstein model fit was achieved from the first iteration in the system identification process. At the higher amplitudes and especially at the highest PEEPs, more iterations were required. The largest number of iterations was 8 for Wiener models and 16 for Hammerstein models, with a mean iteration number of 1.9 (std. dev. 0.5) for Wiener models and 2.9 (std. dev. 0.2) for Hammerstein models. The greatest improvement in the VAF% between the initially

identified models and that of the final iteration was 1.7 % for Wiener models and 0.5 % for Hammerstein models.

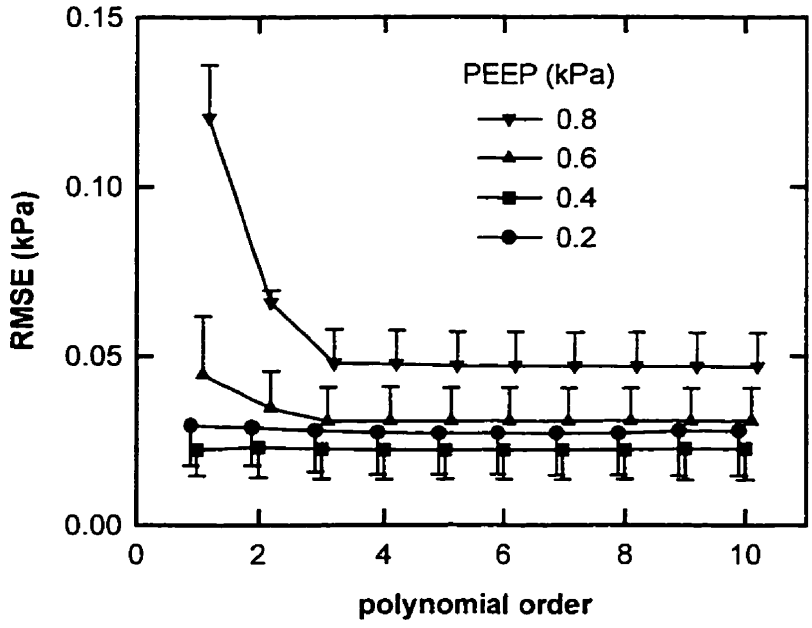


Figure 7-4. The root mean squared error (RMSE) of the Hammerstein models computed with static nonlinear polynomials of order 1 to 10. Perturbations amplitudes of 4 ml for each PEEP were used. The symbols are mean values from all rats, and bars indicate standard error.

### 7.3.2 Estimation of polynomial order

Figure 7-4 shows the root mean squared error (RMSE) between $p(t)$ and the predicted output pressure of the Hammerstein model for increasing polynomial order from 1 to 10 (first order models are linear systems). The largest amplitude oscillation (4 ml) was used at each PEEP level. The plot shows that after 3rd order there is essentially no improvement in the RMSE for all PEEPs. The improvement in RMSE from 1st to 3rd order was substantial for 0.6 and 0.8 kPa PEEP but was very slight for models from data collected at PEEPs of 0.2 and 0.4 kPa. The results for Wiener models were very similar.

Since all significant variation that could be captured by a Wiener or Hammerstein model is achieved by 3rd order, we use polynomials of this order for all further results and comparisons. A typical plot of Hammerstein model nonlinear polynomials for all perturbation amplitudes and all PEEP levels obtained from a single rat is shown in Figure 7-5. Note that the volume axis for each PEEP corresponds to the amplitude of perturbation about the mean volume which was determined by the PEEP and defined to be zero ml for each perturbation.

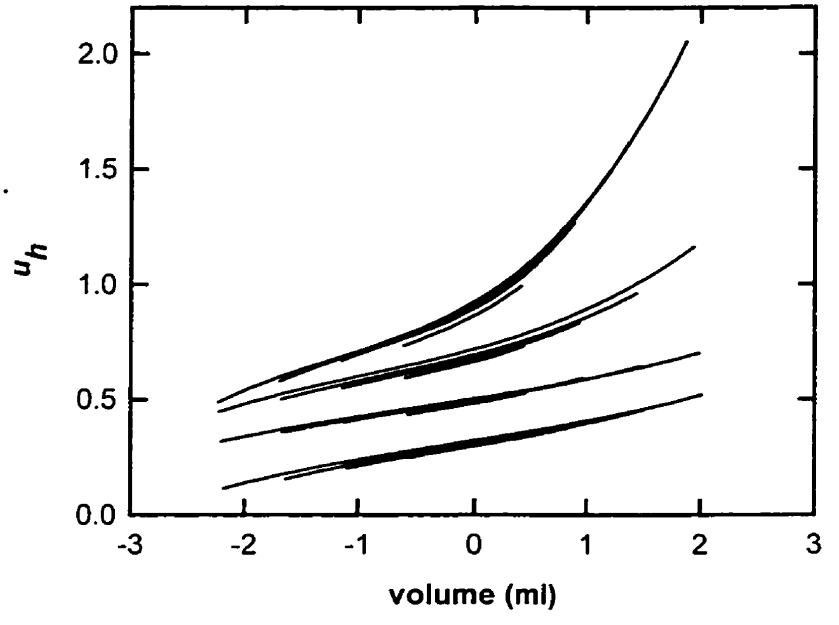


Figure 7-5. Representative example of all the Hammerstein model static nonlinearities estimated from a single rat. The curves are in clusters, each cluster representing PEEPs of 0.2, 0.4, 0.6 and 0.8 kPa while within each cluster the curves in order of increasing length come from perturbation amplitude ranges of 1, 2, 3, and 4 ml.

### 7.3.3 Comparison of Hammerstein models to Wiener models

The RMSE calculated between the model predicted output and $p(t)$ obtained from perturbations of the highest amplitude (4 ml) at each PEEP for linear models and 3rd

order nonlinear block structured models are shown in Figure 7-6. For the pooled data across animals, at PEEP levels of 0.2 and 0.4 kPa, Wiener, Hammerstein and linear models all provided essentially identical fits to the data. However, both nonlinear models were better than the linear model at PEEP 0.6 and 0.8 kPa, and the Hammerstein model performed better than the Wiener model. In terms of VAF%, at the highest PEEP and largest perturbation amplitude the VAF% for the Hammerstein, Wiener and linear models were 98.83 ± 0.58 %, 98.07 ± 0.65 % and 93.00 ± 0.56% (mean ± std. dev), respectively. Since the Hammerstein model outperformed the Wiener model at PEEP 0.8 kPa and there was little difference between the models otherwise, we focus primarily on Hammerstein models from now on.

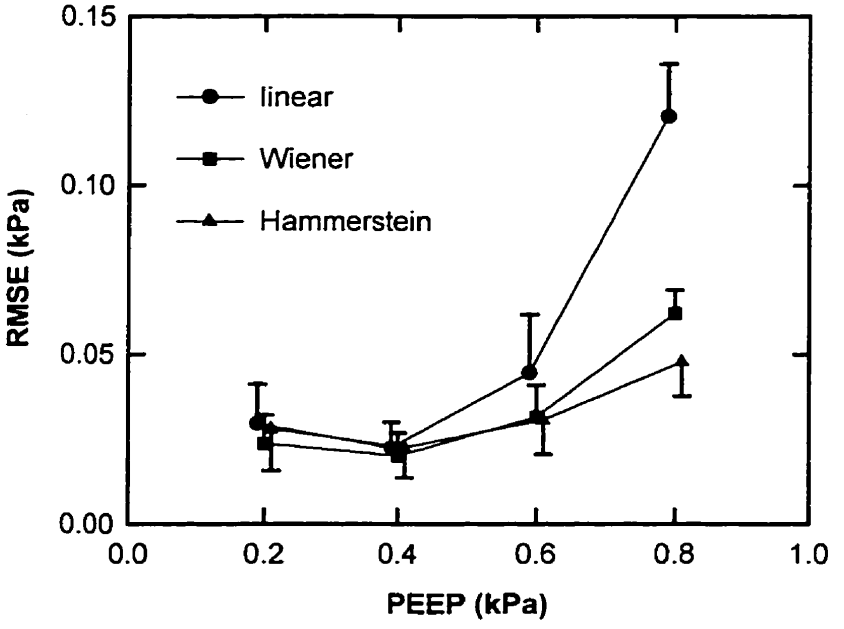


Figure 7-6. Comparison of the RMSE obtained with the linear model and the Wiener and Hammerstein models containing 3rd order polynomials in the static nonlinearity. The perturbation amplitude range was 4 ml at each PEEP level. The symbols are mean values from all rats, and bars indicate standard deviation.

### 7.3.4 Hammerstein linear model blocks

Figure 7-7 shows the frequency dependence of $R_L$ and $E_L$ for the dynamic linear blocks of the Hammerstein models for the pooled animals. The left panels are calculated from perturbation amplitudes of 1 ml for each PEEP while the right panels show the results from perturbation amplitudes of 4 ml for each PEEP. From both 1 ml and 4 ml perturbations, the $R_L$ display hyperbolic frequency dependencies which asymptote to fixed values at higher frequencies. The $R_L$ values are also vertically ordered with decreasing PEEP. The PEEP dependence of $R_L$ is also greater for the 4 ml amplitude perturbations. It can be seen from the right panels of Figure 7-7 that the dc value for $E_L$ is fixed at 1 kPa/ml, as this is a constraint of the system identification process. The $E_L$ at 1 ml perturbation shows a relatively smooth frequency dependence, first increasing and then declining at higher frequencies, presumably due to the onset of inertive effects. At 4 ml amplitude, the low frequency behaviour is similar, but there is little evidence of $E_L$ decreasing at higher frequencies perhaps indicating some amplitude dependence of $E_L$. However, the noise-like variability in the estimates at 4 ml make this unclear. Both $R_L$ and $E_L$ show greater variability among the animals at 4 ml perturbation amplitude than at 1 ml amplitude.

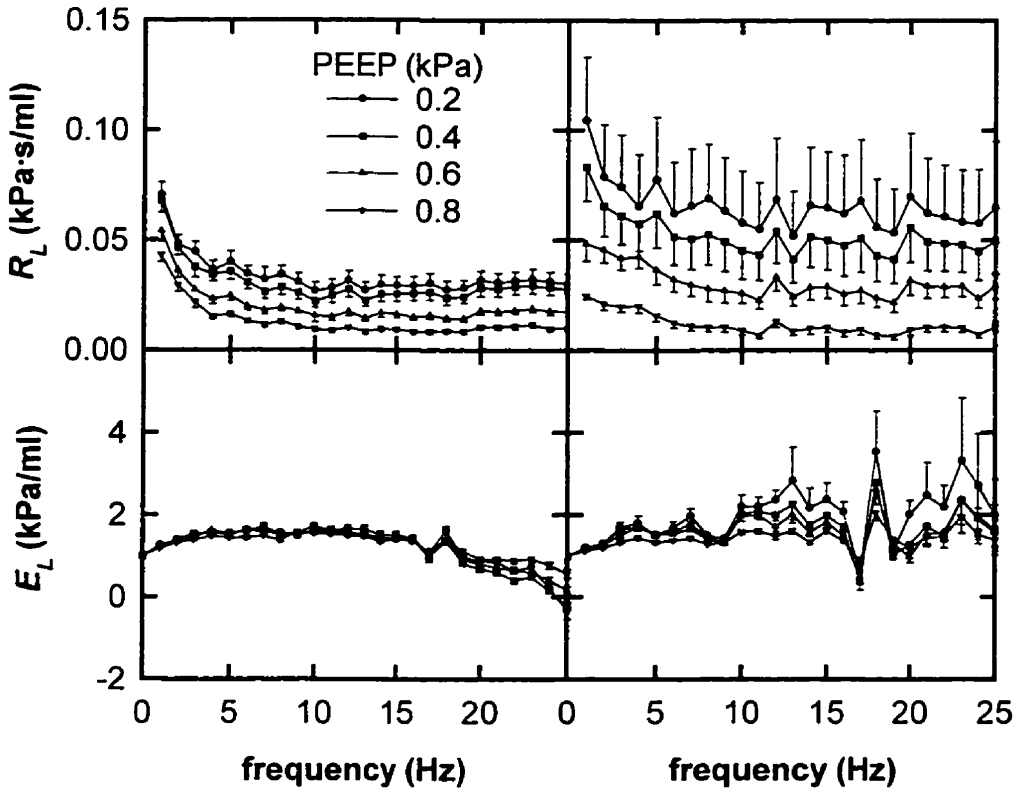


Figure 7-7. Dynamic linear block resistance ($R_L$ ) and elastance ($E_L$) of the Hammerstein model as a function of frequency for all rats from perturbation amplitudes of 1 ml (left panels) and 4 ml (right panels) for each PEEP. Bars indicate standard error.

Due to the static nonlinear gain of the nonlinear block, the data are not directly comparable to linear models. However, results for 1st order models (i.e. linear) were also calculated and were found to resemble scaled versions of the dynamic linear blocks shown in Figures 7-7. The linear model impedances were also far noisier in appearance, especially at the highest PEEPs and amplitudes.

### 7.3.5 Hammerstein nonlinear model blocks

As can be observed in Figure 7-5, for a given PEEP the various perturbations trace the same underlying nonlinear curve, but evoke a greater range with increasing perturbation amplitude (although in most of the animals there was a small shift to higher

pressures observed as the amplitude increased). Figure 7-8 shows the pooled results of the Hammerstein model 3rd order nonlinearities (mean ± standard error) for each PEEP level calculated from the 4 ml amplitude perturbations. At PEEP 0.2 and 0.4 kPa the nonlinearity is almost straight, indicating that a linear model likely suffices at this level of PEEP, agreeing with the results of Figure 7-6. At PEEPs of 0.6 kPa and particularly 0.8 kPa, the curves become increasingly nonlinear.

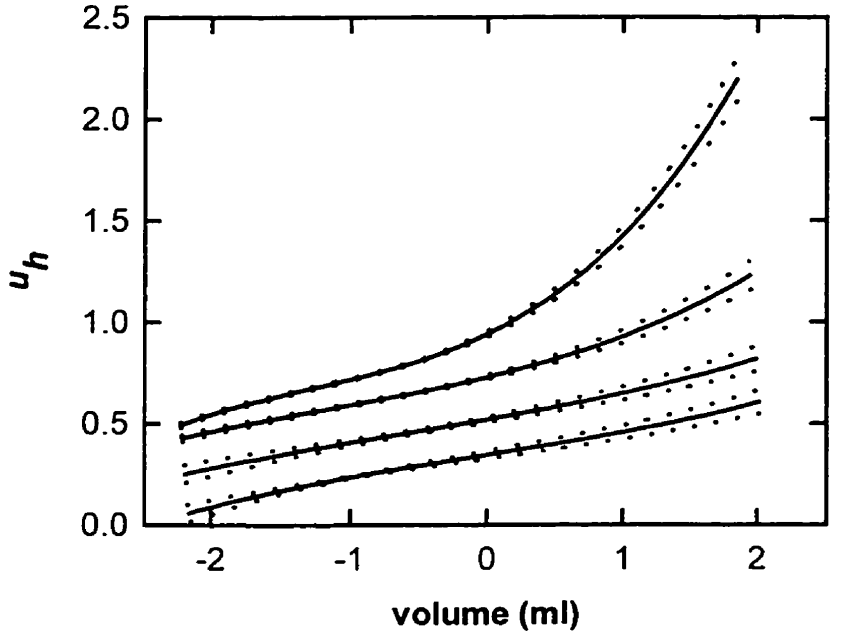


Figure 7-8. Pooled Hammerstein model nonlinear polynomials from all animals (solid lines) ± standard error (dotted lines) for PEEP levels of 0.2, 0.4, 0.6 and 0.8 kPa (bottom to top) obtained using perturbation amplitudes of 4 ml.

## 7.4 Discussion

In this study, we assessed the ability of the Wiener and Hammerstein structures to model rat lung mechanics *in vivo*. In particular, we were interested in separating dynamic linear and static nonlinear effects, so we used a nonparametric approach in order to minimise the number of *a priori* assumptions involved. We found that at the lower

amplitudes and lower PEEPs, Wiener or Hammerstein models performed similarly and did not fit the data any better than linear models. However, at the highest PEEPs, where the effects of nonlinearities were important, a Hammerstein model featuring a 3rd order nonlinearity and a one-sided impulse response function of 1 second duration provided the best fit to the data (Fig 7-6). Again as was the case in Chapter 6, this contrasts with the results of Suki et al. (160), who found that the Wiener model outperformed the Hammerstein model for the tissue block of their model. However the data are not directly comparable, for the differences may be due to the animal species used, the presence of an additional parallel pathway in their model, or the fact that the input to their model was flow rather than volume as in this study. However, there is the possibility that at the lowest PEEP of this study, which more closely matches the region of investigation of Suki et al. (160), the Wiener model may slightly better account for the rat mechanical behaviour (Fig. 7-6) in agreement with their finding, although the degree of nonlinearity at this PEEP is small.

### 7.4.1 Harmonic Distortion

As described in Chapter 6.3.1, the presence of nonlinearities in systems may cause harmonic distortion in estimates of linear system impedances (152). We investigated the performance of nonlinear models at reducing the effects of harmonic distortion by comparing the linear blocks of our Hammerstein or Wiener models to linear models identified from the same data. For those cases where the nonlinear models were not required, the nonlinear system identification process converged after a single iteration, and the linear block of the Wiener or Hammerstein model was identical to the linear model. However, where nonlinear effects were important (at the larger amplitudes and higher PEEPs) the $R_L$ and $E_L$ of the linear models were noisy, presumably due to harmonic distortion arising from static $PV$ nonlinearity (152). In contrast, the corresponding $R_L$ and $E_L$ of the linear blocks in the nonlinear models were much smoother, any remaining noise presumably being due either to noise in the measurements, or to additional nonlinear effects not accounted for by the Hammerstein

model. The fact that the RMSE is not zero indicates this as well (Fig. 7-4, 7-6). Of course we are assuming that the linear system block impedances should be smooth, which is supported by the fact that smaller amplitude perturbations produced less variance in $R_L$ and $E_L$ (Fig. 7-7).

### 7.4.2 Comparison with other results

The low frequency linear mechanical impedance of the rat lung has been measured by Peslin et al. (124), Hantos et al. (53) and Lutchen et al. (87). Each study used small amplitude perturbations and assumed linearity in their analyses. Peslin et al. (124) measured the mechanics of excised rat lungs subjected to sinusoidal forcing between 0.01 and 0.5 Hz. Although this was below the frequency range we used, they also found a hyperbolic frequency dependence of resistance, and a log-linear frequency dependence of elastance. Lutchen et al. (87) and Hantos et al. (53) used pseudo-random forced oscillations over a smaller frequency range (~ 0.25 - 12 Hz) to identify the impedance behaviour. Both these studies again found a hyperbolic frequency dependence of resistance, and log-linear elastance behaviour. To compare to these results, the Hammerstein models were refitted to the data, this time allowing the linear block gain to account for as much of the total static gain as possible. That is, exactly as for the nonlinear models applied to lung tissue (Chapter 6.3.5), instead of normalising the dynamic linear block to have unity dc gain, the coefficients of the nonlinear polynomials were normalised to the value of the first-order coefficient. Thus all linear characteristics of the model - including the linear term of the static zero memory block - are located in the linear block, and the remaining gain of the static nonlinearity is due only to the higher order coefficients. Figure 7-9 shows $R_L$ and $E_L$ calculated in this manner from the linear model compartment obtained using 1 ml amplitude perturbations at each PEEP. Over the corresponding frequency ranges, our $R_L$ values were about one half the values of Hantos et al. (53) and Lutchen et al. (87), while our $E_L$ values were one half those of Hantos et al. (53) and similar to those of Lutchen et al. (87). Differences in results are perhaps due to differences in animal strain. The inverse dependence of $R_L$ on the PEEP (Fig. 7-9)

matches that observed by Hantos et al. (53), and is still comparable to that in Figure 7-7. This inverse $R_L$ dependence on PEEP is to be expected because decreasing lung volume decreases airway dimensions, which leads to larger airway resistances. However, Figure 7-9 shows a bowl-like dependence of $E_L$ on the PEEP, i.e. a decrease in $E_L$ from PEEP 0.2 to 0.4 kPa, then an increase to PEEP 0.6 and 0.8 kPa. Increases in $E_L$ with PEEP has been reported in dogs (52,156) and in rats (53) while the bowl-like dependence of $E_L$ on PEEP has also been observed by Dechman et al. (26) in canine dog lungs.

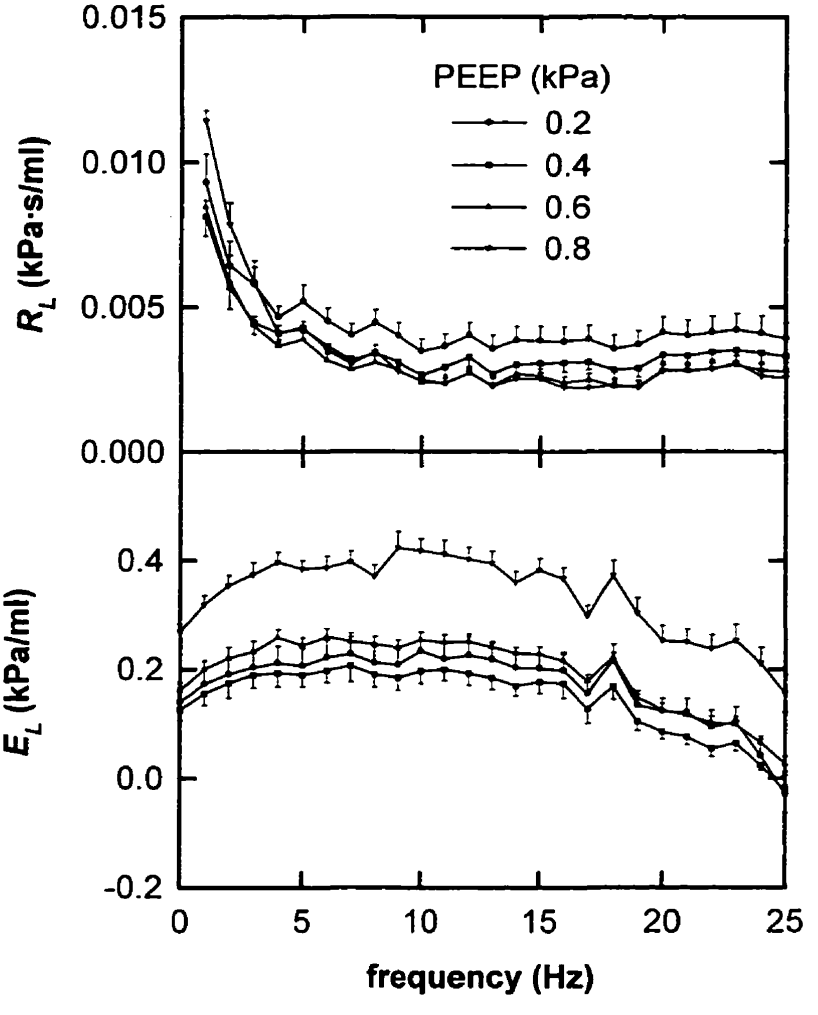


Figure 7-9. Mean Hammerstein dynamic linear block $R_L$ and $E_L$ from all animals obtained using 1 ml amplitude perturbations with the static nonlinear polynomials normalised to their 1st order coefficients. Bars indicate standard error.

Thus as in the nonlinear models of Chapter 6 applied to lung tissue, we can thus view the Hammerstein model of the lung in two ways: 1) with all the dc gain located in the static nonlinear block (i.e. with the gain at 0 Hz of the linear block normalised to unity), and 2) with all the gain located in the dynamic linear block (i.e. with the static nonlinearity normalised to the value of the first-order coefficient). Although the choice is arbitrary as far as the system input-output relationships are concerned, as was found in Chapter 6, we found that there is a compelling reason for assigning all the dc gain to the nonlinearity. This is demonstrated in Figure 7-10A, where we plot the Hammerstein model nonlinearities obtained from one of the rats with the quasi-static $PV$ loops obtained by slow sinusoidal cycling. The two sets of curves are largely coincident, suggesting that the non-normalised Hammerstein nonlinearity provides an estimate of the static $PV$ behaviour of the lung. In contrast, when the dc gain of the Hammerstein model is assigned to the dynamic linear block, the static nonlinearities are not vertically ordered with PEEP and so do not correspond to the static $PV$ behaviour (Fig. 7-10B). Interestingly, when all the dc gain is located in the static nonlinearity, much of the PEEP dependence of $E_L$ is eliminated (Fig. 7-7). This suggests that much of the observed dependence of elastance on PEEP reported by Hantos et al. (53) may be attributable to the static $PV$ nonlinearity. However, $R_L$ remains inversely dependent on PEEP regardless of the location of the gain (Figs. 7-7 and 7-9), indicating that this behaviour is not accounted for by the Hammerstein model.

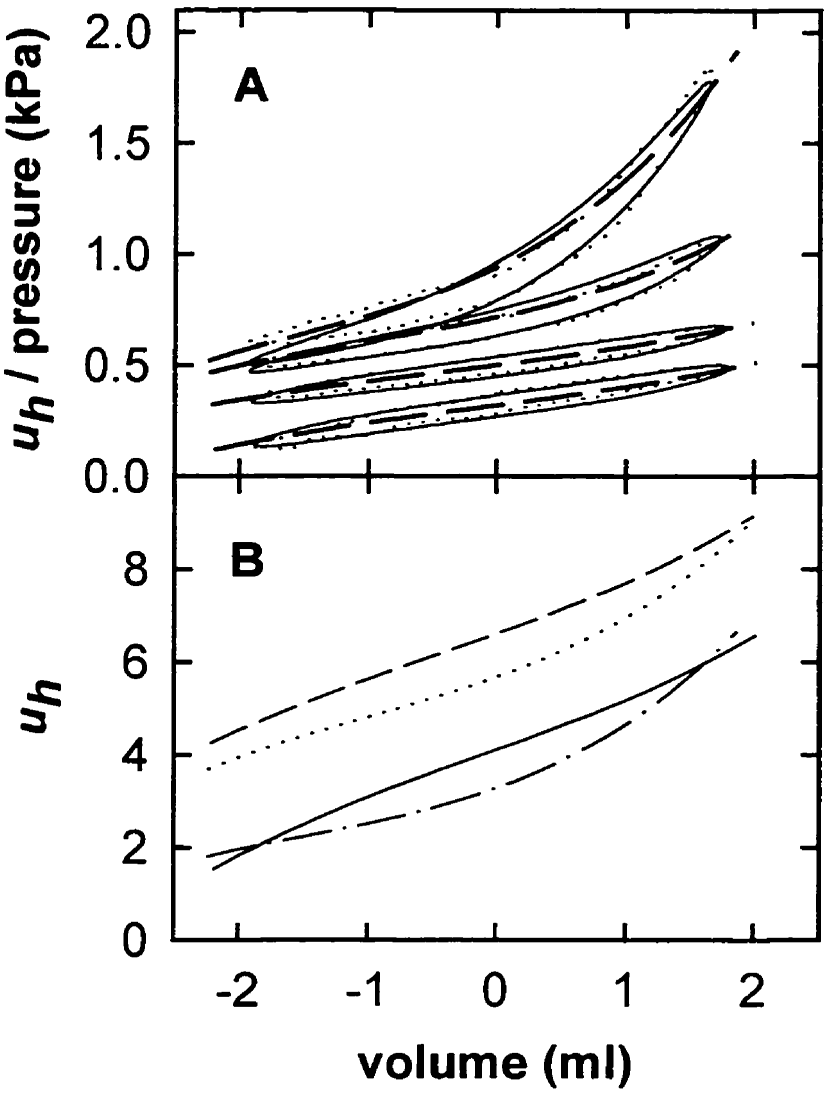


Figure 7-10. (A) Hammerstein static nonlinearities obtained with the dc coefficient of the dynamic linear block normalised to unity (dashed lines) from 4 ml volume perturbations in a single animal. Also shown are the *PV* loops obtained from quasi-static sinusoidal volume perturbations (0.25 Hz) of 4 ml amplitude (dotted lines) and the model output from the same sinusoidal inputs (solid lines). The results from bottom to top are in ascending levels of PEEP of 0.2, 0.4, 0.6 and 0.8 kPa. (B) Hammerstein nonlinearities from the same animal, normalised to the value of the 1st order coefficient (0.2 kPa solid, 0.4 kPa dashed, 0.6 kPa dotted and 0.8 kPa dash-dot).

Of course, the Hammerstein nonlinearities alone do not account perfectly for the measured quasi-static *PV* behaviour of the lung because the latter result in *PV* loops having finite area. However, by applying the same slow sinusoidal cycling to our model as was used to generate the quasi-static *PV* loops, we obtained simulated *PV* loops having similar areas (Fig. 7-10A), supporting the notion that the loop area observed experimentally is largely due to very low frequency system dynamics. Even so, at the highest PEEP the simulated *PV* loop systematically underestimated the experimentally observed loop at its low pressure end (Fig 7-10A). The reasons for this discrepancy are unknown, but presumably include effects not accounted for by the Hammerstein model such as plasticity (76,145). Although there was a consistent difference between the shapes of the predicted loops and the measured *PV* loops at the highest PEEP, there was no difference between the area circumscribed by the PV loops predicted by the Hammerstein model and the measured data. The underestimation of the loop area by the Hammerstein model was 0.8 ± 6.4 % (mean ± std. dev.). Apart from the discrepancy in shape at the highest PEEP level, this implies that the Hammerstein model at a given amplitude and PEEP can account for all dissipation during slow sinusoidal cycling. Since the Hammerstein model is a subset of models describable via the Volterra series it may be concluded that there is no evidence from this data for plasticity in the mechanics of the rat lung. This is because the Volterra series which includes all Hammerstein models cannot account for plastic behaviour, i.e. systems with infinite memory. This may resolve the question raised in Chapter 6, which could only provide an upper bounds on the amount of plasticity for sinusoidally perturbed lung tissue strips. However, some caution must be exercised regarding this assertion, since not all behaviour exhibited by the system was accounted for by the Hammerstein model, and as in the lung tissue results, some dynamics may exist below 1 Hz which can not be estimated with the IRF length (1 sec) used in the identification process. Although plasticity could not be discerned with this data, this does not rule out the possibility. The sinusoidal perturbations were at 0.25 Hz, which may not have been sufficiently slow to discern non-viscoelastic dissipation. Also, although the Volterra series cannot model plastic phenomena in the strictest sense, given

enough degrees of freedom it may be possible to approximate some plastic behaviour, although this is mere supposition and requires further investigation.

## 7.5 Summary

We have used nonparametric Wiener and Hammerstein models to describe rat lung mechanics. At low PEEP there was little difference between either model, and a linear model performed just as well. However, at the higher PEEP levels the Hammerstein model fit the data best. The shape of the dynamic linear block impedance of the Hammerstein model matched previous estimates of lung impedance obtained using small amplitude flow perturbations (53,87,124). Furthermore, the static nonlinearity of the Hammerstein model corresponded closely with the experimentally measured quasi-static *PV* behaviour of the rat lung, provided that the total dc gain of the Hammerstein model was located in the static nonlinearity. This also eliminated much of the PEEP dependence of the linear block elastance. However, a dependence of the linear block resistance on PEEP remained, indicating the presence of mechanical behaviour in the lung not accounted for by the Hammerstein model. The model was able to predict the response to slow sinusoidal cycling with significant discrepancies occurring only at the highest PEEP. Furthermore, no evidence of plastic dissipation was detected during slow sinusoidal cycling.

# 8. Distributed modelling of lung tissue viscoelasticity

## 8.1 Introduction

### 8.1.1 The complex dynamics of the lung tissue strip

With Dr. Daniel Navajas I measured the dynamic viscoelastic behaviour of dog lung tissue using both step changes and oscillatory perturbations in strain as briefly described in Chapter 6.1. We showed that the stress relaxation response to a step change in strain can be well-described by a linear decrease with the logarithm of time. The same relation describes the stress response to step changes in volume of cat lungs (Eq. 2-3) (58). We also measured the response to sinusoidal perturbations at several frequencies, and showed that the tissue resistance is well-modelled by a hyperbolic power law function of the frequency (Eq. 6-2).

Figure 8-1 shows the stress relaxation response from a lung tissue strip subjected to step changes in strain of 0.1 at three different operating stresses, with the curve fits according to the function

$$\sigma - \sigma_0 = Ct^{-\beta}, \tag{8-1}$$

where $C$ and $\beta$ are constants and $\sigma_0$ is stress prior to the step in strain as in Eq. 2-17 Chapter 2.2.3. This expression is similar to Eq. 2-3 since

$$\begin{aligned} t^{-\beta} &= \exp(-\beta \ln(t)) \\ &= 1 - \beta \ln(t) + \beta^2 \ln(t)/2! - \cdots + (-1)^n \beta^n \ln(t)^n/n! + \cdots \\ &\approx 1 - \beta \ln(t) \end{aligned}, \tag{8-2}$$

provided that the exponent $\beta$ is small (12). The results from fitting all five tissue strips are shown in Table 8-1. It is clear that $\beta$ is almost completely independent of amplitude, despite the dependence of $C$ on $\sigma_0$.

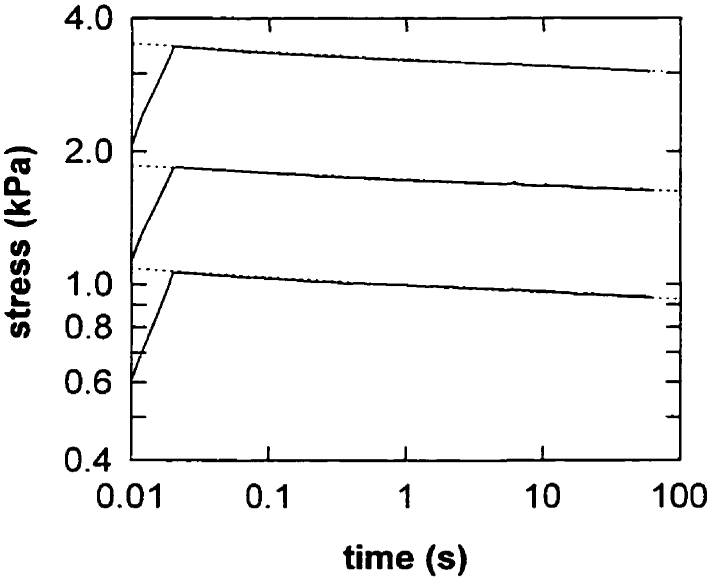


Figure 8-1. Three stress recovery curves (solid) obtained from a tissue strip subjected to 10% stretch from three different operating stresses, with curve fits according to Eq. 8-1 (dotted). The slanting upward portions of the lines from t = 0.01 sec are drawn to indicate the initial stresses prior to the step.

| $\sigma_0$ (kPa) | $C$ (kPa) | $\beta$ | RMS residual (kPa $\times 10^{-3}$) |
|---|---|---|---|
| 0.6 | 0.42 ± 0.05 | 0.044 ± 0.005 | 5.2 ± 3.5 |
| 1.1 | 0.60 ± 0.05 | 0.045 ± 0.004 | 3.8 ± 1.7 |
| 2.1 | 1.25 ± 0.22 | 0.046 ± 0.006 | 4.9 ± 2.0 |

Table 8-1. The values of $C$ and $\beta$ (Eq. 8-1) are means ± std. dev. from five lung tissue strips, each from a different dog.

The magnitude of the impedance of lung tissue $Z(f) = \sigma(f)/\dot{\varepsilon}(f)$ obtained with sinusoidal perturbations also follows an inverse power law. Figure 8-2 shows the mean tissue impedance measured from all tissue strips obtained with sinusoidal oscillations of 0.1 peak-to-peak amplitude. The impedance is almost perfectly proportional to $f^{-\alpha}$ where $\alpha = 0.959$. In fact, this value for $\alpha$ is very close to the value predicted from the Fourier transform of Eq. 8-1 (12), which gives $\alpha = 1 - \beta = 0.955$. Thus, both the stress relaxation and impedance of lung tissue strips show dynamics that follow power law functions. If we consider the impedance of the whole lung, which is also describable using power laws (Chapter 2.2.3, Eqs. 2-5 to 2-7), the above implies that for a white noise flow input signal, the resulting pressure signal will be distributed with a power spectral density proportional to $1/f^{2\alpha}$. For $0 < \alpha < 1$ this falls within the definition of $1/f$ noise (71).

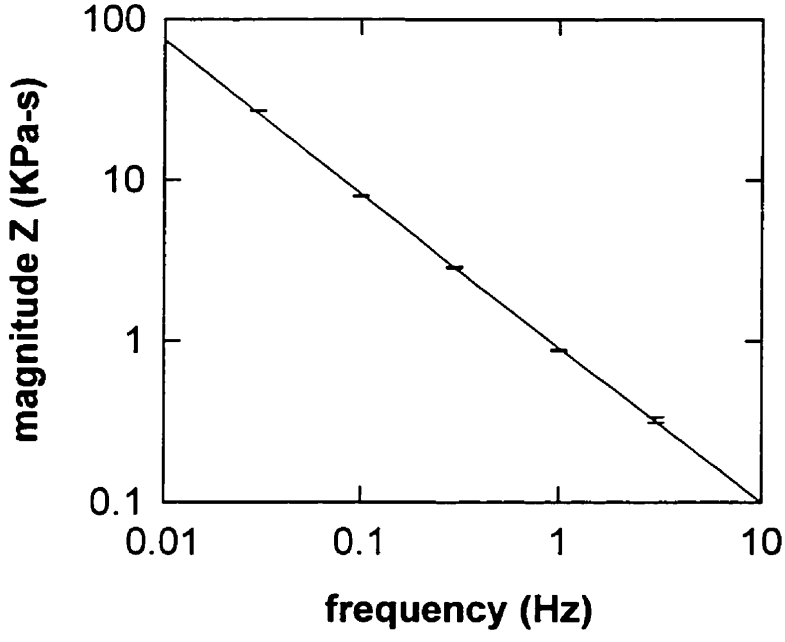


Figure 8-2. Impedance of lung tissue strips obtained using sinusoidal perturbations of 0.1 strain amplitude (peak-to-peak) at an operating stress of 1.1 kPa. Points are mean ± standard deviation and the line is the best fit to the data.

There are innumerable processes in nature which exhibit $1/f$ power spectral densities. Examples include the intensity and frequency of occurrence of earthquakes (4), economic data (96), and even the loudness and pitch of music (168). The ubiquity of $1/f$ processes has led to the speculation that $1/f$ noise reflects "some profound law of nature that applies to all nonequilibrium systems" (71) and that "$1/f$ noise is the consequence of a system being complex irrespective of the context" (171). In Bates et al. (12) we likewise took the view that the above behaviour was a result of the intrinsic complexity of lung tissue.

An explanation for the origin of $1/f$ processes has been postulated recently via the phenomenon called self-organised criticality (SOC) (5,20). Systems which display SOC consist of many interconnected components which can exchange energy only with their nearest neighbours. Each component can absorb energy up to a limit, after which it spills out and contributes to the energy of its neighbours. This may cause some of the neighbours to exceed their energy limits, producing a cascade of energy transfers. Such systems have been shown to naturally organise themselves spatially and temporally according to power laws (20), resulting in dynamics characterised by $1/f$ noise. In Bates et al. (12) we postulated that the dissipation of energy within the tissue was a result of the complex interconnectedness of its components. Many components of lung tissue are in intimate contact with each other, and under stress transmit the load through their contact points. A yield event at a given contact site may result in a cascade of yields in the vicinity leading to SOC within the tissue. We argued that the probability of a such a cascade is given by the product of the individual yield events, leading to the lognormal probability distribution. This is a logarithmic equivalent of the central limit theorem for the Gaussian distribution which results from the summation of many different probabilities. The viscoelastic nature of lung tissue is thus a result of the complex manner in which the individual components interact. However, for this to be physically realised, there must exist at some level within the lung tissue a nonlinear interaction that might lead to such energy cascades. I therefore wondered whether the nonlinear recruitment mechanism between the elastin and collagen fibres developed in Chapter 3 could be such a mechanism.

In Chapter 3, I developed a model for the elastic behaviour of lung tissue based on the fundamental stress-bearing constituents, the elastin and collagen fibres. The foundation for this model was a highly nonlinear interaction between the collagen and elastin fibres, thus providing a possible source for complex processes which could in principle give rise to $1/f$ tissue dynamics. Indeed, the correct nonlinear stress-strain curve was reproduced only if the constituent properties of the elements were distributed in a power-law sense. This distribution is reminiscent of the hyperbolic distribution of time constants which, if used in the linear viscoelastic model of Hildebrandt (58), can describe the stress relaxation of lung tissue (Eq. 2-3). It is thus interesting to consider that the origin for this distribution of time constants may be due to the power law distribution of the elastic properties alone, and that dissipation may be uniform throughout the tissue. Although the primary focus of this thesis has been on the static mechanics of lung tissue, in this chapter I consider the possibility of merging the dynamic and elastic behaviours of lung tissue via the introduction of simple linear viscous dissipation into the models of Chapter 3.

## 8.2 Spring-string-dashpot models

### 8.2.1 Viscous dissipation in series with spring-string pairs

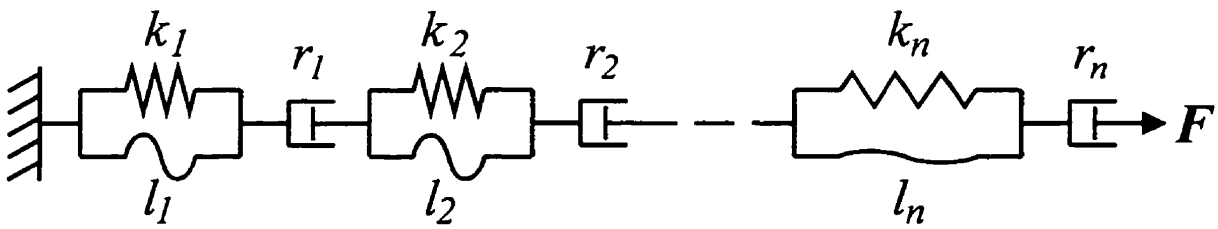


Figure 8-3. Elastic tissue model with dashpots interleaved in series with spring-string pairs. In this arrangement the dashpots can be lumped into a single equivalent dashpot.

Consider the model of Figure 8-3 which consists of a series of spring-string pairs interleaved with dashpots. Since all the dashpots share the same load, they can be lumped together into a single equivalent dashpot, $D_{eq}$, as

$$1/D_{eq} = \sum_{i}^{n} 1/r_i \ . \tag{8-3}$$

Following a step change in length, the instantaneous elastic response of this structure is governed completely by the spring-string components. Furthermore, a portion of these spring-string pairs are stopped (i.e. their respective strings are straight), while the remainder of the springs are below their stop lengths. The initial relaxation process begins according to the simple relaxation equation

$$F = F_o e^{-t/\tau_{eq}} , \tag{8-4}$$

where $F_o$ is the instantaneous elastic recoil force and $\tau_{eq}$ is the time constant of the model, defined by

$$\tau_{eq} = D_{eq} / K_{eq} , \tag{8-5}$$

where $K_{eq}$ is the stiffness of the model. Since the stiffness of the tissue changes with time as the spring-string pairs become progressively unstopped, $\tau_{eq}$ is thus a function of time.

***Series dissipation in the distributed stop length model (model A1)***

If we consider the case where the stop lengths are distributed and each spring is identical ($k_i = k$), then from Eqs. 3-3 and 3-5 we rewrite Eq. 8-5 as

$$\tau_{A1} = \frac{D_{eq}}{k} \int_{l_o}^{\infty} N(l) dl . \tag{8-6}$$

Using the $N(l)$ of Eq. 3-18 which was derived from the stress-strain curves of lung tissue strips, we have

$$\tau_{A1} = \frac{D_{eq}}{k} \left[ \frac{L_r H}{l_o + G A_r / k} \right] . \tag{8-7}$$

Since the force in the unit that has just become unstopped is $F = kl_o$, we can substitute Eq. 8-7 in Eq. 8-4 to obtain the stress relaxation response for model A1, thus

$$F = F_o \exp\left(\frac{-t(F + GA_r)}{D_{eq} L_r H}\right) . \tag{8-8}$$

This expression is an implicit equation in $F$, and can be solved numerically.

***Series dissipation in the distributed stiffness model (model A2)***

If now we consider distributing the stiffnesses while keeping each of the stop lengths identical ($l_i = l$), then from Eq. 3-10 in Eq. 8-5 we have

$$\tau_{A2} = D_{eq} \int_{k_0}^{\infty} \frac{M(k)}{k} dk . \tag{8-9}$$

Similarly to model A1, we use the stiffness distribution derived from the stress-strain curve to obtain

$$\tau_{A2} = D_{eq} \left[\frac{L_r H / l}{k_o + GA_r / l}\right] . \tag{8-10}$$

Substituting $k_o = F/l$ into Eq. 8-10 gives exactly the same stress relaxation time constant as in Eq. 8-8. This agreement between the two relaxation functions is predictable, since in this model dissipation is completely independent of the stress-strain relation, which is the same for either model A1 or A2. Thus even if we distributed both $l$ and $k$ simultaneously, the same stress-relaxation behaviour would result, provided the model accounted for the same static stress-strain curve.

***Response of the series dissipation model (models A1 and A2)***

The implicit equation that describes the relaxation function (Eq.8-8) was solved by root finding using the bisection method (18). Briefly, upper and lower guesses for $F$ which bound the true $F$ were made, and the expression was evaluated at both bounds. If the result was closer to the upper bound, the lower bound was adjusted to the halfway point and the procedure repeated until the desired convergence was achieved (0.01% here). The method is simple and guarantees convergence, unlike Gauss-Newton strategies

(18). The values for the parameters $A_r$, $L_r$, and $H$ were taken from the mean tissue strip data (Table 3-1), while $D_{eq}$ was arbitrarily assigned the value 1000 N·s/m. Figure 8-4 shows the results compared with the stress relaxation of a single time constant model, where the time constant is equivalent to $\tau_{A1}$ at $t = 0$ sec. The results show that the spring-string model A1 relaxes at a slower rate than the single time constant model, and is therefore closer to the observed experimental behaviour, although it does not produce a linear log-log plot of stress relaxation as in Fig. 8-1.

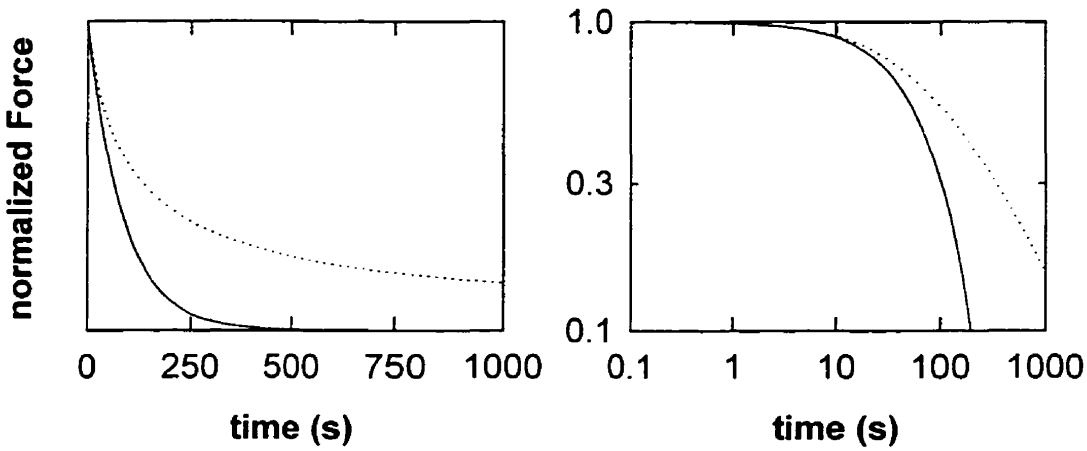


Figure 8-4. Left panel: stress response of model A1 (solid) to unit step input, compared with the response of a single time constant model (dotted), with time constant equal to $\tau_{A1}$ at $t = 0$. The right panel shows the response in log-log space.

### 8.2.2 Viscous dissipation within the spring-string pairs

Consider the model of Figure 8-5, where within each spring-string pair a dashpot is located in series with the spring. This model is considerably more complex than the previous model because recruitment and derecruitment of fibres may affect the rate of stress-relaxation, and so the dashpots cannot be considered as effectively being a single element. Thus not only are distributed spring and string properties possible, but the

dashpot resistances may be distributed as well. However, I consider only that the elastic properties are distributed, and that the viscous properties are identical for all elements.

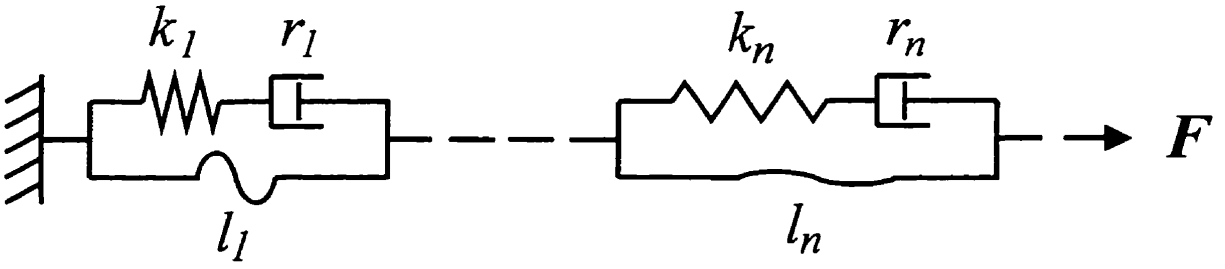


Figure 8-5. Elastic tissue model including dashpots in series with each spring.

***Distributed stop lengths with identical stiffnesses and resistances (model B1)***

If the stop-lengths of the model are distributed, with $k_i = k$ and $r_i = r$ for all $i$, then the units which are unstopped can be lumped together into an equivalent dashpot and spring. The time constant of the unstopped units is then simply

$$\tau_{B1} = \frac{1/k \int_{l_o}^{\infty} N(l)dl}{1/r \int_{l_o}^{\infty} N(l)dl} = r/k \quad , \tag{8-11}$$

which is identical to a single Maxwell element. Within a stopped unit the force is shared between the Maxwell element and the string. However, the rate of relaxation is the same as for the unstopped elements (Fig. 8-6), since all time constants are identical. Another way to view this is that, as the dashpot within a unit relaxes, the force at which that unit becomes stopped, $F_s$, decreases as well. This is because the movement of the dashpot is equivalent to increasing the relaxed length of the spring. Therefore, the force in the entire model never decreases to the level where a unit can become unstopped (Fig. 8-6). This model is thus independent of fibre recruitment-derecruitment and its dynamics are equivalent to a single time constant Maxwell element.

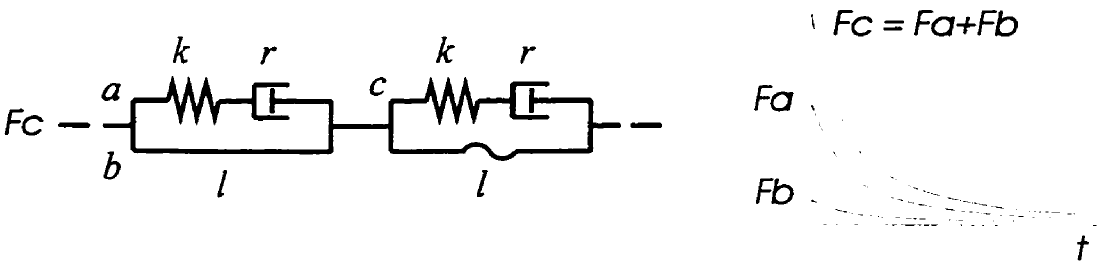


Figure 8-6. Schematic of model featuring a stopped unit (left) and unstopped unit (right) with relaxation functions in each path: spring-dashpot stopped unit ($F_a$), string stopped unit ($F_b$), and spring-dashpot unstopped unit ($F_c$). The stopped units never become unstopped, since the force is decreasing within each unit at the same rate.

***Distributed stiffnesses with identical stop-lengths and resistances (model B2)***

If the static elastic properties of the tissue are derived from the distribution of spring constants, then the behaviour of the model is considerably more complex. However, like model B1, the time constant is determined from the unstopped springs and dashpots as,

$$\tau_{B2} = \frac{\int_{k_o}^{\infty} \frac{M(k)}{k} dk}{1/r \int_{k_o}^{\infty} M(k) dk}. \tag{8-12}$$

The force in the model is given by that unit that is just at its stop length as $F = k_o l$, and it declines as $k_o$ changes with time, similar to models A1 and A2. Using the $M(k)$ from Eq. 3-21 derived from the stress-strain curves of lung tissue strips, we can solve for the equivalent time constant of the model, $\tau_{B2}$. However, the integral in the denominator to because of its infinite upper limit is not finite. We thus fix an upper limit for the stiffness distribution as was done in Chapter 3. Evaluating the denominator thus gives

$$\tau_{B2} = \frac{r(k_f - k_o)}{\ln\left(\frac{k_f + J}{k_o + J}\right) + \frac{J(k_o - k_f)}{(k_f + J)(k_o + J)}}, \tag{8-13}$$

where

$$J = GA_r/l, \tag{8-14}$$

and we have defined $l$ as in Eq. 3-22, $k_f$ as in Eq. 3-25 and $G$ and $A_r$ from the mean tissue strip properties (Table 3-1). The value for $r = 1.78\text{x}10^7$ was chosen so that $\tau_{B2} = \tau_{A1}$ at t = 0. Substituting $l = F/k_o$ into Eq. 8-13 we have the stress relaxation function for model B2 as

$$F = F_o e^{-t/\tau_{B2}} \tag{8-15}$$

where like models A1 and A2, this is an implicit function in $F$ and must be solved numerically.

***Response of the series dissipation model (model B2)***

The solution technique for model B2 is identical to that of models A1 and A2, using the bisection method for root finding (18). The results are shown in Figure 8-7, and are very similar to those of Model A1 and A2 (Fig. 8-4). The model has slower stress relaxation than a single time constant model, but again does not match experimental behaviour since the stress relaxation does not produce a linear log-log plot.

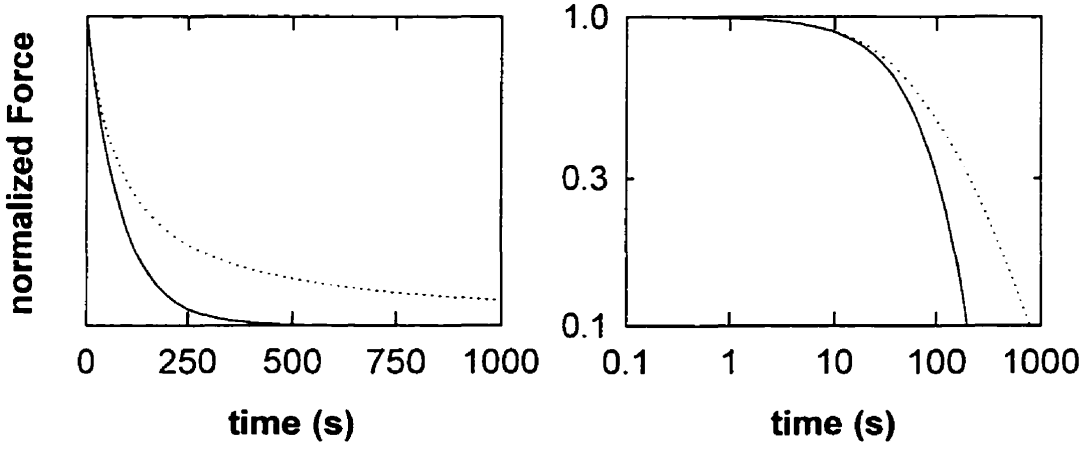


Figure 8-7. Left panel: stress response of model B2 (solid) to unit step input, compared with the response of a single time constant model (dotted), with time constant equal to $\tau_{B1}$ at $t = 0$ (and equal to $\tau_{A1}$ at $t = 0$). The right panel shows the response in log-log space.

## 8.3 Discussion

None of the models incorporating a single Newtonian resistance were able to accurately account for the dynamic behaviour of lung tissue. Each of these models relied on the recruitment-derecruitment of fibre properties to mimic the $t^{-\beta}$ stress-relaxation of lung tissue, and thus attempted to utilise the spatially distributed properties of the elastin-collagen fibres as a single mechanism for both static elastic and dynamic behaviour. Since no suitable candidates were found, it is likely that the origin of tissue viscoelasticity arises from a mechanism distinct from the recruitment of collagen fibres that leads to the static-elastic stress-strain properties. There is also considerable doubt that recruitment mechanisms are linked to the $t^{-\beta}$ behaviour of lung tissue, since $t^{-\beta}$ can also describe the stress relaxation of natural rubbers and polymers (32,92,131). So whatever mechanisms are responsible for this behaviour, they must be general and ubiquitous. We must also not forget the results of Chapter 6 which showed that the nonlinear static behaviour and linear dynamic behaviour could be accurately accounted for in separate blocks by a Hammerstein model. Thus the mechanisms for the static nonlinear elastic properties appear to be distinct from those that give rise to the dynamic properties. Indeed, Lanir (81) has shown that for collagenous tissues, a fibre recruitment model is compatible with the quasilinear theory of viscoelasticity which is equivalent to a Hammerstein model (Chapter 2.3.3). This compatibility was not expected to hold for tissues with more than one fibre type with two independent rates of recruitment. However, the recruitment he considered was that of wavy collagen becoming taut and thereafter extending linearly with the applied force. The tissue thus stiffens as a result of the accumulation of collagen fibre stiffnesses in parallel. Instead of collagen as the extensible fibre, my model relies on the removal of elastin fibres in series as the collagen fibres take up the load. Although the recruitment behaviour is different, and the model contains two fibre types, there is only one rate of fibre recruitment. Thus, as Lanir showed for collagenous tissues, it may be possible that the model presented here is compatible with the Hammerstein model, as the results of Chapters 3 and 6 suggest. If this is true, this adds to the body of evidence in this

thesis that the recruitment of fibres leading to static elastic behaviour is independent of the processes responsible for the dynamic behaviour.

If the static mechanical behaviour of lung tissue arises from the mechanism of fibre recruitment, the question then remains then as to the mechanism for the dynamic behaviour. Mechanisms have been proposed that arise from the plastic and viscous sliding actions between fibres in intimate contact (107), or viscoelastic fibre behaviour akin to that of branched polymer chains (154). Each of these mechanisms may be present, and may even be complemented by further interactions within the lung tissue. However, $1/f^{\alpha}$ noise and $t^{-\beta}$ behaviour of the lung tissue need not arise from any mechanism in particular, if the lung behaves as a complex system. All that may be required is that the interactions within the lung tissue be sufficiently rich and varied, and exchange energy amongst its parts in a nonlinear fashion (4,12,20). Thus it may be argued that the origin of dynamic viscoelasticity arises from the ensemble behaviour of the many components within the parenchyma, and is a consequence of the lung tissue being a complex dynamic system.

## 8.4 Summary

In this chapter I explored the possibility that the dynamic behaviour of lung tissue might arise from the power law distribution of its constituent properties, using the recruitment models of Chapter 3. I showed that lung tissue stress-relaxation behaviour could not be accounted for by introducing linear resistances interleaved in series with each spring-string pair. Similarly including linear resistances in series with each spring in the spring-string pair could not account for the experimentally observed $t^{-\beta}$ stress relaxation. Dynamic properties thus could not be linked with the mechanics of fibre recruitment responsible for the static nonlinear behaviour. In Chapter 6, I showed that a Hammerstein model which separates dynamic mechanics and static mechanics in different blocks accounted for essentially all the mechanical response. Thus the nonlinear

static mechanics most likely arise from distinct mechanisms from those responsible for the dynamics. Indeed, the static nonlinear stress-strain curve may be best described via fibre recruitment, while the $t^{-\beta}$ relaxation and $1/f$ impedance behaviour may arise from the lung tissue being a complex dynamic system with many nonlinearly interacting components.

# 9. Conclusions

In this thesis, I have applied two different modelling approaches to the study of lung tissue mechanics. The static behaviour of lung tissue was modelled using *a priori* information concerning its fundamental structural elements, the collagen and elastin fibres. The combined static mechanical and dynamic behaviour was modelled using non-parametric block structured nonlinear models which make no assumptions as to the source of the behaviour.

The nonlinear elastic behaviour of the lung tissue strip was modelled by assuming that the collagen fibre lengths or the elastin fibre stiffnesses were distributed within the lung tissue. The model considered that tissue was composed of linearly elastic elastin fibres in parallel with initially wavy collagen fibres which straighten progressively with extension. Fitting of the analytical models to stress-strain measurements of dog lung tissue strips revealed that either collagen fibre lengths or elastin stiffnesses or both were distributed according to inverse power laws. Collagen fibres were distributed as squared power laws and elastin fibre stiffnesses were hyperbolically distributed for over greater than 95% of their ranges. This implies that the lengths and stiffnesses of the fibres are spatially organised in a fractal-like manner. The stiffness distributions led to elastin fibre diameter distributions which were in very good agreement with the morphometric data of Sobin et al. (142) and the collagen length distributions agreed qualitatively with their collagen curvature distributions. Computer simulations of two-dimensional tissue strips showed that hyperbolically distributed collagen fibre lengths predicted the stress-strain curves of the tissue strips. The difference from the analytical model in the exponent of the power law distribution of collagen fibre lengths was attributed to geometrical effects in the two-dimensional simulation. These simulations also illustrated the gradual recruitment of collagen fibres, showing the development of spatial and stress distribution heterogeneity with uniaxial stretch.

Insofar as the tissue plays an important role in the generation of the $PV$ curve, the model provided a mechanistic basis for its nonlinear shape, and quantitatively defined how the elastin and collagen networks may be altered in lung tissue disease. Changes in the model parameters from normal to emphysematous and fibrotic lungs were in qualitative agreement with the current understanding of the structural changes that occur in these diseases. Changes in the elastin and collagen fibre network properties were found to be reflected in changes in the shape factor $K$ of the expression $V = A - B\exp(-KP)$ commonly used for the $PV$ curve. Changes in the collagen network were found to be reflected in the parameter $B$. Changes in the elastin properties dominated the changes in collagen properties in both emphysema and fibrosis. This was attributed to the proportional manner in which elastin may contribute to the elastic recoil, while changes in the collagen network may only alter lung distension probabalistically.

The dynamic and static mechanical behaviours of the lung tissue strip were extremely well-described by a static nonlinear block in series with a linear dynamic block together comprising the Hammerstein model. This model accounted for more than 99% of the stress resulting from broadband pseudo-random perturbation of the strain, and was invariant to changes in input amplitude and operating stress level. The model was also able to extract the static nonlinear behaviour from the dynamic linear behaviour, which was similar to that obtained from small amplitude inputs. The Wiener model also accounted for much of the observed behaviour as did a parallel combination of a static nonlinear block and linear dynamic block. However, each was slightly inferior to the Hammerstein model, as they were not consistent for changes in strain amplitude and operating stress. The amount of plastic dissipation within the lung tissue strip was estimated at less than 20%. The Hammerstein model was also found to be the best of the block structured models at describing the rat lung *in vivo*. However, additional dependence of the linear dynamic block resistance on operating pressure and input amplitude indicated that a more complicated mode is required to describe the mechanics of the whole lung.

It was found that it was not possible to account for the dynamic behaviour of the lung tissue by including linear resistances within the nonlinear static elastic fibre recruitment model. It was concluded that the mechanisms leading to the inverse power law stress relaxation and inverse power law dependence of the impedance on frequency arise from distinct processes independent of fibre recruitment. This is in agreement with ability of the Hammerstein model to separate the static elastic behaviour from the linear dynamic behaviour.

## 9.1 Statement of original contributions

(1) An analytical model for the stress-strain curve of lung tissue strips based on the properties of collagen and elastin fibres was introduced. The distributions of the fibre properties were derived without assumptions being made as to their functional forms. The model provides a mechanistic basis for the well-accepted idea that the elastin fibres are responsible for the elastic properties at small strains, but that the collagen fibres are gradually recruited throughout the measurement range and limit the maximum extension.

(2) The model was found to predict collagen fibre lengths and elastin fibre stiffnesses that followed inverse power laws, for over 95% of their ranges. This is suggestive of a fractal-like organisation of the fibre properties.

(3) A two-dimensional finite element computer simulation of lung tissue was developed. It was found that inverse power law distributed properties in this model can also describe the nonlinear stress strain curve. The model illustrated the gradual recruitment of collagen fibres causing the development of geometric and stress distribution heterogeneity.

(4) The one-dimensional fibre recruitment model was extended to describe the $PV$ curve of the lung. The model predicted changes in collagen and elastin fibre properties that are in agreement with the nature of emphysema and fibrosis. This provides a tissue based mechanistic explanation for the shape factor $K$ and the

parameter $B$ in the equation $V = A - B\exp(-KP)$ that is commonly used to describe the $PV$ curve. $K$ reflects both the collagen and elastin fibre networks while $B$ reflects the maximum distension of the collagen fibres.

(5) Very large amplitude broad-band mechanics of the lung tissue strip were measured for the first time at several different operating stresses and strain amplitudes over the entire physiologic amplitude range between 0.125 and 12.5 Hz.

(6) Large amplitude and broadband mechanics of the rat lung were measured for the first time at several different operating pressures and volume amplitudes over much of the physiologic range between 0.25 and 25 Hz.

(7) Nonparametric forms for the Wiener and Hammerstein models were applied for the first time to describe the mechanical properties of lung tissue strips *in vitro* and rat lungs *in vivo*. By using these models to predict the dissipation of energy during slow sinusoidal cycling, the estimated amount of plastic dissipation within the lung tissue was reduced from about 30% to less than 20%.

(8) The Hammerstein model was found to account for essentially all the mechanical response to broadband perturbations of the uniaxially stretched tissue strip, and was found to be slightly superior to the Wiener model in this regard.

(9) A parallel combination of a static nonlinear block and linear dynamic block was introduced as a possible model for lung tissue mechanics. Although this model accounted for most of the behaviour, it was found to be inferior to the Hammerstein model.

(10) The Hammerstein model was shown to be a better description of rat lung mechanics *in vivo* than the Wiener model. However, dependence of the linear block resistance on the operating stress of both Wiener and Hammerstein models indicated that a more complex model is required.

(11) Fibre recruitment models of lung tissue incorporating linear viscous dissipation were investigated. These models were found not to be able to reproduce experimentally observed mechanical behaviour. This reinforces the notion that the

dynamic behaviour of lung tissue arises from mechanisms distinct from fibre recruitment.

## 9.2 Suggestions for future research

### 9.2.1 Dynamic and static mechanics of tissue strips exposed to proteases

The models of Chapters 3 and Chapter 4 were based on stress-strain curves of normal dog lung tissue strips subjected to uniaxial strain. These models were based on the different properties of the collagen fibres and how the constituents are arranged. Studies which have used proteolytic enzymes such as collagenase and elastase have found that the quasi-static stress-strain curves of the lung tissue strips are altered in a manner consistent with these models (70, 134). However only limited studies on the dynamic properties have been performed (110) on strips exposed to enzymes. These studies found that with the administration of elastase caused both that $R$, $E$ and tension to decrease. It would thus appear that at least a portion of the dynamics arises from the elastin fibre network properties. It may also be possible to selectively damage the different fibre types using irradiation to damage those fibres with a higher molecular weight. However, it is unclear how the changes in the static elastic properties influenced the changes in dynamics. The Hammerstein model of Chapter 6 is particularly well suited to answering this question since it is capable of separating the static elastic behaviour from the dynamic behaviour. It would thus be interesting to apply the identification of nonlinear block structured models to tissue strips treated with various proteases.

### 9.2.2 Multiple path block structured models

The origin of the dependence of the linear block resistance of the Hammerstein model on the operating stress (Chapter 8) is unknown. It is thought that this may

represent linear or nonlinear airway properties which were not accounted for by the simple block structured model. In Westwick (173), techniques were developed for the nonparametric identification of nonlinear block structured models consisting of multiple Wiener paths, or models with mixed Hammerstein and Wiener paths. The addition of a second block structured model in parallel to the models of Chapter 7 may account for the observed dependence of the linear system block on operating stress, and is thus worthy of investigation. This may prove difficult since there was very little remaining variance not accounted for by the models. It may be possible to increase the portion of the variance accounted for by the dynamics by increasing the mid-range frequencies relative to the lower frequencies, which may reveal more of the additional system behaviour. However, depending on the form of any additional model path, it may or may not lead to any physiologically meaningful insights as to the origin of the observed PEEP dependence.

### 9.2.3 Measurements of human emphysematous and fibrotic lung tissue

In Chapter 5 a model was described for the *PV* curve of the lung curve based on the properties of collagen and elastin fibres. When the model was applied to the *PV* curves of emphysematous and fibrotic lungs, the changes in the model parameters were consistent with the changes observed in the tissue with these diseases. However, it is uncertain to what extent surface tension effects lead to this behaviour. One possible method to attempt to resolve this issue may be to apply the model to the stress-strain data of tissue strips prepared from biopsies or post-mortem emphysematous and fibrotic lungs. If it is indeed changes in the tissue that are important, then the tissue strips should mimic the results of Chapter 5. However, owing to the patchy nature of these diseases (emphysema in particular) the data may not prove to be conclusive unless a reasonable number of experiments can be performed.

### 9.2.4 Morphometric study of collagen fibre recruitment

The models in Chapter 3 and 4 predicted that collagen fibre straightening occurs in a gradually progressive manner with the applied load. When the tissue is subjected to nonuniform loading such as with uniaxial stretch, this process leads to structural distortions and the development of a heterogeneous distribution of stress. Although the determination of local stresses in tissue is not possible, it is possible to fix and image tissue samples from degassed rat lungs at different levels of uniaxial tension. By selectively staining the collagen fibres, perhaps with Gomori's silver stain or Sirius red, the degree of distortion could be observed. More importantly, the distribution of collagen fibre straightening could be assessed at each level of uniaxial strain. The shape of the collagen fibre distribution could thus be morphologically determined and compared with the model predictions computed from the length tension curves.

### 9.2.5 Assessment of plasticity within the lung tissue

In Chapter 6 it was shown that the Hammerstein model could account for more than 80% of the dissipation that occurred during slow cycling. Since the Hammerstein model is describable using the Volterra series, it may be that the remaining energy dissipation arose from plastic processes which can not be accounted for by the Volterra series. This represented a reduction of earlier estimates of ~30% from parametric modelling approaches which may not have accurately modelled all the viscoelastic behaviour (114). The nonparametric models of Chapter 6 do not have this limitation. It was also shown that increasingly more of the energy dissipation could be accounted for by increasing the lag of the linear block impulse response function of the Hammerstein model. However, further reduction of the lower estimate for plasticity could not be performed since the data length was insufficient to support reliable estimates of the impulse response function for longer lag lengths. In practice, one can measure accurate tissue strip data for very long records. It may thus be possible to improve the estimation of the model. However, in order to conclusively resolve this we would have to be certain that the impulse response estimates at the long lags were attributable to model behaviour.

This is more likely to be the case, since the perturbation from which the model is identified is very dissimilar to the sinusoidal signal which the model is used to predict. However, corroboration of the findings could possibly be achieved from the estimation of sinusoids at different low frequencies. If the results were similar for each of the loops, it would indicate that the model may be predicting the underlying viscoelastic behaviour.

# 10. References


1. Agostoni, E. Mechanics of the pleural space. In: *Handbook of Physiology*, edited by P. T. Macklem and J. Mead. Bethesda, MD: Am. Physiol. Soc. 1986, p. 531-559.

2. Azuma, T. and M. Hasegawa. A rheological approach to the architecture of arterial walls. *Jap. J. Physiol.* 21: 27-47, 1971.

3. Bachofen, H., S. Schurch, M. Urbinelli, and E. R. Weibel. Relations among alveolar surface tension, surface area, volume, and recoil pressure. *J. Appl. Physiol.* 62: 1878-1887, 1987.

4. Bak, P. and K. Chen. Self-organized criticality. *Scientific American* 46-53, 1991.

5. Bak, P., C. Tang, and K. Wiesenfeld. Self-organized criticality: an explanation of 1/f noise. *Phys. Rev. Lett.* 59: 381-384, 1987.

6. Balassy, Z., M. Mishima, and J. H. T. Bates. Changes in regional lung impedance after intravenous histamine bolus in dogs: effects of lung volume. *J. Appl. Physiol.* 78: 875-880, 1995.

7. Barnas, G. M., D. Stamenovic, K. R. Lutchen, and C. F. Mackenzie. Lung and chest wall impedances in the dog: effects of frequency and tidal volume. *J. Appl. Physiol.* 72: 87-93, 1992.

8. Bates, J. H. T., M. Mishima, and Z. Balassy. Measuring the mechanical properties of the lung in vivo with spatial resolution at the acinar level. *Physiological Measurement* 16: 151-159, 1995.

9. Bates, J. H. T., K. A. Brown, and T. Kochi. Respiratory mechanics in the normal dog determined by expiratory flow interruption. *J. Appl. Physiol.* 67: 2276-2285, 1989.

10. Bates, J. H. T., A. M. Lauzon, G. S. Dechman, G. N. Maksym, and T. F. Schuessler. Temporal dynamics of pulmonary response to intravenous histamine in dogs: effects of dose and lung volume. *J. Appl. Physiol.* 76: 616-626, 1994.

11. Bates, J. H. T., M. S. Ludwig, P. D. Sly, K. Brown, J. G. Martin, and J. J. Fredberg. Interrupter resistance elucidated by alveolar pressure measurement in open-chest normal dogs. *J. Appl. Physiol.* 65: 408-414, 1988.

12. Bates, J. H. T., G. N. Maksym, D. Navajas, and B. Suki. Lung tissue rheology and 1/f noise. *Ann. Biomed. Eng.* 22: 674-681, 1994.

13. Baydur, A., W. A. Behrakis, W. A. Zin, M. Jaeger, and J. Milic-Emili. A simple method for assessing the validity of the esophageal balloon technique. *Am. Rev. Respir. Dis.* 126: 788-791, 1982.

14. Brown, R. E., J. P. Butler, R. A. Rogers, and D. E. Leith. Mechanical connections between elastin and collagen. *Connective Tissue Research* 30: 295-308, 1994.

15. Budiansky, B. and E. Kimmel. Elastic moduli of the lungs. *J. Appl. Mech. Trans. ASME* 54: 351-358, 1987.

16. Bull, H. B. Protein structure and elasticity. In: *Tissue Elasticity*, edited by J. W. Remington. Washington: Am. Physiol. Soc. 1957, p. 33-42.

17. Carton, R. W., J. Dainauskas, and J. W. Clark. Elastic properties of single elastic fibers. *J. Appl. Physiol.* 17: 547-551, 1962.

18. Chapra, S. C. and R. P. Canale. *Numerical methods for engineers.* New York: McGraw-Hill, 1988, p. 128

19. Cheng, W., D. S. DeLong, G. N. Franz, E. L. Petsonk, and D. G. Frazer. Contribution of opening and closing of lung units to lung hysteresis. *Respir. Physiol.* 102: 205-215, 1995.

20. Christensen, K., Z. Olami, and P. Bak. Deterministic $1/f$ noise in nonconservative models of self-organized criticality. *Phys. Rev. Lett.* 68: 2417-2420, 1992.

21. Colebatch, H. J., I. A. Greaves, and C. K. Ng. Exponential analysis of elastic recoil and aging in healthy males and females. *J. Appl. Physiol. : Respirat. Environ. Exercise Physiol.* 47: 683-691, 1979.

22. Colebatch, H. J., C. K. Ng, and N. Nikov. Use of an exponential function for elastic recoil. *J. Appl. Physiol. : Respirat. Environ. Exercise Physiol.* 46: 387-393, 1979.

23. Daroczy, B. and Z. Hantos. An improved forced oscillatory estimation of respiratory impedance. *International Journal of Bio-Medical Computing* 13: 221-235, 1982.

24. Davey, B. L. and J. H. T. Bates. Regional lung impedance from forced oscillations through alveolar capsules. *Respir. Physiol.* 91: 165-182, 1993.

25. Debes, J. C. and Y. C. Fung. Effect of temperature on the biaxial mechanics of excised lung parenchyma of the dog. *J. Appl. Physiol.* 73: 1171-1180, 1992.

26. Dechman, G. S., D. A. Chartrand, P. P. Ruiz-Neto, and J. H. T. Bates. The effect of changing end-expiratory pressure on respiratory system mechanics in open- and closed-chest anesthetized, paralyzed patients. *Anesthesia & Analgesia* 81: 279-286, 1995.

27. Decraemer, W. F., M. A. Maes, and V. J. Vanhuyse. An elastic stress-strain relation for soft biological tissues based on a structural model. *J. Biomech.* 13: 463-468, 1980.

28. Denny, E. and R. C. Schroter. The mechanical behaviour of a mammalian lung alveolar duct model. *J. Biomech. Eng.* 117: 254-261, 1995.

29. Dolhnikoff, M., M. Dallaire, and M. S. Ludwig. Lung tissue distortion in response to methacholine in rats: effect of lung volume. *J. Appl. Physiol.* 79: 533-538, 1995.

30. Dubois, A. B., A. W. Brody, D. H. Lewis, and B. F. Burgess. Oscillation mechanics of lungs and chest in man. *J. Appl. Physiol.* 8: 587-594, 1956.

31. Eyles, J. G. and R. L. Pimmel. Estimating respiratory mechanical parameters in parallel compartment models. *IEEE Trans. Biomed. Eng.* 28: 313-317, 1981.

32. Findley, W. N., J. S. Lai, and K. Onaran. *Creep and relaxation of nonlinear viscoelastic materials*. New York: Dover, 1976, p. 367

33. Fine, R., B. McCullough, J. F. Collins, and W. G. Johanson,Jr. Lung elasticity in regional and diffuse pulmonary fibrosis. *J. Appl. Physiol. : Respirat. Environ. Exercise Physiol.* 47: 138-144, 1979.

34. Frankus, A. and G. C. Lee. A theory for distortion studies of lung parenchyma based on alveolar membrane properties. *J. Biomech.* 7: 101-107, 1974.

35. Fredberg, J. J., D. Bunk, E. Ingenito, and S. A. Shore. Tissue resistance and the contractile state of lung parenchyma. *J. Appl. Physiol.* 74: 1387-1397, 1993.

36. Fredberg, J. J., D. H. Keefe, G. M. Glass, R. G. Castile, and I. D. Frantz, 3rd. Alveolar pressure nonhomogeneity during small-amplitude high-frequency oscillation. *J. Appl. Physiol. : Respirat. Environ. Exercise Physiol.* 57: 788-800, 1984.

37. Fredberg, J. J. and D. Stamenovic. On the imperfect elasticity of lung tissue. *J. Appl. Physiol.* 67: 2408-2419, 1989.

38. Fukaya, H., C. J. Martin, A. C. Young, and S. Katsura. Mechanial properties of alveolar walls. *J. Appl. Physiol.* 25: 689-695, 1968.

39. Fung, Y. C. A theory of elasticity of the lung. *J. Appl. Mech. Trans. ASME* 41: 8-14, 1974.

40. Fung, Y. C. *Biomechanics, mechanical properties of living tissues.* New York: Springer-Verlag, 1981, p. 336

41. Fung, Y. C. Microrheology and constitutive equation of soft tissue [published erratum appears in Biorheology 1989;26(2):281]. *Biorheology* 25: 261-270, 1988.

42. Fung, Y. C. Connecting incremental shear modulus and Poisson's ratio of lung tissue with morphology and rheology of microstructure. *Biorheology* 26: 279-289, 1989.

43. Fung, Y. C., P. Tong, and P. Patitucci. Stress and strain in the lung. *J. Eng. Mech. Div. ASCE* 104: 201-223, 1978.

44. Gibson, G. J. and N. B. Pride. Lung distensibility. The static pressure-volume curve of the lungs and its use in clinical assessment. [Review]. *British Journal of Diseases of the Chest* 70: 143-184, 1976.

45. Gibson, G. J., N. B. Pride, J. Davis, and R. C. Schroter. Exponential description of the static pressure-volume curve of normal and diseased lungs. *Am. Rev. Respir. Dis.* 120: 799-811, 1979.

46. Gil, J., H. Bachofen, P. Gehr, and E. R. Weibel. Alveolar volume-surface area relation in air- and saline-filled lungs fixed by vascular perfusion. *J. Appl. Physiol. : Respirat. Environ. Exercise Physiol.* 47: 990-1001, 1979.

47. Gilroy, R. J., R. Peslin, C. Duvivier, F. Blum, and J. P. Butler. Relation of mouth flow to body surface flow during forced oscillation at the chest. *J. Appl. Physiol.* 63: 121-129, 1987.

48. Greaves, I. A. and H. J. Colebatch. Elastic behavior and structure of normal and emphysematous lungs post mortem. *Am. Rev. Respir. Dis.* 121: 127-136, 1980.

49. Haber, P. S., H. J. Colebatch, C. K. Ng, and I. A. Greaves. Alveolar size as a determinant of pulmonary distensibility in mammalian lungs. *J. Appl. Physiol. : Respirat. Environ. Exercise Physiol.* 54: 837-845, 1983.

50. Hance, A. J. and R. G. Crystal. The connective tissue of lung. [Review]. *Am. Rev. Respir. Dis.* 112: 657-711, 1975.

51. Hantos, Z., A. Adamicza, E. Govaerts, and B. Daroczy. Mechanical impedances of lungs and chest wall in the cat. *J. Appl. Physiol.* 73: 427-433, 1992.

52. Hantos, Z., B. Daroczy, T. Csendes, B. Suki, and S. Nagy. Modeling of low-frequency pulmonary impedance in dogs. *J. Appl. Physiol.* 68: 849-860, 1990.

53. Hantos, Z., B. Daroczy, B. Suki, and S. Nagy. Low-frequency respiratory mechanical impedance in the rat. *J. Appl. Physiol.* 63: 36-43, 1987.

54. Hantos, Z., B. Daroczy, B. Suki, S. Nagy, and J. J. Fredberg. Input impedance and peripheral inhomogeneity of dog lungs. *J. Appl. Physiol.* 72: 168-178, 1992.

55. Hantos, Z., B. Suki, T. Csendes, and B. Daroczy. Constant-phase modelling of pulmonary tissue impedance. *Bull. Eur. Physiopathol. Respir.* 23, Suppl. 326s1987.(Abstract)

56. Haut, R. C. and R. W. Little. A constitutive equation for collagen fibers. *J. Biomech.* 5: 423-430, 1972.

57. Hildebrandt, J. Comparison of mathematical models for cat lung and viscoelastic balloon derived by Laplace transform methods from pressure-volume data. *Bulletin of Mathematical Biophysics* 31: 651-667, 1969.

58. Hildebrandt, J. Pressure-volume data of cat lung interpreted by a plastoelastic, linear viscoelastic model. *J. Appl. Physiol.* 28: 365-372, 1970.

59. Hoppin, F. G., Jr., G. C. Lee, and S. V. Dawson. Properties of lung parenchyma in distortion. *J. Appl. Physiol.* 39: 742-751, 1975.

60. Hoppin, F. G. J. and J. Hildebrandt. Mechanical properties of the lung. In: *Bioengineering aspects of the lung*, edited by J. B. West. New York: Marcel Dekker, Inc. 1977, p. 83-162.

61. Hunter, I. W. and R. E. Kearney. Two-sided linear filter identification. *Med. Biol. Eng. Comput.* 21: 203-209, 1983.

62. Hunter, I. W. and R. E. Kearney. Generation of random sequences with jointly specified probability density and autocorrelation functions. *Biol. Cybern.* 47: 141-146, 1983.

63. Hunter, I. W. and M. J. Korenberg. The identification of nonlinear biological systems: Wiener and Hammerstein cascade models. *Biol. Cybern.* 55: 135-144, 1986.

64. Ingenito, E. P., L. Mark, and B. Davison. Effects of acute lung injury on dynamic tissue properties. *J. Appl. Physiol.* 77: 2689-2697, 1994.

65. Jackson, A. C. and K. R. Lutchen. Modeling of respiratory system impedances in dogs. *J. Appl. Physiol.* 62: 414-420, 1987.

66. Jackson, A. C., K. R. Lutchen, and H. L. Dorkin. Inverse modeling of dog airway and respiratory system impedances. *J. Appl. Physiol.* 62: 2273-2282, 1987.

67. Karakaplan, A. D., M. P. Bieniek, and R. Skalak. A mathematical model of lung parenchyma. *J. Biomech. Eng.* 102: 124-136, 1980.

68. Karlinsky, J., J. Fredette, G. Davidovits, A. Catanese, R. Snider, B. Faris, G. L. Snider, and C. Franzblau. The balance of lung connective tissue elements in elastase-induced emphysema. *Journal of Laboratory & Clinical Medicine* 102: 151-162, 1983.

69. Karlinsky, J. B., J. T. Bowers, 3rd, J. V. Fredette, and J. Evans. Thermoelastic properties of uniaxially deformed lung strips. *J. Appl. Physiol.* 58: 459-467, 1985.

70. Karlinsky, J. B., G. L. Snider, C. Franzblau, P. J. Stone, and F. G. J. Hoppin. In vitro effects of elastase and collagenase on mechanical properties of hamster lungs. *Am. Rev. Respir. Dis.* 113: 769-777, 1976.

71. Keshner, M. S. $1/f$ noise. *Proc. IEEE* 70: 212-218, 1982.

72. Kimmel, E., R. D. Kamm, and A. H. Shapiro. A cellular model of lung elasticity. *J. Biomech. Eng.* 109: 126-131, 1987.

73. Kochi, T., J. H. T. Bates, S. Okubo, E. S. Petersen, and J. Milic-Emili. Respiratory mechanics determined by flow interruption during passive expiration in cats. *Respir. Physiol.* 78: 243-252, 1989.

74. Koeller. Applications of fractional calculus to the theory of viscoelasticity. *J. Appl. Mech.* 51: 299-307. 1984.

75. Koo, K. W., J. A. Hayes, H. M. Kagan, D. E. Lieth, C. Franzblau, and G. L. Snider. Lung volumes and mechanics following elastase and collagenase in hamsters. *Clin. Res.* 22: 508-514A1974.

76. Korenberg, M. , J. and I. Hunter,W. Identification of nonlinear biological systems: Volterra kernel approaches. *Ann. Biomed. Eng.* 24: 250-268, 1996.

77. Kowe, R., R. C. Schroter, F. L. Matthews, and D. Hitchings. Analysis of elastic and surface tension effects in the lung alveolus using finite element methods. *J. Biomech.* 19: 541-549, 1986.

78. Lai-Fook, S. J., T. A. Wilson, R. E. Hyatt, and J. R. Rodarte. Elastic constants of inflated lobes of dog lungs. *J. Appl. Physiol.* 40: 508-513, 1976.

79. Lambert, R. K. and T. A. Wilson. A model for the elastic properties of the lung and their effect of expiratory flow. *J. Appl. Physiol.* 34: 34-48, 1973.

80. Lanir, Y. Constitutive equations for the lung tissue. *J. Biomech. Eng.* 105: 374-380, 1983.

81. Lanir, Y. On the structural origin of the quasilinear viscoelastic behavior of tissues. In: *Frontiers in biomechanics*, edited by G. W. Schmid-Schönbein, S. L.-Y. Woo, and B. W. Zweifach. New York: Springer-Verlag, 1986, p. 130-136.

82. Lauzon, A. M., G. S. Dechman, J. G. Martin, and J. H. T. Bates. Time course of histamine-induced bronchoconstriction and its adrenergic and H2 modulation. *Respir. Physiol.* 99: 127-138, 1995.

83. Lee, G. C. and A. Frankus. Elasticity properties of lung parenchyma derived from experimental distortion data. *Biophys. J.* 15: 481-493, 1975.

84. Ligas, J. R., F. P. Primiano,Jr., and G. M. Saidel. Static mechanics of excised whole lung: pleural mechanics. *Ann. Biomed. Eng.* 12: 437-448, 1984.

85. Liu, J.-T. and G. C. Lee. Static finite deformation analysis of the lung. *J. Eng. Mech. Div. ASCE* 104: 225-238, 1978.

86. Ludwig, M. S., S. Bellofiore, S. A. Shore, J. M. Drazen, and J. J. Fredberg. Dynamics of the collateral pathways of canine lungs after flow interruption. *J. Appl. Physiol.* 67: 1213-1219, 1989.

87. Lutchen, K. R., Z. Hantos, F. Petak, A. Adamicza, and B. Suki. Airway inhomogeneities contribute to apparent lung tissue mechanics during constriction. *J. Appl. Physiol.* 80: 1841-1849, 1996.

88. Lutchen, K. R. and A. C. Jackson. Reliability of parameter estimates from models applied to respiratory impedance data. *J. Appl. Physiol.* 62: 403-413, 1987.

89. Lutchen, K. R. and A. C. Jackson. Effects of tidal volume and methacholine on low-frequency total respiratory impedance in dogs. *J. Appl. Physiol.* 68: 2128-2138, 1990.

90. Lutchen, K. R., B. Suki, Q. Zhang, F. Petak, B. Daroczy, and Z. Hantos. Airway and tissue mechanics during physiological breathing and bronchoconstriction in dogs. *J. Appl. Physiol.* 77: 373-385, 1994.

91. Macklem, P. T. and D. Eidelman. Reexamination of the elastic properties of emphysematous lungs. *Respiration* 57: 187-192, 1990.

92. Maksym, G. N. and D. Chapman. Sonobuoy suspension design study: elastic elements. Defense Research Establishment Atlantic tehcnical note UA/90/4: 1990.

93. Maksym, G. N., D. Navajas, and J. H. T. Bates. A tissue strip oscillator and preconditioning protocol. *Proc. 19th Conf. Canadian Med. Biol. Eng. Soc. Ottawa.* 100-101, 1993.

94. Maksym, G. N., D. Navajas, and J. H. T. Bates. Lung parenchyma stress response to step strains. *Proc. 15th Ann. Int. Conf. IEEE Eng. Med. Biol. Soc. San Diego.* 1116-1117, 1993.

95. Maksym, G. N., T. F. Schuessler, and J. H. T. Bates. Nonlinear pulmonary rat mechanics identification. *Amer. J. Resp. Crit. Care Med.* 151:A116, 1995. (Abstract)

96. Mandelbrot, B. B. and J. W. Van Ness. Fractional brownian motions, fractional noises, and applications. *SIAM Rev.* 10: 422-437, 1968.

97. Matsuda, M., Y. C. Fung, and S. S. Sobin. Collagen and elastin fibers in human pulmonary alveolar mouths and ducts. *J. Appl. Physiol.* 63: 1185-1194, 1987.

98. Mead, J. Mechanical Properties of Lungs. *Physiol. Rev.* 41: 281-328, 1961.

99. Mead, J. Contribution of compliance of airways to frequency-dependent behavior of lungs. *J. Appl. Physiol.* 26: 670-673, 1969.

100. Mead, J. and C. Collier. Relation of volume history of lungs to respiratory mechanics in anaesthetized dogs. *J. Appl. Physiol.* 14: 669-678, 1959.

101. Mead, J., T. Takishima, and D. Leith. Stress distribution in lungs: a model of pulmonary elasticity. *J. Appl. Physiol.* 28: 596-608, 1970.

102. Mercer, R. R. and J. D. Crapo. Three-dimensional reconstruction of the rat acinus. *J. Appl. Physiol.* 63: 785-794, 1987.

103. Mercer, R. R. and J. D. Crapo. Spatial distribution of collagen and elastin fibers in the lungs. *J. Appl. Physiol.* 69: 756-765, 1990.

104. Mercer, R. R. and J. D. Crapo. Structural changes in elastic fibers after pancreatic elastase administration in hamsters. *J. Appl. Physiol.* 72: 1473-1479, 1992.

105. Michaelson, E. D., E. D. Grassman, and W. R. Peters. Pulmonary mechanics by spectral analysis of forced random noise. *J. Clin. Invest.* 56: 1210-1230, 1975.

106. Mijailovich, S. M., D. Stamenovic, R. Brown, D. E. Leith, and J. J. Fredberg. Dynamic moduli of rabbit lung tissue and pigeon ligamentum propatagiale undergoing uniaxial cyclic loading. *J. Appl. Physiol.* 76: 773-782, 1994.

107. Mijailovich, S. M., D. Stamenovic, and J. J. Fredberg. Toward a kinetic theory of connective tissue micromechanics. *J. Appl. Physiol.* 74: 665-681, 1993.

108. Milic-Emili, J., J. Mead, and J. M. Turner. Topography of esophageal pressure as a function of posture in man. *J. Appl. Physiol.* 19: 212-216, 1964.

109. Mishima, M., Z. Balassy, and J. H. T. Bates. Acute pulmonary response to intravenous histamine using forced oscillations through alveolar capsules in dogs. *J. Appl. Physiol.* 77: 2140-2148, 1994.

110. Moretto, A., M. Dallaire, P. Romero, and M. Ludwig. Effect of elastase on oscillation mechanics of lung parenchymal strips. *J. Appl. Physiol.* 77: 1623-1629, 1994.

111. Mount, L. E. The ventilation flow-resistance and compliance of rat lungs. *J. Physiol. Lond.* 127: 157-167, 1955.

112. Nagase, T., Y. Fukuchi, S. Teramoto, T. Matsuse, and H. Orimo. Mechanical interdependence in relation to age: effects of lung volume on airway resistance in rats. *J. Appl. Physiol.* 77: 1172-1177, 1994.

113. Nakamura, M., H. Sasaki, and T. Takishima. Effect of lung surface tension on bronchial collapsibility in excised dog lungs. *J. Appl. Physiol. : Respirat. Environ. Exercise Physiol.* 47: 692-700, 1979.

114. Navajas, D., G. N. Maksym, and J. H. T. Bates. Dynamic viscoelastic nonlinearity of lung parenchymal tissue. *J. Appl. Physiol.* 79: 348-356, 1995.

115. Navajas, D., S. Mijailovich, G. M. Glass, D. Stamenovic, and J. J. Fredberg. Dynamic response of the isolated passive rat diaphragm strip. *J. Appl. Physiol.* 73: 2681-2692, 1992.

116. Oldmixon, E. H., J. P. Butler, and F. G. Hoppin,Jr. Lengths and topology of alveolar septal borders. *J. Appl. Physiol.* 67: 1930-1940, 1989.

117. Oldmixon, E. H. and F. G. Hoppin,Jr. Distribution of elastin and collagen in canine lung alveolar parenchyma. *J. Appl. Physiol.* 67: 1941-1949, 1989.

118. Otis, A. B. History of respiratory mechanics. In: *Handbook of physiology*, edited by P. T. Macklem and J. Mead. Bethesda, MD: Am. Physiol. Soc. 1986, p. 1-12.

119. Otis, A. B., C. B. McKerrow, R. A. Bartlett, J. Mead, M. B. McIlroy, J. Selverstone, and E. P. Radford. Mechanical factors in distribution of pulmonary ventilation. *J. Appl. Physiol.* 8: 427-443, 1956.

120. Pare, P. D., L. A. Brooks, J. Bates, L. M. Lawson, J. M. Nelems, J. L. Wright, and J. C. Hogg. Exponential analysis of the lung pressure-volume curve as a predictor of pulmonary emphysema. *Am. Rev. Respir. Dis.* 126: 54-61, 1982.

121. Peslin, R., C. Duvivier, and C. Gallina. Total respiratory input and transfer impedances in humans. *J. Appl. Physiol.* 59: 492-501, 1985.

122. Peslin, R. and J. J. Fredberg. Oscillation mechanics of the respiratory system. In: *Handbook of physiology*, edited by P. T. Macklem and J. Mead. Bethesda, MD: Am. Physiol. Soc. 1986, p. 145-177.

123. Peslin, R., C. Gallina, and C. Duvivier. Respiratory transfer impedances with pressure input at the mouth and chest. *J. Appl. Physiol.* 61: 81-86, 1986.

124. Peslin, R., M. Rotger, N. Delaigue, and C. Duvivier. Compared responses of rat lungs to step volume changes and to sinusoidal forcing. *Biorheology* 28: 527-535, 1991.

125. Petak, F., Z. Hantos, A. Adamicza, and B. Daroczy. Partitioning of pulmonary impedance: modeling vs. alveolar capsule approach. *J. Appl. Physiol.* 75: 513-521, 1993.

126. Press, W. H., B. P. Flannery, S. A. Teukolsky, and W. T. Vertterling. *Numerical recipes, the art of scientific computing.* Cambridge NY: Cambridge University Press, 1986, p. 200-209.

127. Pride, N. B. and P. T. Macklem. Lung mechanics in disease. In: *Handbook of Physiology*, edited by P. T. Macklem and J. Mead. Bethesda, MD: Am. Physiol. Soc. 1986, p. 659-691.

128. Qian, S. Y. and W. Mitzner. In vivo and in vitro lung reactivity in elastase-induced emphysema in hamsters. *Am. Rev. Respir. Dis.* 140: 1549-1555, 1989.

129. Radford, E. P. Recent studies of the mechanical properties of mammalian lungs. In: *Tissue elasticity*, edited by J. W. Remington. Washington, DC: Am. Physiol. Soc. 1957, p. 177-190.

130. Reiser, M. and N. Wirth. *Programming in oberon, steps beyond pascal and modula.* New York: Addison-Wesley, 1992.

131. Rouse, P. E. A theory of the linear viscoelastic properties of dilute solutions of coiled polymers. *J. Chem. Phys.* 21: 1272-1280, 1953.

132. Salazar, E. and J. H. Knowles. An analysis of pressure-volume characteristics of the lungs. *J. Appl. Physiol.* 19: 97-104, 1964.

133. Sasaki, H., T. Takishima, and T. Sasaki. Influence of lung parenchyma on dynamic bronchial collapsibility of excised dog lungs. *J. Appl. Physiol. : Respirat. Environ. Exercise Physiol.* 42: 699-705, 1977.

134. Sata, M., K. Takahashi, S. Sato, and H. Tomoike. Structural and functional characteristics of peripheral pulmonary parenchyma in golden hamsters. *J. Appl. Physiol.* 78: 239-246, 1995.

135. Schellenberg, J. C. and G. C. Liggins. Elastin and collagen in the fetal sheep lung. I. Ontogenesis. *Pediatric Research* 22: 335-338, 1987.

136. Schuessler, T. F. and J. H. T. Bates. A computer-controlled research ventilator for small animals: design and evaluation. *IEEE Trans. Biomed. End.* 42: 860-866, 1995.

137. Setnikar, I. Origine e significato della proprieta meccaniche del pulmone. *Arch. Fisiol.* 55: 349-374, 1955.

138. Similowski, T. and J. H. T. Bates. Two-compartment modelling of respiratory system mechanics at low frequencies: gas redistribution or tissue rheology?. [Review]. *European Respiratory Journal* 4: 353-358, 1991.

139. Similowski, T., P. Levy, C. Corbeil, M. Albala, R. Pariente, J. P. Derenne, J. H. T. Bates, B. Jonson, and J. Milic-Emili. Viscoelastic behavior of lung and chest wall in dogs determined by flow interruption. *J. Appl. Physiol.* 67: 2219-2229, 1989.

140. Smith, J. C. and D. Stamenovic. Surface forces in lungs. I. Alveolar surface tension-lung volume relationships. *J. Appl. Physiol.* 60: 1341-1350, 1986.

141. Snider, G. L. Pathogenesis of emphysema and chronic bronchitis. [Review]. *Medical Clinics of North America* 65: 647-665, 1981.

142. Sobin, S. S., Y. C. Fung, and H. M. Tremer. Collagen and elastin fibers in human pulmonary alveolar walls. *J. Appl. Physiol.* 64: 1659-1675, 1988.

143. Soong, T. T. and W. N. Huang. A stochastic model for biological tissue elasticity in simple elongation. *J. Biomech.* 6: 451-458, 1973.

144. Stamenovic, D., G. M. Glass, G. M. Barnas, and J. J. Fredberg. Viscoplasticity of respiratory tissues. *J. Appl. Physiol.* 69: 973-988, 1990.

145. Stamenovic, D., K. R. Lutchen, and G. M. Barnas. Alternative model of respiratory tissue viscoplasticity. *J. Appl. Physiol.* 75: 1062-1069, 1993.

146. Stamenovic, D. and J. C. Smith. Surface forces in lungs. III. Alveolar surface tension and elastic properties of lung parenchyma. *J. Appl. Physiol.* 60: 1358-1362, 1986.

147. Stamenovic, D. and T. A. Wilson. A strain energy function for lung parenchyma. *J. Biomech. Eng.* 107: 81-86, 1985.

148. Stamenovic, D. and D. Yager. Elastic properties of air- and liquid-filled lung parenchyma. *J. Appl. Physiol.* 65: 2565-2570, 1988.

149. Sugihara, T., J. Hildebrandt, and C. J. Martin. Viscoelastic properties of alveolar wall. *J. Appl. Physiol.* 33: 93-98, 1972.

150. Sugihara, T., C. J. Martin, and J. Hildebrandt. Length-tension properties of alveolar wall in man. *J. Appl. Physiol.* 30: 874-878, 1971.

151. Suki, B., R. Peslin, C. Duvivier, and R. Farré. Lung impedance in healthy humans measured by forced oscillations from 0.01 to 0.1 Hz. *J. Appl. Physiol.* 67: 1623-1629, 1989.

152. Suki, B. Nonlinear phenomena in respiratory mechanical measurements. *J. Appl. Physiol.* 74: 2574-2584, 1993.

153. Suki, B., A. L. Barabasi, Z. Hantos, F. Petak, and H. E. Stanley. Avalanches and power law behaviour in lung inflation. *Nature* 368: 615-618, 1994.

154. Suki, B., A. L. Barabasi, and K. R. Lutchen. Lung tissue viscoelasticity: a mathematical framework and its molecular basis. *J. Appl. Physiol.* 76: 2749-2759, 1994.

155. Suki, B. and J. H. T. Bates. A nonlinear viscoelastic model of lung tissue mechanics. *J. Appl. Physiol.* 71: 826-833, 1991.

156. Suki, B., Z. Hantos, B. Daroczy, G. Alkaysi, and S. Nagy. Nonlinearity and harmonic distortion of dog lungs measured by low-frequency forced oscillations. *J. Appl. Physiol.* 71: 69-75, 1991.

157. Suki, B. and K. R. Lutchen. Pseudorandom signals to estimate apparent transfer and coherence functions of nonlinear systems: applications to respiratory mechanics. *IEEE Trans. Biomed. End.* 39: 1142-1151, 1992.

158. Suki, B., A.-L.Barabasi, Z. Hantos. F. Petak, and H. Eugene Stanley. Avalanches and power-law behaviour in lung inflation. *Nature* 368: 615-618, 1994.

159. Suki, B., R. Peslin, C. Duvivier, and R. Farre. Lung impedance in healthy humans measured by forced oscillations from 0.01 to 0.1 Hz. *J. Appl. Physiol.* 67: 1623-1629, 1989.

160. Suki, B., Q. Zhang, and K. R. Lutchen. Relationship between frequency and amplitude dependence in the lung: a nonlinear block-structured modeling approach. *J. Appl. Physiol.* 79: 660-671, 1995.

161. Suwa, N., H. Fukasawa, R. Fujimoto, and M. Kawakami. Strain and stress of pulmonary tissues. *Tohoku J. Exper. Med.* 90: 61-75, 1966.

162. Tai, R. C. and G. C. Lee. Isotropy and homogeneity of lung tissue deformation. *J. Biomech.* 14: 243-252, 1981.

163. Thompson, M. J. and H. J. Colebatch. Decreased pulmonary distensibility in fibrosing alveolitis and its relation to decreased lung volume. *Thorax* 44: 725-731, 1989.

164. Vawter, D. L. A finite element model for macroscopic deformation of the lung. *J. Biomech. Eng.* 102: 1-7, 1980.

165. Vawter, D. L., Y. C. Fung, and J. B. West. Elasticity of excised dog lung parenchyma. *J. Appl. Physiol. : Respirat. Environ. Exercise Physiol.* 45: 261-269, 1978.

166. Vawter, D. L., Y. C. Fung, and J. B. West. Constitutive equation of lung tissue elasticity. *J. Biomech. Eng.* 105: 38-45, 1979.

167. Verbeken, E. K., M. Cauberghs, J. M. Lauweryns, and K. P. Van de Woestijne. Structure and function in fibrosing alveolitis. *J. Appl. Physiol.* 76: 731-742, 1994.

168. Voss, R. F. and J. Clarke. 1/*f* noise in music: Music from 1/*f* noise. *J. Acoust. Soc.* 63: 258-263, 1978.

169. Weibel, E. R. Functional morphology of lung parenchyma. In: *Handbook of Physiology*, edited by P. T. Macklem and J. Mead. Bethesda: Am. Physiol. Soc. 1986, p. 89-110.

170. Weibel, E. R. and J. Gil. Structure-function relationships at the alveolar level. In: *Bioengineering aspects of the lung*, edited by J. B. West. New York: Marcel-Dekker, Inc. 1977, p. 1-81.

171. West, B. J. and M. F. Schlesinger. On the ubiquity of 1/f noise. *Int. J. Mod. Phys.* 3: 795-819, 1989.

172. West, J. B. and F. L. Matthews. Stresses, strains, and surface pressures in the lung caused by its weight. *J. Appl. Physiol.* 32: 332-345, 1972.

173. Westwick, D. T. Methods for the identification of multiple-input nonlinear systems. Ph.D Thesis, McGill University pp. 157-159, 1995.

174. Wilson, T. A. A continuum analysis of a two-dimensional mechanical model of the lung parenchyma. *J. Appl. Physiol.* 33: 472-478, 1972.

175. Wilson, T. A., J. J. Fredberg, J. R. Rodarte, and R. E. Hyatt. Interdependence of regional expiratory flow. *J. Appl. Physiol.* 59: 1924-1928, 1985.

176. Wilson, T. A., M. J. Hill, and R. D. Hubmayr. Regional lung volume trajectories during expiratory flow in dogs. *J. Appl. Physiol.* 80: 1144-1148, 1996.

177. Wong, D. F., H. W. Leong, and C. L. Liu. *Simulated annealing for VLSI design.* Norwell, MA: Kluwer Academic, 1988, p. 1-7.

178. Wright, J. L. and A. Churg. Smoke-induced emphysema in guinea pigs is associated with morphometric evidence of collagen breakdown and repair. *Am. J. Physiol. (Lung Cell. Mol. Physiol. 12)* 268: L17-L20, 1995.

179. Yokoyama, E., Z. Nambu, I. Uchiyama, and H. Kyono. An emphysema model in rats treated intratracheally with elastase. *Environmental Research* 42: 340-352, 1987.

180. Zeng, Y. J., D. Yager, and Y. C. Fung. Measurement of the mechanical properties of the human lung tissue. *J. Biomech. Eng.* 109: 169-174, 1987.

# IMAGE EVALUATION TEST TARGET (QA-3)

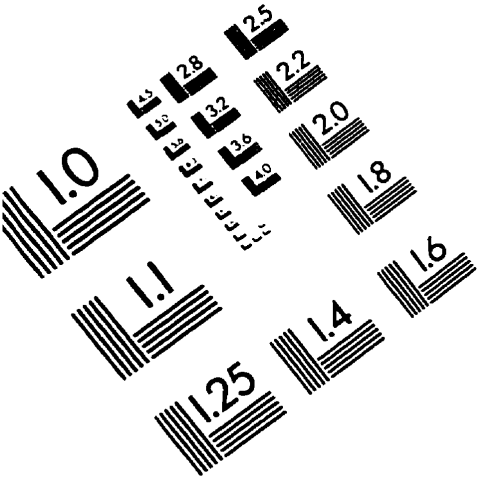


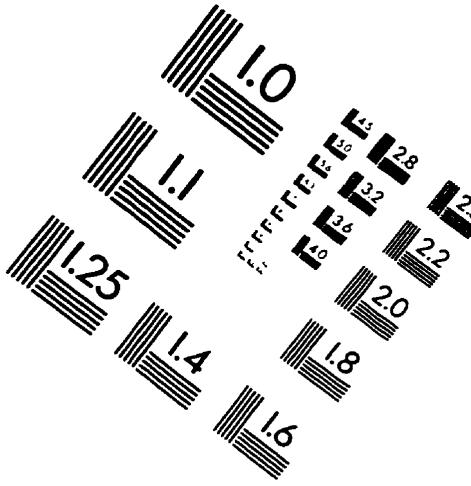


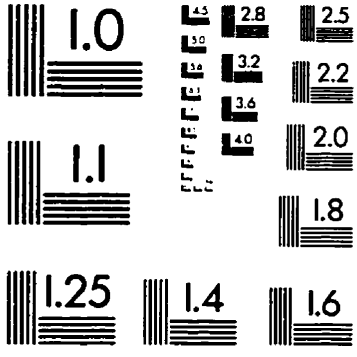


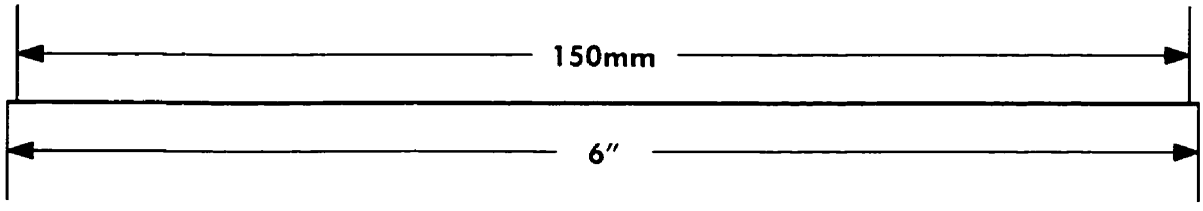


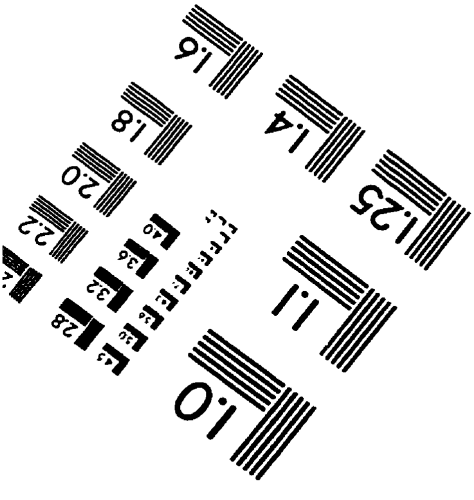


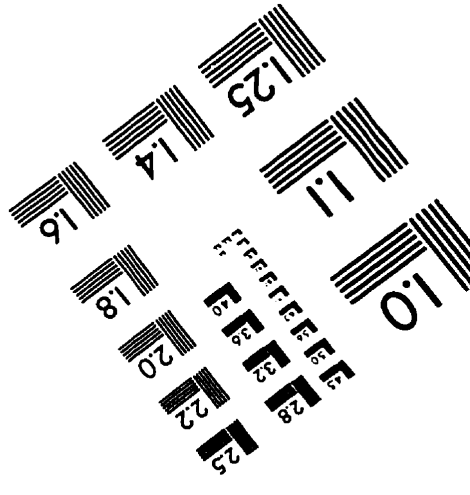


APPLIED IMAGE, Inc
1653 East Main Street
Rochester, NY 14609 USA
Phone: 716/482-0300
Fax: 716/288-5989